universität wien

DISSERTATION / DOCTORAL THESIS

Titel der Disseratation / Title of the Doctoral Thesis

„Time domain interference with complex systems“

verfasst von / submitted by

Philipp Rieser, BSc MSc

angestrebter akademischer Grad / in partial fulfilment of the requirements for the degree of

Doktor der Naturwissenschaften (Dr.rer.nat.)

Wien, 2023 / Vienna, 2023

Studienkennzahl lt. Studienblatt / degree programme code as it appears on the student record sheet:	UA 796 605 411
Studienrichtung lt. Studienblatt / degree programme as it appears on the student record sheet:	Physik
Betreut von / Supervisor:	Univ. Prof. Dr. Markus Arndt

Abstract

Quantum physics has, since its inception in the early 20th century, enriched the world with numerous discoveries and experiments, probing the world on a miniature scale. Interference of massive systems is a phenomenon that lies at the heart of quantum physics. Here, the particles become delocalized and propagate through space as a wave, instead of classical trajectories. This phenomenon has been studied for complex systems [1, 2], and has been shown to hold for the mass range accessible in experiments thus far. Pushing the mass limit further and observing interference of more complex and massive systems is an important avenue of research. In this thesis, I present pulsed near-field interference with the optical time-domain matter-wave (OTIMA) interferometer. It is an example of a pulsed Talbot Lau interferometer operating in the near-field regime. The three-grating setup is realized using standing wave laser gratings to spatially modulate the molecular beam by depletion in the antinodes. The OTIMA setup highlights the requirements and peculiarities of a pulsed interferometer and the importance of strong particle-grating interactions to realize interference measurements. With the goal of interference experiments with proteins, it is important to observe and improve these interactions for large complex systems that are inert to vacuum ultraviolet photons. I present an interference experiment with gramicidin, a large polypeptide that shows the progress and required steps toward protein interference.

Additionally, I show the progress in the optical control of molecules using photolabile tags, as well as work on a pulsed source technique for nanoparticles, suitable for optomechanics experiments in high vacuum. Adaptations of this technique for different materials could become a precise mass-controlled source of metal clusters for pulsed interferometer experiments. I discuss the physical and technical limits to consider for interference experiments with high masses, which inform the interferometer design for the next pulsed interferometer, BIOTIMA, and interference with chemically tagged insulin. The proposed interferometer informs the outlook on interference-assisted measurements of molecular properties. I will further use the limits for large interference experiments with the goal of pulsed interference past 1 MDa, where I motivate gold clusters as a candidate system.

Kurzfassung

Die Quantenphysik hat, seit ihrer Geburt im frühen 20en Jahrhundert, die wissenschaftliche Welt mit neuartigen Werkzeugen und Experimenten bereichert, welche der Welt auf Miniaturebene auf den Zahn fühlen. In der Quantenmechanik ist die Interferenz von massiven Teilchen ein Exemplar des einzigartigen Verhaltens von Quantensystemen. Solch ein Interferenzphänomen erscheint, wenn die Teilchen delokalisiert sind und sich wie Wellen verhalten, anstatt klassischen Trajektorien zu folgen. Solche Materiewelleneigenschaften wurden bereits für komplexe Systeme nachgewiesen [1, 2] und zeigt keinen Anschein, fundamental unmöglich zu werden. Daher ist es wichtig, weitere Regime in Komplexität und Größe für Interferenzexperimente erreichbar zu machen, da damit ein direkter Einblick in das quantenmechanische Verhalten von makroskopischen Systemen möglich wird. In dieser Arbeit präsentiere ich das Zeitdomänen Materiewelleninterferometer OTIMA. Es ist ein Beispiel für ein gepulstes Interferometer vom Talbot Lau Typ und operiert im Nahfeld Beugungsregime. Das drei-Gitter Setup wird durch gepulste Stehwellen verwirklicht, die den Molekularstrahl örtlich modulieren, indem sie in den Stehwellenbäuchen den Strahl entleeren. Das OTIMA Experiment veranschaulicht viel der notwendigen Eigenschaften und Besonderheiten eines gepulsten Interferometers im Nahfeld, wie die Notwendigkeit von starken Teilchen-Licht-Wechselwirkungen, um effiziente Gitter zu gewährleisten. Mit Protein-Interferenzexperimenten als Ziel ist es wichtig, diese Interaktionen für Systeme zu studieren und verbessern, die gegenüber Vakuum-ultravioletten Photonen inert sind. Hier präsentiere ich erfolgreiche Interferenz des Polypeptids Gramizidin, womit der Fortschritt und die notwendigen Änderungen in der Herangehensweise für Proteininterferenz hervorgehoben werden.

Zusätzlich beschreibe ich Ansätze für die bessere optische Kontrolle von Molekülen durch die Verwendung von photolabilen Markern, die es ermöglichen werden, den Ladungszustand von Molekülen in der Gasphase zu ändern. Eine weitere Anstrengung besteht in einer gepulsten Quelltechnik für große Nanopartikel, welche für das Laden von optomechanischen Experimenten im Hochvakuum geeignet sein könnte. Um das Proteininterferometer einzuläuten, befasse ich mich mit den physikalischen und technischen Limits, welche auf Interferenzexperimente mit hohen Massen Einfluss nehmen. Diese Limits informieren das Design der nächsten Version des OTIMA Experiments, wo ich auf die Ansprüche für Interferenz mit chemisch markierten Insulin eingehe. Das vorgeschlagene Interferometer dient als Ansporn für Interferenzassistierte Messungen von Moleküleigenschaften. Zuletzt verwende ich die besprochenen Limits, um über gepulste Interferenzexperimente mit Massen über 1 MDa zu reden, wo ich den Fokus auf Goldcluster als Kandidatensystem lege.

Contents

1 Introduction

Quantum physics has, since its inception in the early 20th century [3, 4], greatly enriched the scientific world. Growing from its beginnings in exploring new concepts and possibilities of the world on the nanoscale[5], it has shown itself to be a formidable and resilient theory, with a strong series of successes and discoveries cementing it as the pillar it is today. The reach of quantum physics nowadays is truly vast. Branching out into the realm of high energy physics with quantum field theory [6], it has served as the basis for the standard model of particle physics, one of the most well-tested and accurate models to date. Meanwhile, 'regular' quantum mechanics has continued to delve deeper into the mechanics of more complex systems, be they Bose-Einstein Condensates or superconductors, pushing quantum theory further and further toward the macroscopic. Added to this are the technological advances that quantum physics has brought into being, giving the scientific world a growing toolbox of extremely precise and sensitive systems to use and control, atomic clocks being one such example.
In all of this explosive growth of the field, both in the breadth of scope and size of systems, many questions remain. Why do these effects of quantum systems vanish at large scales? Why can we not observe them in our daily lives? The interplay of quantum mechanics and gravity is another such question. How can one reconcile the worldview of general relativity, which has shown its accuracy many times, and quantum physics? The two great theories of our time seem incompatible, so how do we join them together? While these questions remain unanswered, the search for answers is ongoing, with no effort too large ref[7, 8].
Attempts to explain the transition from a quantized to a classical world are many. One close-at-hand explanation is decoherence[9]. Here, the isolated quantum system becomes entangled with an uncontrolled noisy environment, which leads to a loss of observable information and can serve as an explanation for why quantum effects seem to vanish for large systems. This is a powerful explanation for the loss of quantum control in systems [10, 11], but as the process is based on entanglement, we are left with a more complex quantum system, not a classical one. Another explanation is Continuous Spontaneous Localization [12, 13](CSL). Here a stochastic term in the Schrödinger equation, dependent on the size of the system, randomly causes the collapse of the wavefunction. Such a term may even be linked to gravity [14, 15] to possibly reconcile general relativity and quantum mechanics. Until now quantum mechanics has weathered every test thrown at it, and the search continues through many avenues([16], [17]).
This brings the story to matter-wave interference, which can serve as one avenue of approach for testing the limits of quantum physics. It is a prime example of the strange nature of quantum systems, as it displays the wave-like behavior of massive objects under certain conditions. This was predicted by Lois deBroglie 100 years ago [18]. In his work, he connected the momentum

of a particle to a characteristic wavelength that would govern the behavior of its wavefunction

$$\lambda_{dB} = \frac{h}{p} \tag{1.1}$$

This at the time groundbreaking hypothesis was soon proven to be true with the example of electron diffraction[19, 20]. This set off an avalanche of experiments attempting interference experiments for more complex and massive systems [21, 22] during which the boundaries of the possible were pushed forward and new knowledge gained[23] neutron gravity, fermion. One of the great success stories for matter-wave interference is atom interferometry [24, 25], where continued effort lifted the experiments from proof of possibility into the realm of extreme precision measurements [26, 27], as the control of the atomic systems grew by leaps and bounds. Optical atom interferometers benefited from the increased control brought about by the improvements of laser techniques and atom optics[28, 29], allowing experimenters precise control of their systems. Today, it is feasible to use atom interferometers as powerful sensors[30], able to detect minute differences in local fields[31] and sensitive to small scales[32]. They can probe the nature of gravity with absolute measurements and tests of the equivalence principle, and are used to search for cosmological specters like dark energy [33, 34].

Interferometry experiments beyond the scope of atoms are an important research direction [35]. The nature of atom interferometers makes them less suited for scanning the parameter space of macroscopicity, as the mass of the systems has a larger impact than the spatial separation of the wave packets. By performing interference experiments with systems of great complexity and mass[36, 1, 30], it will be possible to probe the physics that atom interferometers are not sensitive to, be it the push towards the macroscopic world and attempting to find the boundary of quantum and classical reality or probing forces and systems for which large systems λ_{dB} provide an overwhelming advantage[37].

For this to become possible, it is necessary to make interference experiments with large and massive systems a possibility, a not-so-trivial task. Realizing interference experiments becomes ever more difficult as the de Broglie wavelength of the system grows smaller. The experiments take longer, the wave function becomes more fragile, and the system becomes less controllable. To prevail in the face of these challenges, new techniques for particle control and interference experiments must be found. Near field interference experiments[38, 39], based on the Talbot Lau[40] effect of optics, have shown great promise in pushing the limits of interference with massive systems towards higher masses due to their improved mass scaling. Experiments with systems of increasing size and complexity have pushed the mass limit for interference towards $\simeq$25000 Dalton[1], and efforts to go further are continuing[41, 8]. The efforts in the Arndt group in Vienna are split between continuous experiments in the long baseline universal matter-wave interferometer (LUMI)[42, 1] and pulsed experiments in the all-optical time domain matter wave interferometer (OTIMA)[43, 2]. These two approaches complement each other and make it possible to perform experiments with a large variety of systems, from as small as atoms to truly massive molecules. This thesis will focus on my efforts at the OTIMA experiment to show the results achieved and to find new avenues to push the complexity and size of systems accessible in the laboratory to new regimes. To begin, chapter 2 will give an introduction to the theory behind the OTIMA experiment. Starting with a primer on diffraction, the concept underlying

the interference experiments, I will move on to show how it may lead to interference, describing both the near and far field regimes of interference. The focus will then shift to the near-field regime and the Talbot Lau effect, which forms the basis of the near-field interferometers used by the Arndt group in Vienna. After motivating the use of standing light waves as gratings and time domain experiments, the journey of a particle through the interferometer will be shown in the Wigner formalism[44]. Here, the various parameters and effects that shape the observed interference fringes will be discussed, and different methods of quantifying them. The distinction between classical shadow and quantum fringe oscillation is an important facet of Talbot Lau interferometers, and ways to distinguish between the two possibilities will be shown. The adaptation of theory to match experimental reality will finish this section of the thesis.
Chapter 3 presents the experimental realization of a pulsed interferometer with light gratings in the example of OTIMA, showing how the individual components come together to make interference experiments possible for a variety of molecules. Here, I will highlight the experimental and practical considerations that influenced the final shape of the interferometer and the challenges to overcome for performing interference measurements with massive systems. The first part will deal with providing the stable source conditions required for molecular beam experiments. Here I will focus on work with bio-molecules and ways to deal with their fragility to achieve an intense and stable beam of neutral molecules for the experiment. Following this, I will describe the interferometer conditions necessary for interference measurements and how to achieve them in the lab. The focus here lies on creating the best possible gratings and optimizing the timing feedback control of the experiment to ensure a viable interference measurement.
An example of high mass interference and its challenges will be presented in chapter 4, with the interference of gramicidin, a large polypeptide, serving as a prototype for protein interference[2]. This chapter will give specific insights into the process of realizing interference measurements with such a fragile and complex molecule, showing the steps necessary to reach the current point and highlighting the efforts required for future endeavors with proteins.
Chapter 5 will focus on the first steps of the journey to protein interference. Here, the necessity for new grating mechanisms and unlocking proteins for neutral experiments in the gas phase is discussed. A potential approach for this is shown, photolabile tagging for charge transfer after cleavage[45], a way to make proteins interact with photons of a variety of wavelengths. After explaining the concept, I will introduce the test setup and method used to quantify the suitability of the chemical tag method. Initial results for a variety of test molecules are shown and discussed.
The content of chapter 6 is a different source mechanism, aimed at experiments with much more massive systems. Here, I discuss tests of a potential source of size-selected nanoparticles for optical experiments. I begin by giving an overview of the current best methods[46, 47, 48] for particle generation and highlight the potential benefit of alternative methods. This is followed by a description of the method and its origins[49, 50] and the parameters relevant to our goals. The experimental setup is shown, where I focus on how the control of key parameters can reliably influence the source conditions. The need for precise control and readout for the experiment is discussed, as well as how it can be achieved. Showing the results, I first highlight the fundamental suitability of the technique as a vacuum-compatible source and further describe quantitative tests of parameter space control. To finish, I discuss the future potential

and direction in developing the technique and discuss possible applications.
Chapter 7 is an exploration of interferometer possibilities and designs for future experiments. I first introduce the limitations inherent to large mass interference experiments[51, 52, 53]. I will then describe possibilities for a pulsed protein interferometer, building on chapter 5. Here, I will more closely treat the requirements for interference experiments to access proteins and sketch a road map toward possible interference with insulin.
Ending with chapter 8, I will give an outlook for the potential of interference experiments with massive complex systems as a tool for obtaining information about the particles themselves[54]. Here I focus on proteins and the potential to extract electric[55, 56], magnetic[57], geometric and optical properties[58, 59]. Following this, I look further into the future and discuss the potential of pulsed cluster interferometry with masses exceeding 1 MDa. Here I begin by describing the requirements for choosing a particular metal for cluster interferometry and highlight a particular candidate, gold. Following this, the parameter space for viable earth-bound experiments is mapped, showing the possible breakpoints for interferometry with massive systems. After showing the constraining factors of such experiments, I describe possible methods of molecular beam control that may be used to prepare the beam parameters to suit a tabletop experiment.

2 The theoretical model of a pulsed Talbot Lau interferometer

This chapter gives a summary of the fundamental physics needed to understand the mechanics of pulsed beam sources and matter-wave diffraction in a near-field interferometer of the Talbot Lau scheme. It will focus on treating the physics in the time domain to better relay the physical realities of pulsed interferometers.

2.1 Diffraction in the far and near field

As OTIMA is a diffraction experiment at heart, it is prudent to revisit the concept of 'diffraction' and the relevant scales and nuances that lead to the more specific picture shown in this chapter. We will first introduce diffraction in general, then work towards near-field interference in the Talbot Lau scheme.

2.1.1 Diffraction

Diffraction is a phenomenon first discussed for classical waves of light[60] and later in the realm of quantum physics with matter waves[18, 20]. To start with, I will use the classical terminology of diffracted light for a more intuitive picture.
We begin with a plane wave E that propagates forward in direction z. It can be seen as composed of a series of overlapping spherical wavelets that create the plane wavefront. To observe diffraction we require an object, or obstacle to the plane wave as at its core diffraction is the interaction of a wave and a diffracting object. Once the propagating wavefront encounters the object, it will 'bend' at the edges of the obstacle, leading to effects inside its geometric shadow.
Treating this event with more detail, let us restart at the beginning. According to the Huygens-Fresnel principle, we can describe the wave $E(\vec{x})$ the following way: each point on the wavefront may be described as a collection of spherical wavelets from points that make up the source. As the wave propagates towards the particle and intersects with it, parts of the wave are blocked. In this event, the transmissive area $S(\xi, \eta)$ of the obstacle may be seen as a starting point for new sources for wave propagation $E(\xi, \eta)$. The overall propagation is now different from the incoming wave, as some spherical wavelets no longer contribute to the wave.
How the wave changes is determined by the object's in-plane transmission function and its size, given by A, and the wavelength λ. The modulation is dependent on the distance L after the object, first rising as the wavelets immediately around the obstacle contribute, then decreasing

when the contribution of far away wavelets increases. Putting this into a mathematical form we obtain

$$E(\vec{x}) = \frac{-i}{\lambda} \int\int_S \frac{e^{-ikr}}{r} E(\xi,\eta) d\xi d\eta \tag{2.1}$$

To simplify the integral, let us make some assumptions. At large enough distances L, we can transition to the paraxial approximation $r \simeq z$ outside the exponent. Using the Fresnel approximation in the exponent allows us to rewrite the integral as follows

$$E(\vec{x}) = \frac{-i}{\lambda z} \int\int_S \exp\left(-ik\left[\frac{-x\xi - y\eta}{z} + \frac{-\xi^2+\eta^2}{2z}\right]\right) E(\xi,\eta) d\xi d\eta \tag{2.2}$$

Observing this integral we can distinguish two cases, depending on the distance L. In the case of $z >> x, y$ we can assume that only the linear terms offer a significant contribution to $E(\vec{x})$. This regime, known as Fraunhofer or far-field regime, deals with wave fronts that are flat to such a degree that curvature effects may be neglected. The well-known double slit experiment [61] is a clear example of flat wavefront interference. It is in this regime that Mach-Zehnder [62] and Ramsey-Borde interferometers [63] operate.
Moving closer towards the aperture however makes the picture more complicated. Here, the wavefronts are still curved so the second-order terms of the expansion must be accounted for. This puts us in the near field, or Fresnel, regime of diffraction, where we finally find the Talbot effect.

2.1.2 Near field interference: Talbot and Lau effects

This section will serve as an overview of the effects making up the fundamental principle of the interferometers used in Vienna: the Talbot[40] and Lau[64] effects.
To observe the Talbot effect, one needs only two ingredients: a sufficiently monochromatic plane wave and a periodic structure, such as a grating. If we set the grating in the path of the plane wave, it will lead to diffraction of the plane wave at the grating openings. Then, in the near field behind the grating, these diffracted wavelets will interfere with each other to create a modulation in the light field intensity. This modulation, when scanned over the distance to the grating, takes the shape of a periodic structure, known as the Talbot carpet, shown in figure 2.1. At certain intervals, the free space intensity modulation closely mimics the transmission function of the grating, displaying the same periodicity and a $\pi/2$ phase shift. They occur at multiples of a characteristic distance known as the Talbot length

$$L_T = \frac{d^2}{\lambda} \tag{2.3}$$

and it is at these distances that searching for near-field interference is most fruitful. To observe the Talbot effect, the incoming light must be a coherent plane wave, a prerequisite that has up to now been only replicated with atoms [65].
Here it is useful to look at the Lau effect, a close analog to the Talbot effect, where the plane wave is replaced by a spherical point source. Preparing a molecular point source is a much more manageable task. To obtain it, we may simply extend our interference experiment by another

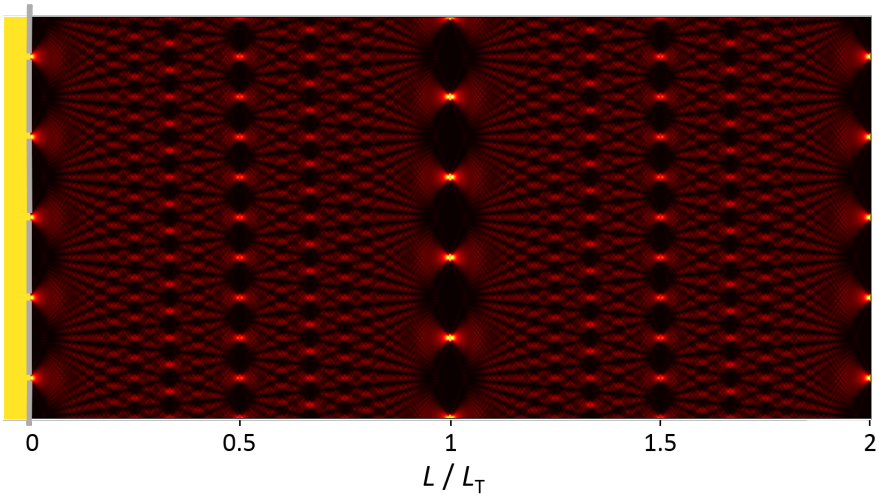

Figure 2.1: Image of a Talbot carpet. A plane light wave passing through the slits from the left leads to diffraction at the slits. Wave interference leads to intensity modulations at multiples of L_T that are reproductions of the grating transmission function. Higher order effects become visible for small opening fractions of the grating, causing the emergence of patterns at distances $< L_T$

step, namely the introduction of an additional grating of the same grating period. With it, it is possible to spatially constrain the molecules in the beam into an array of point-like sources that may then propagate to the second grating and cover sufficient slits coherently to make the diffraction pattern possible.
Now that we have functioning diffraction, the next question is how to quantify said interference fringes. Since the pattern is a reproduction of the grating transmission, it is a spatial modulation on the scale of 100 nm, not resolvable by most particle detectors. To obtain the spatial sensitivity necessary to measure the intensity modulation, a final grating is added to scan over the beam and block it partially. This three grating setup, shown in figure 2.2 is known as a Talbot Lau interferometer. The type of grating used for the interferometer affects which molecules are viable for interference in the setup.
Material gratings are advantageous for smaller nonpolar particles, as they serve as stable absorption masks for the first and final grating. Since transmission is purely based on collision with the grating walls, these gratings are applicable for a wide variety of systems. Material gratings run into problems however when it comes to more massive particles. Dipole polarizability of the molecules promotes unfavorable interactions between grating and molecule[66]. The molecules become sensitive to the uneven charge distribution of mechanical gratings caused by the machining process, leading to loss of interference contrast. The particle size itself may also be a fundamental limit to the use of material gratings[42], as after a certain size they begin to clog the gratings with extended exposure. Optical gratings formed by standing light waves are an alternative approach that can overcome many of these limitations.

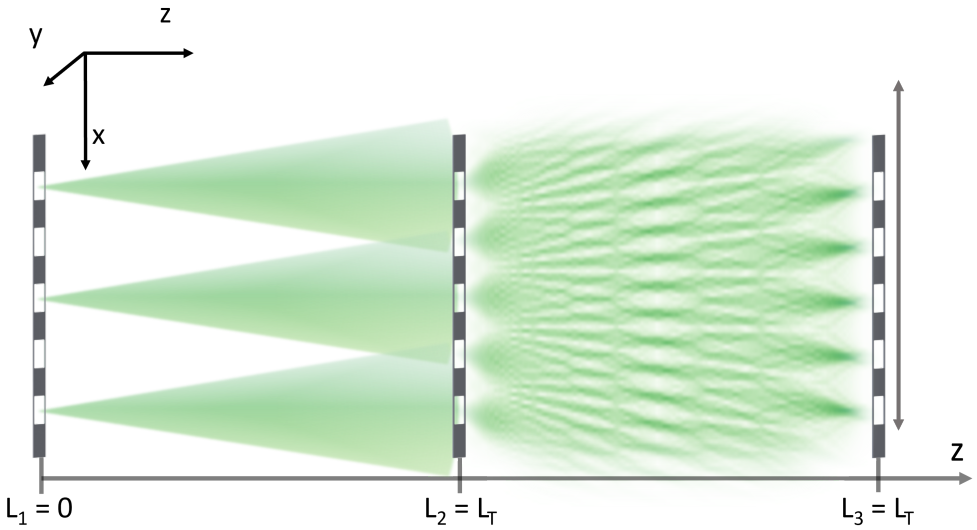

Figure 2.2: Simplified image of a three-grating Talbot Lau interferometer. Particles arrive from the left as an incoherent ensemble. The first grating localizes the particles passing through into point-like sources, with transverse coherence that grows enough at the second grating to allow for the emergence of the Talbot Lau carpet. This nanoscale pattern is scanned with a third grating, making it possible to measure the fringe oscillations using macroscopic detectors

2.2 Light grating mechanisms

Light gratings have long become a staple in atom optics experiments, allowing precise control by targeting the atomic resonances. This allows for both coherent beam splitting mechanisms using Rabi-oscillations[[67] or stimulated Raman transitions [29]. Such experiments are always highly specific to the species of atom in use and therefore lack universal application inside a single experiment. For larger systems composed of many atoms, methods that only target the resonance are much less suited, as the dissipation of the photon energy into the many internal degrees of freedom does not always guarantee a visible change in the system. However, light gratings for molecules still have great potential, as the possible interactions between particle and light offer many opportunities to explore as grating mechanisms[68, 69].
While the interaction of molecules and light is a topic of interest in its own right, serving to learn more about the internal structure of the molecules and dynamics of the electrons, our focus is more specific. To effectively use light as absorptive gratings, we must look for interactions that lead to observable effects on its center of mass motion.

2.2.1 Absorption

For a fully optical interferometer, absorption events are the centerpiece of the experiment. Only by absorption and the subsequent relaxation processes changing the molecule noticeably is

it possible to modulate the intensity of a molecular beam with light. This modulation then makes it possible for light gratings to perform the task required of the first and final grating. It depends on the particle's response to the light field and the intermediate excitation levels before ionization or dissociation [70, 71] For a single photon process, we can look at the population of the ground state

$$\frac{dn_0}{dt} = -\sigma_1 n_0(t)\Phi(t) \tag{2.4}$$

Here σ_1 the one photon cross-section for the transition and $\Phi(t) = P(t)\lambda/hcA$ is the laser fluence, depending on the wavelength λ the pulse power $P(t)$ and the illuminated area A. We assume it to be rectangular over the pulse duration for simplicity, $\Phi(t) = \Phi$ for $0 \leq t \leq \tau$. If we integrate over the pulse duration, we obtain the fluence-dependent term

$$n_0(\Phi) = e^{-\sigma_1 \Phi \tau} \tag{2.5}$$

To obtain the final state population we may use $n_1(t) = 1 - n_0(t)$. Let us now assume a process requiring two photons to eject the particle from the beam. The population equations then look as follows

$$\begin{aligned} \frac{dn_0}{dt} &= -\sigma_1 n_0(t)\Phi(t) + k n_1(t) + \sigma_1 n_1 \Phi(t) \\ \frac{dn_1}{dt} &= \sigma_1 n_0(t)\Phi(t) - k n_1(t) - \sigma_1 n_1 \Phi(t) - \sigma_2 n_1(t)\Phi(t) \\ \frac{dn_2}{dt} &= \sigma_2 n_1 \Phi(t). \end{aligned} \tag{2.6}$$

Here, σ_1 and σ_2 denote the one photon cross-sections for the transitions $0 \to 1$ and $1 \to 2$, while n_i denotes the populations of the ground state (0), intermediate excited state (1) and final state (2). Focusing on $n_1(t)$, we see the excitation from n_0 to n_1 $\sigma_1 n_1(t)\Phi$ and from n_1 to n_2 $\sigma_2 n_1(t)\Phi$, combined with spontaneous and stimulated emission of a photon. To obtain the number of molecules in the final state, we take $n_2(t) = 1 - n_0(t) - n_1(t)$. Starting with all molecules in the ground state $n_0(0) = 1$, we can calculate the fluence dependent probability for reaching n_2

$$P(\Phi) = 1 + \frac{1}{2}(\sec C - 1)\exp\left(-\frac{B}{2}(\cos C + 1)\right) \tag{2.7}$$

With $B = k\tau + (2\sigma_1 + \sigma_2)\tau$ and $C = \arcsin(2\sqrt{\sigma_1\sigma_2}\phi\tau/B)$. For an off-resonant process where $k\tau \gg 1$, this reduces to[70]

$$P(\Phi) = 1 - e^{-\tau\sigma_1\sigma_2\Phi^2/k} \tag{2.8}$$

Higher-order processes are more complicated to calculate but follow the same form [72]. In conclusion, for us higher-order photon effects require more intensity to accomplish the transition to the observable state, be it electron ejection, fragmentation, or both[73]. The optimal condition for a light grating is then that absorption of a single photon removes the particle from detection, which allows efficient modulation of the molecular beam[74]. The two main channels of interest to us are photo-$ionization$ and photo-$fragmentation$. An example of how they work as gratings is shown in figure 2.3.

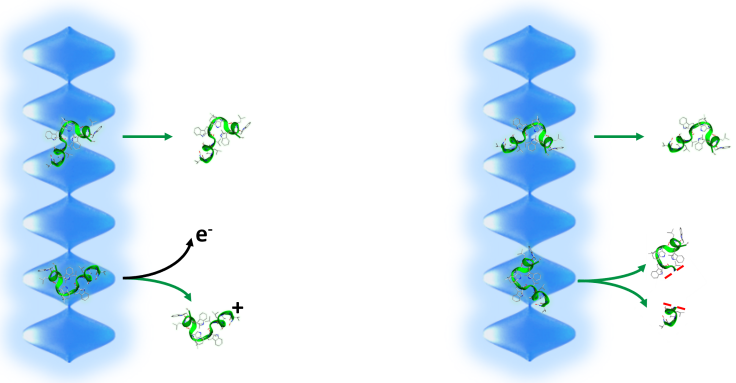

Figure 2.3: Left: image of the working process for photoionization gratings. Particles traveling through the node of the standing light wave absorb no photons and pass by undisturbed. In the antinodes a photon is absorbed, leading to ionization of the particle. The ion can be removed from the beam by applying an external field $\vec{E}$
Right: the working process behind photo-fragmentation gratings. While particles in the node remain whole, in the antinode the photon absorption leads to fragmentation. The fragments can be distinguished from the parent by mass-sensitive detection

Photofragmentation

Photofragmentation is a possible relaxation channel for photon absorption. After absorption, should photoionization not take place, the molecule equilibrates the photon energy across its bonds. If this energy then is higher than the bond strength, the molecule fragments at that point. This gives rise to two possible scenarios for the interferometer. In the first, the fragments both remain in the molecular beam and are distinguishable from the intact survivors by the difference in mass. The second possibility is a full removal of the fragments from the beam due to their relative momenta carrying them out of the detection region[75]. Both scenarios allow us to distinguish between particles traveling through a node or antinode.

Photoionization

Photoinzation is a strongly favored relaxation channel for sufficient photon energy. If the energy exceeds the ionization threshold, the absorption lead directly to the loss of an electron. The remaining system now has a positive charge and is very susceptible to electric fields as a consequence. This makes it possible to use ionization as a beam depletion mechanism. Particles passing through the antinode are ionized and then extracted from the beam via an electric field. The additional utility that photo-ionization brings to the table is the possibility of using it as a detection mechanism. Ionizing the remaining beam after the interference experiment makes it possible to detect it with mass spectrometry techniques[76].

2.2.2 Phase effects

A particle passing through a standing light wave is not only affected by directly absorbed photons. In addition to the absorption results mentioned before, the particle may be affected by the light due to dipole force interactions [77, 78]. These interactions, strongest in the antinodes of the grating, lead to a phase modulation of the molecular beam. The strength of the phase shift is determined by the particle's polarizability at the grating wavelength and the intensity of the standing light wave.

2.3 OTIMA and the time domain

For OTIMA as an all-optical interferometer, the absorptive grating mechanism is realized using pulsed VUV light gratings to allow for off-resonant photo-ionization of a large variety of particles. The pulsed nature of the lasers makes it expedient to treat the experiment in the time domain. The main step to take for this is to change the Talbot length to the Talbot time by

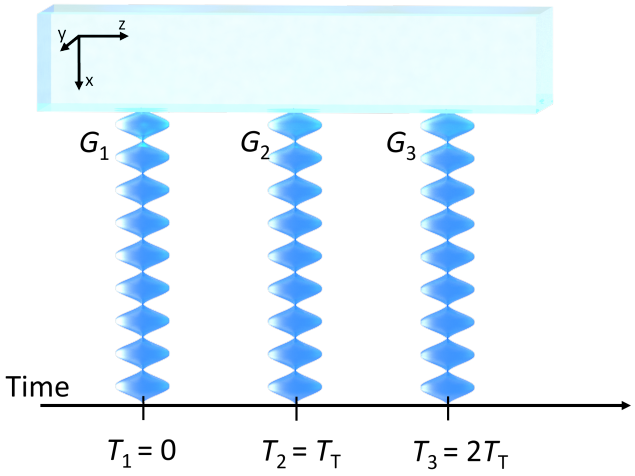

Figure 2.4: Scheme for a pulsed optical interferometer. Here, the gratings are replaced with light pulses forming standing light waves to precisely control the time in between the gratings. The Talbot time T_T is now the relevant parameter for the $temporal$ spacing of the gratings. The high photon energy enables spatial modulation of the beam as it passes through the grating setup, allowing G_1 and G_3 to act as the absorptive masks required to prepare and measure the fringe oscillations.

dividing L_T by the particle velocity v

$$T_T = \frac{d^2}{h} m. \tag{2.9}$$

Here h is Planck's constant and m is the particle mass. The grating period $d = \lambda/2$ is given by the wavelength of the light forming the standing light wave.The new form can be seen in figure

2.4. The Talbot time signifies the time required after the $transverse$ momentum kick of the grating diffraction to lead to a sufficient spread of the wave function to observe interference effects in the form of the revival of the transmission function. Seen from this perspective, the time domain approach is a more direct window into the wavefront evolution than looking at the spatial picture with L_T.

2.4 The mathematical framework of OTIMA

This section will focus on the mathematical description of a pulsed, optical interferometer of the type of OTIMA. It will cover the relevant particle light interactions that form the basis of the diffraction gratings, as well as describe a Wigner function evolution of a particle through the interferometer sequence of coherence preparation, diffraction, and readout. Many [69, 52, 43, 79] of the individual pieces described here have been shown previously, however, I will attempt to combine them all into a cohesive picture of how OTIMA, or any pulsed near field interferometer, functions.

2.4.1 The Wigner formalism

To describe the interactions of particle and light field that culminate in the interference patterns observable in the experiment, I will use the Wigner function representation of the quantum state ρ in one dimension

$$w(x,p) \;=\; \frac{1}{h}\int \mathrm{d}s\; e^{ips/\hbar}\,\langle x-\frac{s}{2}|\,\rho\,|x+\frac{s}{2}\rangle\,. \tag{2.10}$$

It can be seen as the extension from the phase state distribution of a classical particle f, to now describe the quantum state ρ. The advantages of using the Wigner formalism for detailing the phase state evolution throughout the interferometer sequence are twofold. First, this makes it possible to describe the process as a combination of free evolution and grating interactions, providing an intuitive view of the particle's path through the interferometer. Second, the similarity to a classical phase state description allows the smooth transition between both classical and quantum descriptions of the experiment. This makes comparing the expected outcomes, a necessity in a Talbot Lau style interferometer, an easily achievable task.
To let the function evolve through the experimental sequence, two types of transformation actions on the function are necessary. Firstly, a shearing transformation describes the free evolution of the particle in between interactions of the gratings

$$w(x,p) \;\rightarrow\; w(x-pt/m-at^2/2, p-mat), \tag{2.11}$$

where the time t gives the duration of the free evolution. The acting acceleration a springs from global forces acting on the particles, such as gravity or earth's rotation.
The other ingredient for describing the interferometer is the particle's interaction with the diffracting object, the light gratings. It is given by a transformation via convolution with the transmission kernel $T(x,p)$

$$w(x,p) \;\rightarrow\; \int \mathrm{d}p_0\; T(x,p-p_0)\; w(x,p_0) \tag{2.12}$$

The kernel is based on the transmission function, which is given by the nature of the grating and the possible particle grating interactions.

2.4.2 The transmission function

For an optical absorption grating based on single photon depletion, the transmission function $t^{(k)}(x)$ takes the form

$$t^{(k)}(x) \;=\; \exp\left[\left(\frac{-n_0}{2}+i\phi_0\right)\cos^2\left(\frac{\pi x}{d}\right)\right] \tag{2.13}$$

It has two components of note. The eikonal phase factor $\phi_0^{(k)}$ imparted on the molecule by the dipole field leads to a phase shift in the overall pattern. The second is the mean number of photons $n_0^{(k)}$ absorbed in the antinodes of the grating. It gives the transmission probability after passing through the grating $|t^{(k)}(x)|^2$ and effectively determines the grating opening fraction. Both $\phi_0^{(k)}$ and $n_0^{(k)}$ are determined by particle grating interactions mentioned earlier 2.2

$$n_0^{(k)} = \frac{4\sigma E^{(k)}\lambda}{hcA}, \tag{2.14}$$

$$\phi_0^{(k)} = \frac{16\pi^2 E^{(k)}\alpha}{hcA}, \tag{2.15}$$

and depend on the laser fluence $E^{(k)}/A$ and the particle's absorption cross-section σ and polarizability volume α. Expanding the transmission Kernel into a Fourier series reveals the Talbot coefficients

$$\begin{aligned} T^{(k)}(x,p) \;&=\; \frac{1}{h}\int \mathrm{d}s e^{ips/\hbar} t\left(x-\frac{s}{2}\right) t^*\left(x+\frac{s}{2}\right) = \\ &=\; \frac{1}{h}\sum_n \exp\left(\frac{2\pi i n x}{d}\right)\int \mathrm{d}s\; e^{ips/\hbar} B_n^{(k)}\left(\frac{s}{d}\right), \end{aligned} \tag{2.16}$$

which are described by Bessel functions of the first kind J_n

$$\begin{aligned} B_n^{(k)}(\xi) = \sum_{j=-\infty}^{\infty} b_j^{(k)}\left(b_{j-n}^{(k)}\right)^* e^{i\pi(n-2j)\xi} = e^{-n_0^{(k)}/2}\left(\frac{\sin\pi\xi-\beta\cos\pi\xi}{\sin\pi\xi+\beta\cos\pi\xi}\right)^{n/2} \\ \times\, J_n\left(\mathrm{sign}(\sin\pi\xi+\beta\cos\pi\xi)\frac{n_0^{(k)}}{2\beta}\sqrt{\sin^2\pi\xi-\beta^2\cos^2\pi\xi}\right). \end{aligned} \tag{2.17}$$

The parameter β introduced here gives a measure of the relative strength between phase- and absorptive grating effects

$$\beta \;=\; \frac{n_0^{(k)}}{2\phi_0^{(k)}} \;=\; \frac{\sigma\lambda_L}{8\pi^2\alpha_L}. \tag{2.18}$$

This relation plays an important role in determining the optimal contrast conditions, as depending on the relative strength of eikonal phase and grating absorption the evolution of the interference contrast develops differently in time.

2.4.3 Phase space evolution through a Talbot Lau interferometer

Knowing the basic premise of the interferometer and the necessary formalism, it is now time to follow the journey of a wave packet through the experiment. We begin with a series of assumptions: firstly, the particles are assumed to be point-like, allowing for a clean center of mass treatment of the wave function. Secondly, changes in the transverse component of the molecule wave function may be neglected, or the eikonal approximation is assumed to hold. Finally, the y-z position of the particles in the grating is assumed to be unimportant to the particle grating interactions.
The particle starts its journey through the interferometer as a beam with an initial position spread $X_0 \gg d$ and a momentum spread $P_0 \gg h/d$. As both are much larger than the relevant grating sizes we see it as an incoherent mixture of states indistinguishable from the classical case. We can describe it with the initial Wigner function $w_0(x,p) = D(p)/X_0$. The transverse momentum distribution $D(p) = \int \mathrm{d}p\, \mu(p, p_y, p_z)$ is gained by integrating over the momentum density distribution, and will be of significance further along the journey.
Once the molecules arrive at the first grating G_1, the interaction between grating and particle will lead to a interaction of particles and grating in the way described in (2.12), leading to the transformation.

$$w_1(x,p) = \int \mathrm{d}p_0\; T^{(1)}(x, p-p_0) D(p_0)/X_0 \tag{2.19}$$

After leaving grating one behind, the journey continues towards the second grating G_2 and is described by free evolution as in 2.11. The remainder of the journey happens in much the same way, first interacting with the transmission Kernel of G_2, followed by another free evolution. This gives us the penultimate form of the Wigner function in front of the final grating G_3

$$\begin{aligned} w_3(x,p) \;=\; & \frac{1}{X_0} \int \mathrm{d}p_1 T^{(2)} \left(x - \frac{pT_2}{m} + \frac{a}{2} T_2^2 . p - p1 - maT_2 \right) \\ \times \int \mathrm{d}p_0 T^{(1)} & \left(x - \frac{pT_2}{m} - \frac{p_1 T_1}{m} + \frac{a}{2}(T_1^2 + T_2^2).p_1 - p_0 - maT_1 \right) D(p_0). \end{aligned} \tag{2.20}$$

To obtain the spatially modulated signal that is measured experimentally, we integrate our function over the momentum coordinate. Here it is useful to introduce the Fourier transform of the initial momentum distribution

$$\tilde{D}(x) \;=\; \int \mathrm{d}p e^{-ips/h} D(p), \tag{2.21}$$

which as an effect of the large initial momentum distribution is very narrow $h/P_0 \ll d$. Now we can integrate and obtain the final form of the Wigner function

$$\begin{aligned} w_3(x) = \frac{1}{X_0} \sum_{\ell,k} \tilde{D} \left(\frac{kT_1 + \ell T_2}{T_T} d \right) B_k^{(1)} \left(\frac{kT_1 + \ell T_2}{T_T} \right) B_{\ell-k}^{(2)} \left(\frac{\ell T_2}{T_T} \right) \\ \times \exp\left(\frac{2\pi i}{d} \left[\ell x - \ell \frac{a}{2} (T_1 + T_2)^2 + (\ell - k) \frac{a}{2} T_1^2 \right] \right). \end{aligned} \tag{2.22}$$

Here we can see the importance of $\tilde{D}(x)$ for our signal. For a very narrow distribution, only a very small range of index pairs ℓ and k can meaningfully contribute to the function(Ref). This can be interpreted as the particles being out of $resonance$ with each other, leading to interference patterns that do not overlap in phase. This causes the higher-order terms of the Fourier sum to vanish and leaves only the transmitted signal.
In general, it is much more common for the fringes to lack this stable phase condition due to this limitation. Observing a meaningful fringe oscillation is only possible in certain $resonant$ configurations $k = -N\ell$, which ensure a phase locking in between the individual patterns. This finally leads to the preferred configuration of OTIMA, the symmetric grating separation with $k = -\ell$.

$$w_3(x) = \frac{1}{X_0} \sum_{\ell} \tilde{D}\left(\frac{l\tau}{T_T} d\right) B_{-\ell}^{(1)}\left(\frac{\ell\tau}{T_T}\right) B_{2\ell}^{(2)}\left(\ell \frac{T+\tau}{T_T}\right) \exp\left[\frac{2\pi i}{d}(x + \Delta x\right]. \tag{2.23}$$

The value Δx is the total fringe shift of the fringes. It is composed of a static phase difference between the three gratings Δx_s and the contribution due to accelerations caused by effects such as gravity or Coriolis. Should the initial momentum distribution possess a mean transverse momentum component $p_\theta \neq 0$, the shift is modified.

$$\Delta x = \frac{a(2\Delta T + \tau)^2}{2} - \frac{p_\theta \tau}{m} + \Delta x_s. \tag{2.24}$$

The time τ is the detuning between the grating times, which for $\tau = 0$ are set to be at symmetrical pulse separations $\Delta T = T_2 - T_1 = T_3 - T_2$. We see that the transverse momentum p_θ only scales with this detuning, as the normally symmetric grating configuration cancels out phases linear in time.
To measure the signal we now only need to let $w_3(x)$ pass through G_3 by performing one final convolution

$$\begin{aligned} S(x, \Delta T, \tau) &= \sum_{\ell} S_\ell \exp\left[\frac{2\pi i \ell}{d}(x + \Delta x(\Delta T, \tau))\right] \\ S_\ell &= \tilde{D}\left(\frac{l\tau}{T_T} d\right) B_{-\ell}^{(1)}\left(\frac{\ell\tau}{T_T}\right) B_{2\ell}^{(2)}\left(\ell \frac{\Delta T + \tau}{T_T}\right) B_{-\ell}^{(1)}(0). \end{aligned} \tag{2.25}$$

It gives us the probability of a particle successfully passing through all three gratings in the interferometer sequence.

2.4.4 Interference contrast

Having obtained the signal after the third grating, we are now only a single step away from quantifying the interference contrast. To extract the intensity modulation, we can scan the phase of the final grating and measure the signal at different points. From this it is possible to extract the Visibility

$$\mathcal{V} = \frac{S_{max} - S_{min}}{S_{max} + S_{min}}, \tag{2.26}$$

which can be likened to the sinusoidal visibility, or the first order Fourier terms in 2.25. This view is valid for the case of moderate grating strengths,

$$\mathcal{V}_{\text{sin}} = \left|\frac{2S_1}{S_0}\right| = 2\left|\tilde{D}\left(\frac{\tau d}{T_T}\right)\frac{B_{-1}^{(1)}\left(\frac{\tau}{T_T}\right)B_2^{(2)}\left(\frac{\Delta T+\tau}{T_T}\right)B_{-1}^{(3)}(0)}{B_0^{(1)}(0)B_0^{(2)}(0)B_0^{(3)}(0)}\right|, \tag{2.27}$$

where the higher-order Fourier contributions are negligible. For high grating strengths, 2.27

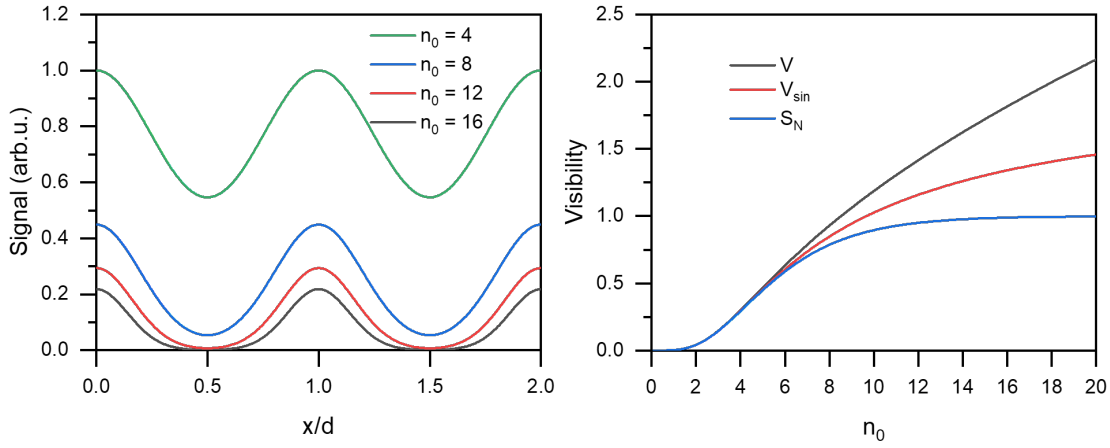

Figure 2.5: Left: Signal at G_3 for various grating strengths. It can be seen that the signal already begins to deviate from a sinusoidal form at $n_0 \simeq 8$ and transforms into isolated peaks for $n_0 > 10$. Right: A plot of $\mathcal{V}$, $\mathcal{V}_{\text{sin}}$ and S_N as a function of n_0. We see the change in signal reflected in the measures of visibility. Once S_{min} reaches 0 the conventional visibility saturates, while $\mathcal{V}_{\text{sin}}$ and continue to grow.

becomes a poorer estimate as the higher order contributions become more significant and the signal less sinusoidal. This can be seen in figure 2.5, where the influence of the grating strength on both signal and visibility is shown. A more accurate measure of the fringe oscillations in this case is the *normalized Contrast*

$$S_N = \frac{S_I - S_{\text{avg}}}{S_{\text{avg}}}, \tag{2.28}$$

where the fringe signal S_I is compared to the mean of the overall signal. This can be seen as a generalization of 2.26 with its simple form of the average. This contrast measure accounts for the change in fringe conditions due to the higher order Fourier terms and does not saturate like $\mathcal{V}$. To obtain S_N, we can perform the same measurements and adapt the formula.

Remembering 2.17, we see that the fringe oscillations are dependent on the parameter β, the relative strength of absorption versus eikonal phase. Different values of beta shift the maximum fringe oscillations away from T_T. This may lead to a reduced resonance time in the case of $\alpha > 0$, or extend the evolution for maximum contrast for $\alpha < 0$, as shown in figure 2.6. Another important factor to consider for measuring interference is the effect of the grating strength

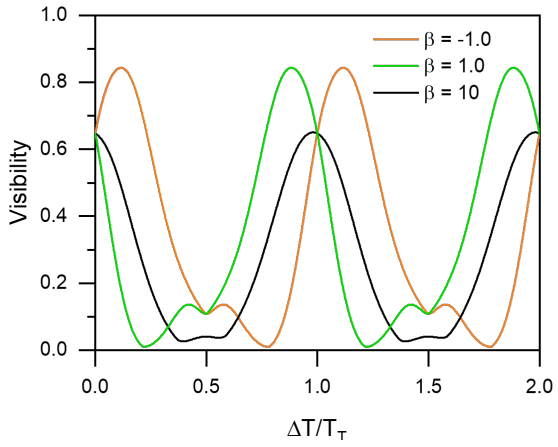

Figure 2.6: Time scan of the fringe contrast for different values of β. We see that for high absorption versus phase effect $\beta = 10$, the strongest contrast is found at $\Delta T = T_T$. With the stronger influence of the eikonal phase $\beta = 1.0$, we can see a shift in the pattern. The maximal contrast is reached before, for $\beta > 0$ (green), or after T_T for $\beta < 0$(orange). The visibility at $\Delta T = T_T$ is independent of β. $n_0^{(k)}$ was set to 6.0 for all gratings.

on visibility and transmission. Knowing where to expect the best contrast while retaining an appreciable signal is crucial for realizing the best possible version of the experiment. The effect of different grating strengths is shown in figure 2.7. We can see that G_1 and G_3 contribute differently to the interference contrast to the inner diffraction grating G_2, saturating their effect on $\mathcal{V}$ much earlier. This is due to their different contribution to the final signal, with G_2 retaining higher orders beside the pure transmission $B^{(k)}(0)$. Since the visibility saturates at higher grating strengths for G_2 it is advantageous to work with gratings of $differing$ strength, with higher n_0 for G_2 than the outer gratings.

Once again, β is important to consider, as it makes the consideration of the choice of $n_0^{(2)}$ more nuanced. Changing the pulse separation ΔT to match the optimal resonance may improve the contrast yield for higher transmissions significantly but reduce it instead for stronger gratings.

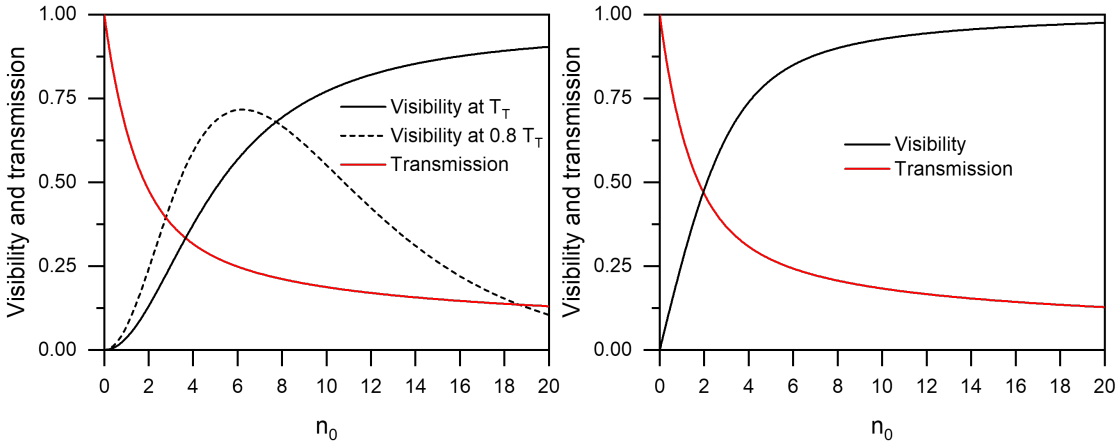

Figure 2.7: Left: Plot of fringe contrast at T_T(solid blue) and $0.8T_T$(dashed blue), and transmitted signal for G_2. At the integer resonance, we can see that the visibility is growing significantly until $n_0 \simeq 9$, or 20% transmission. In the case of $0.8T_T$, the contrast increase is sharper up to $n_0 = 6$, after which the higher grating strength causes the resonance to shift closer to T_T, reducing the visibility. Right: Visibility and transmission plotted for varying n_0 for G_1. Here we can see the visibility rising and saturating much faster than in the case of G_2. The pure transmission influence on the outer grating saturates quicker and makes them act as a magnifying factor for the true diffraction grating. The grating strength of the other gratings was set to $n_0 = 6$ for both plots.

Quantum and classical fringe modulation

In a three-grating setup like OTIMA, it is possible to observe another form of fringe modulation[52], caused by the Moiré shadow effect of the three overlapping gratings. As this shadow may mimic the fringe oscillations expected from matter wave interference, a closer look is needed to properly distinguish the two possibilities. Here we can look at the classical counterparts of the Talbot coefficients 2.29

$$C_n^{(k)}(\xi) = \sum_j B_{n-j}^{(k)}(0) c_j^{(k)}(\xi), \;\; c_j^{(k)}(\xi) = \frac{1}{d}\int_{-d/2}^{d/2} \mathrm{d}x \exp\left(-\frac{2\pi i n x}{d} - i\xi \frac{q^{(k)}(x) d}{h}\right). \quad (2.29)$$

They are composed of the grating transmission coefficients $B_n^{(k)}(0)$ and a classical momentum kick $q^{(k)}(x)$. In the limit of $\xi \to 0$, $C_n^{(k)}(\xi)$ and $B_n^{(k)}(\xi)$ are largely identical, converging to the pure transmission $|t^{(k)}(x)|^2$. This changes for larger ξ, where the different dependence on it becomes relevant. While the Talbot coefficients are periodic, the classical coefficients are not. We can translate $B_n^{(k)}(\xi) \to C_n^{(k)}(\xi)$ with $\sin(\pi\xi) \to \pi\xi$ and $\cos(\pi\xi) \to 1$. This difference affects both the strength of the contrast and how it evolves with varying delay times from the diffracting grating and is shown in figure 2.8. In the classical case, the contrast is high at low pulse separations and drops off for larger separations. It does not display the characteristic

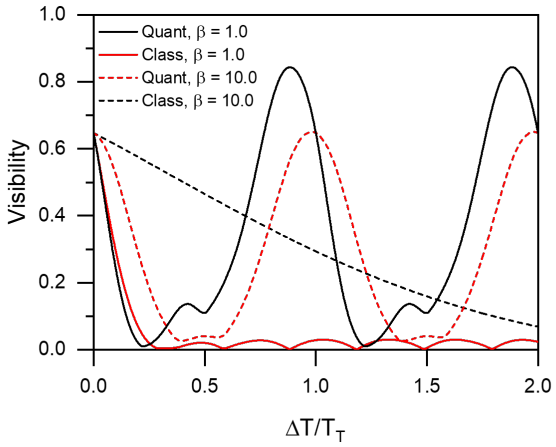

Figure 2.8: Visibility time scan for quantum visibility (solid line) and classical shadow (dashed line). The classical shadow is largely identical for small ΔT but drops continuously and does not show true phase revivals. The quantum visibility shows periodic revivals even at higher ΔT. Once again β plays an important role, with large values giving a strong classical shadow.

revivals one can see from the Talbot carpet. However, it still pays to be careful as the in case of high β the classical shadow only slowly degrades and may still show strong overlap with the quantum fringe oscillations.
The nature of the fringe oscillation can be tested by varying different parameters to observe the behavior of the fringes. One method of verifying the quantum nature of the fringe oscillations is a symmetric time scan. As 2.8 shows, the contrast evolves differently for classical and quantum scenarios. Performing several measurements for varying ΔT, we can map out this behavior and distinguish between quantum and classical cases. This is usually a difficult method to realize, as the experimental conditions must be varied significantly to make such a scan.
Another method relies on the different dependence of the classical and quantum case on the grating strength. By varying n_0 for a series of interference scans, the resulting contrast can be matched to one of the possibilities. As can be seen in figure 2.9, this process can distinguish between classical and quantum case very well for low β, while for high values care must be taken. In this case, both classical and quantum expectation show the same qualitative behavior for varying grating strength, with the classical visibility smaller but still significant. Observing fringe contrast on the order of 20 There, the choice of timing may be crucial. At pulse separations $T \neq T_T$, the power dependence once again is markedly different for quantum oscillation and classical shadow.

One other, qualitative difference between quantum interference and classical shadow is the emergence of higher order fringe oscillations. Observing the Talbot effect once more, we can see that it is possible to obtain fringe modulation at fractional Talbot orders. At $T_T/2$ the grating transmission function is reformed at a fractional periodicity d/2. This effect is impossible to replicate with a Moire shadow for a symmetric grating configuration. This then is a fundamental difference in fringe contrast that may serve to easily distinguish quantum and classical cases.

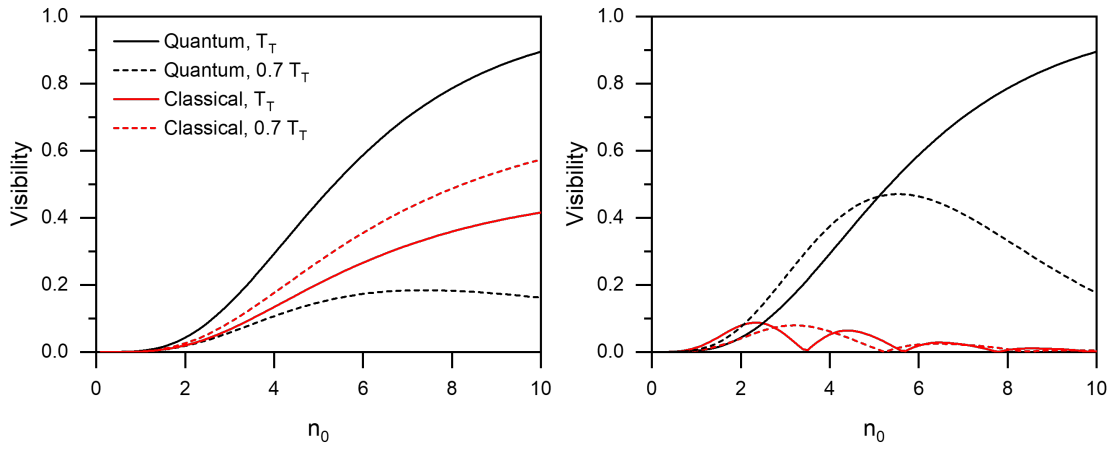

Figure 2.9: Left: power scan of the quantum (black) and classical(red) fringe visibility for $\beta = 1$, at resonance(solid) and at 0.7 T_T(dashed). We see that for low values of β the classical shadow is limited in visibility and reduces for $n_0 > 4$. An energy scan can clearly distinguish between the quantum and classical expectation.
Right: power scan of the fringe visibility for $\beta = 10$. Here we see the classical visibility follow the same qualitative change at $T = T_T$, growing for higher n_0. In the case of $T = 0.7T_T$ it becomes possible to distinguish between quantum and classical cases again, with the quantum visibility saturating and decreasing as n_0 grows while the classical shadow keeps gaining in strength.

The periodicity of the fringe modulation is closely tied to the opening fraction of the gratings or the average number of absorbed photons. While fringe contrast can be observed already starting at low values of $n < 6$ (see Figure 2.10), the higher order Fourier terms are negligible still. Only for high numbers of absorbed photons $n > 6$ in the grating antinodes do the contributions increase sufficiently for the fractional fringe oscillation to become pronounced. In the case of a Moiré shadow, the reduction in the opening fraction reduces only the contrast but leads to no change in periodicity. Figure 2.10 shows the signal at G_3 using both classical and quantum treatment at $T_T/2$. Here we can see that at a certain point the fractional order appears in the quantum case, whereas the classical case shows only a decrease in signal strength.

Adapting theory to experiment

The formalism presented up to this gives us knowledge on what to expect in an idealized setting and serves well to provide qualitative predictions. To obtain a true quantitative prediction of the measured interference fringes, several parameters still need to be accounted for. These parameters deal with the imperfect nature of the experiment, caused by limitations of the lasers, the source, or the interferometer.
One limitation is given by the nature of the OTIMA experiment. While a single mirror makes it very sturdy towards vibrations, it prevents the ability to scan the grating phase easily over the signal at G_3. As the currently given method of quantifying the visibility relies on shifting

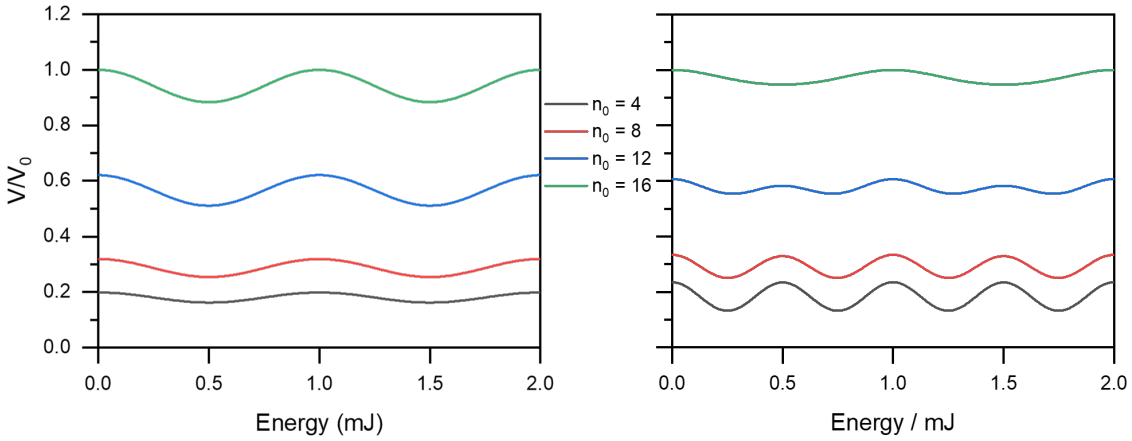

Figure 2.10: Left: Quantum signal at $T_T/2$ for various grating strengths n_0. We can see that for lower n_0 the fractional order has yet to separate from the broad first order resonance. For a stronger grating, the higher order fourier terms gain in size and a pattern of $d/2$ periodicity emerges. Right: Classical signal at $T_T/2$. Here we mainly see a sharp decrease in signal as the grating 'slits' become smaller. While there is a periodic signal modulation, it does not change in nature for higher n_0, instead remaining with a period of d

the phase of the final grating, it is not truly possible to realize in the OTIMA setup. This means an alternate measure of interference is needed. Here the sharpness of the resonance conditions $\tilde{D}(x)$ offers a solution. By slightly varying the detuning τ of the grating pulses between resonant and off-resonant and making two complementary measurements, we can compare the interference fringe signal S_I with the average transmission signal S_{avg}, and use 2.28. To perform such a resonance dip measurement, only slight detunings in the grating pulse timings are necessary, leaving the particles effectively stationary between the two modes.
A limit for this method is the vertical alignment of the gratings. The gravitational free fall during propagation adds a time-dependent phase to the experiment 2.24, which may, in combination with the other phase contributions, leave the resonant signal identical to the mean. We can use the non-zero transverse momentum p_θ as a way to overcome this limitation. Changing the detuning τ, we can scan the phase of the final grating linear in time and overcome the fixed grating limitation. The process is shown with an example resonance dip measurements in figure 2.11. As an all-optical interferometer, the quality of interference measurement is tied to the quality of the standing light waves[79]. While the fundamental parameters of grating strength and wavelength are already accounted for, the standing wave fidelity is also of importance. To quantify this value we must look at two parameters: the interferometer mirror reflectivity R, governing how much of the light is turned into a standing wave; and the standing wave coherence C, which gives a measure of the average quality of the standing light wave across the molecular beam. Accounting for these factors the effective light field is modified

$$E(x) = (1-R)E_0 + R\left[2(1-C)E_0 + 4RC\cos\left(\frac{\pi x}{d}\right)\right] \tag{2.30}$$

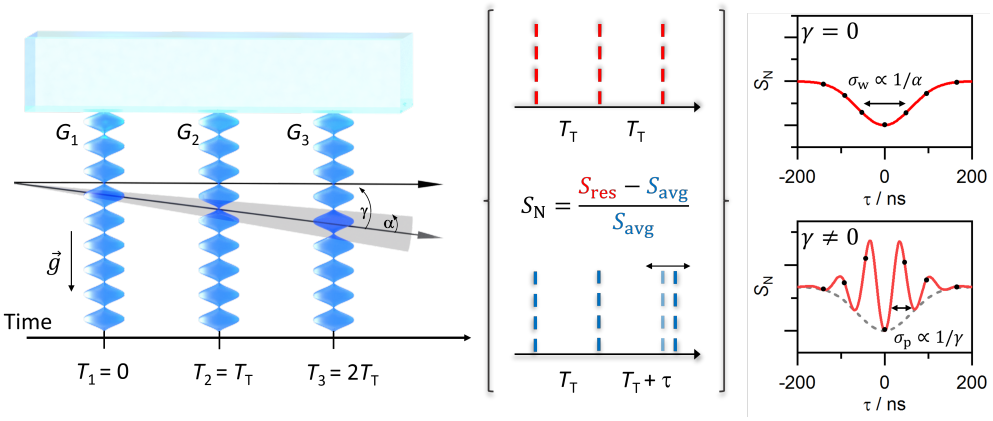

Figure 2.11: Left: Scheme for measuring interference fringes with phase locked gratings. The beam traversing the three grating setup has a transverse momentum distribution, or *divergence*, described by the angle α and an average transverse momentum, described by the *tilt* γ The measurement process is split into two modes: resonant to obtain S_{int}, and reference S_{ref}, where a variable detuning τ is introduced. The signals of the two modes are compared using 2.28, with S_{ref} acting as S_{avg}. With different values of τ, the dip resonance can be scanned. In the case of $\gamma \neq 0$, the grating phase can be scanned also.

We see contributions from the non-reflected light leading to overall signal depletion and the incoherent contribution to the standing light wave, likewise only reducing the transmission. In the end, we have the contribution of the actual standing light wave. This can be incorporated into the mathematical formalism by introducing the $effective$ values for absorption n_0 and phase shift ϕ_0 of the standing light wave

$$n_{eff}^{(k)} = RC\frac{4\sigma E^{(k)\lambda}}{hcA}, \quad \phi_{eff}^{(k)} = RC\frac{16\pi^2 E^{(k)}\alpha}{hcA}, \tag{2.31}$$

which influence the diffracting behavior of G_2, and therefore the maximally observable contrast. The transmission probability is only minimally affected, due to the usually high values for R, since no other parameters change the effective field strength of the gratings. To account for this, the effective number of n_{eff} for the transmission function is modified by the standing wave visibility V

$$n_{eff} \to V n_{eff} = \frac{1+R}{2RC} n_{eff} \tag{2.32}$$

The coherence of the standing light field gives the biggest contribution to a loss of effective grating strength. To ensure it remains at an acceptably high value, we must position the particle beam close to the mirror surface.

3 The OTIMA experiment

In this chapter, I will give an overview of the individual parts of the OTIMA experiment. I will focus on the technical requirements each component has to make interference possible, as well as how to make them work together for measurements of the quantum fringe oscillation for various molecules.

3.1 Experimental overview

The Experiment, seen schematically in Figure 3.1, is divided into three segments, housed in individual vacuum chambers. The source chamber (SC) houses the different sources used to produce the stable, intense beams of molecules required for the experiment. It is pumped down to 10^{-7} mbar using two turbo molecular pumps. The main chamber (MC) houses the interferometer mirror, as well as the particle detection. The chamber is pumped to 3×10^{-9} mbar by three turbo molecular pumps to prevent collisional decoherence [80]. To minimize the vibrations of the turbo molecular pumps, which may lead to dephasing[81] of the interference fringes, they are mounted on vibration-dampening stages, reducing the amplitudes by a factor of 10.
The mirror is mounted on a platform that allows 2d-movement orthogonal to the direction of molecular beam propagation. Using this mobility, it is possible to optimize standing wave coherence and mirror surface quality for the experiment. Two collimation stages are present in the chamber, consisting of vertical and horizontal slit arrays with varying width that are mounted on translation stages. This makes it possible to tailor the molecular beam geometry to perfectly match the illuminated grating area. To detect the remaining particles after the interferometer sequence, the beam is ionized with a 157 nm running wave for detection in a Time of Flight Mass Spectrometer (ToF-MS). The beam area of detection can be controlled to match the spatial extension of the light gratings, ensuring no particles are detected that did not interact with the interferometer sequence. The laser beams are aligned into standing light waves in the optics chamber (OC), pumped to 10^{-4} mbar to minimize attenuation of the light pulses.

3.2 Molecular beam sources

The molecular beam sources in use at OTIMA and tested for use beyond share one main aspect: they are pulsed, with a small opening time on the order of 10 µs to allow for an experimental cycle without contamination from previous experimental runs. This also highlights one of the key limiting factors for a pulsed interferometer: choosing a source that can produce suitably time-constrained packages of particles to send on their way through the interferometer sequence.

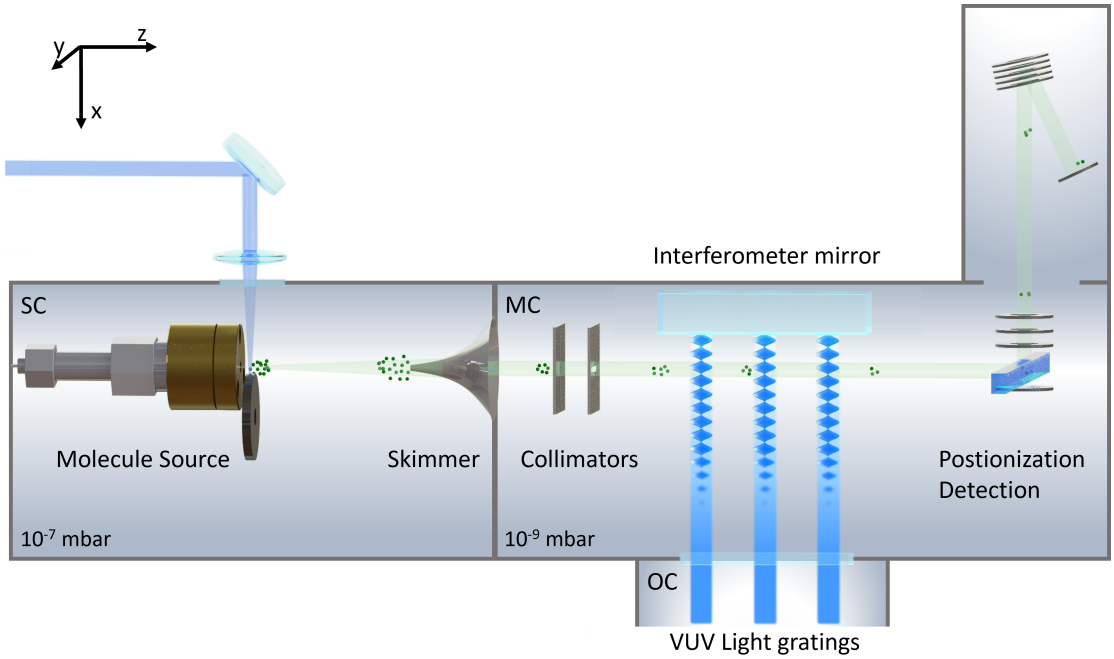

Figure 3.1: Image of the OTIMA interferometer setup. The individual components of the experiment are housed in separate chambers. The particle beam created with laser ablation and supersonic expansion in the source chamber (SC) passes through a skimmer To enter the main chamber (MC). Here, the beam is shaped with a vertical and horizontal collimation stage to ensure maximal overlap of the grating pulse and molecular beam. Passing under the interferometer mirror, the molecules are illuminated in sequence by three VUV laser pulses, aligned into standing light waves in the optics chamber (OC). The surviving molecules are ionized using a running wave of the same wavelength and detected in a time-of-flight mass spectrometer.

This will be the main focus of this section: highlighting several pulsed molecular beam sources and their different properties.

3.2.1 Laser desorption from a plate source

One method of creating the pulsed molecular beam is laser desorption from a plate source. This method shares many similarities with Matrix-Assisted-Laser-Desorption ionization (MALDi) method, ubiquitous in mass spectrometry studies of proteins[82]. A target plate is first coated with the molecular species of interest. To transfer the molecules into the gas phase, ultraviolet laser pulses with ns or fs duration are used. The ns light pule is provided by a tunable optical parametric oscillator (OPO) system from $EKSPLA$. The laser is capable of producing light pulses at 355 nm with a peak pulse energy of 40 mJ and a 5 ns pulse duration. The light is focused onto the target plate to create the necessary intensity for desorbing the molecules. Alternatively, a 343 nm pulse with femtosecond duration from a Pharos laser from $Light\ Conversion$ can be

used to enable softer desorption conditions[83]. It has a pulse duration of 290 fs, with 70 µJ peak pulse energy. The resulting plume is sharply defined in time, ensuring no cross-contamination of the signal between experimental cycles. After desorption, the molecules travel towards the interferometer with velocities given by a Maxwell-Boltzmann distribution modified for molecules leaving a surface [84]

$$F(v) \propto \left(\frac{m}{k_B T}\right) v^3 \exp\left(-\frac{m(v-v_s)^2}{2kT}\right). \tag{3.1}$$

Here, T is the temperature, and v_s is the stream velocity of the adiabatic expansion. The velocity distribution is broad due to the high local Temperature after desorption, exceeding 1000 K at the beginning of plume formation[85, 86]. This makes it possible to match the Talbot resonance condition 2.9 of the molecule with a velocity existing in the beam without changing the alignment of the light gratings. To operate the source with optimal signal lifetime and intensity, the target is placed on a programmable motorized stage, allowing for x-y movement. Tuning the scanning speed and step width of the motor movement enables us to find the best conditions for a given particle species.
In this configuration, the source chamber is very compact and can be vented and evacuated rapidly. This makes it possible to prepare new samples with good speed and return to measurements soon after. However, this source type does not work for all species of molecule, as the velocity spread can be disadvantageous. Considering the velocity selection of the detection scheme of 0.5%, for some molecules the signal does not suffice for accumulating the statistics necessary for interference measurements. This can be alleviated by extending the data collection to longer runs, but that increases the influence of drifts in the interferometer, suppressing the fringe oscillations.

3.2.2 Supersonic expansion

Larger, more fragile molecules, such as polypeptides and proteins, are more difficult to volatilize without destroying them[85]. This is due to a combination of several factors. One is the increased sensitivity to the desorption conditions. Larger biomolecules are prone to fragmentation when exposed to intense laser light[85]. This means that fewer intact molecules leave the target surface and enter the gas phase. Large molecules are also much less abundant on the target plate for a given coating compared to smaller species. These factors all combine to a reduced signal yield for experiments with large complex molecules.
To mitigate these issues, we can adapt the source mechanism by adding a pulsed supersonic noble gas jet[87]. Here, the gas undergoes adiabatic expansion from a high-pressure region into the vacuum, leading to significant cooling of the forward and transverse temperatures. The high-pressure gradient ensures a large forward velocity of the gas. By matching the timing of desorption with a gas pulse, we can inject the molecules of interest into the gas jet. The rapid collisions between carrier gas and seeded molecules have a range of useful effects. The hot molecules are cooled due to the collisions, which prevents further fragmentation and reduces the velocity spread significantly. The velocity can again be modeled using 3.1, where now v_s is the velocity of the carrier gas, and T its temperature.
Here the source takes a different shape, shown in figure 3.2 The particles are coated onto a

felt wheel, acting as a particle reservoir for the source. The felt wheel is in contact with a glassy carbon wheel, coating it with a thin, even layer of molecules. The carbon wheel then acts as the target for the desorption laser, rotating to keep refreshing the target area. After desorption, the particles are picked up by a noble gas jet undergoing adiabatic expansion, which turns the seeded molecules into a directed beam of sharply defined velocity. The adiabatic expansion is produced by an Even-Lavie valve[88], with precisely timed pulses of high-pressure gas that expand into a vacuum of 10^{-7} mbar. The desorbed molecules enter the high-pressure

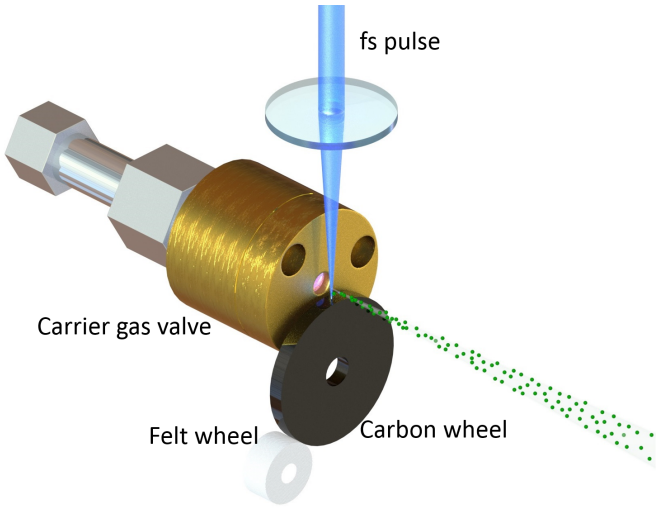

Figure 3.2: Image of the supersonic source configuration. The particles are deposited onto a felt wheel reservoir, where they are picked up by a rotating glassy carbon wheel to form a thin film. The wheel serves as a desorption target to create a plume of molecules, which are then picked up by a high-pressure gas jet, that undergoes adiabatic expansion into the vacuum. With this, the molecules to reach equilibrium with the carrier gas due to collisions and form a beam of fast molecules with low-velocity spread. A version of this image was published in[2]

region of this expansion, where they then interact with the surrounding gas by collisions. The particles are cooled in all degrees of freedom during this process, however with different efficiency[89]. The strongest effect is on the translation degrees of freedom, owing to their continuous energy spectrum. Here, cooling the particles down to the temperature of the carrier gas is possible. The temperature of rotations is less accessible, as the usual energy spacing of 0.001 to 0.01 eV is harder to bridge with collisions, leading to a higher final energy after freeze-out. Molecule vibrations are the least affected by this cooling process, with their larger energy spacing between 0.01 and 0.1 eV. They become inaccessible to collision cooling very early in the expansion process. This leads to the temperature relation $T_{\mathrm{trans}} < T_{\mathrm{rot}} < T_{\mathrm{vib}}$ for the molecules exiting the source.
This is still a marked improvement over the case of simple desorption from the target plate, as in this case the molecules bleed off the energy in their degrees of freedom only via expansion and remain hot[86]. The velocity distribution for supersonic expansion is very narrow compared

to a thermal source and compresses the total signal into a smaller velocity range. This gives a significant improvement in effective signal and makes a larger variety of molecules available for interferometry. The velocity of the molecular beam is predominantly given by the velocity of the carrier gas jet, accounting for a velocity slip [90] for larger seed molecules, and can be tuned by controlling the carrier gas. By adjusting the nozzle temperature or changing the type of carrier gas for lighter or heavier systems like helium or krypton, it is possible to change the mean velocity significantly and improve rotational and translational cooling. The high gas load caused by the expansion increases the background pressure from 10^{-7} to 10^{-5} mbar during operation. The skimmer, placed between SC and MC, prevents the formation of shock waves in the beam.

3.3 The interferometer

3.3.1 Pulsed light gratings in OTIMA

As a pulsed Talbot Lau interferometer, OTIMA requires optical depletion gratings that can be tuned to match the experimental requirements for grating strength, evolution time, and position.

The grating lasers

OTIMA consists of three separate lasers that are guided toward the interferometer mirror by sets of remotely controlled mirror stages. We use $GAM\ EX50$ vacuum ultraviolet (VUV) excimer lasers housing a cavity filled with a fluorine-helium gas mixture. The gas is a mixture of 99.88 vol$\%$ helium and 0.12 vol$\%$ fluorine. The ratio is tuned for high output energy and stability. To reach a maximal pulse energy of 3 mJ, the laser cavity is filled with up to 3 bar pressure. A 16 kV discharge from electrodes inside the cavity ignites a plasma, which creates excited dimers of fluorine[91]. The discharge timing is controlled using a hydrogen thyratron for high timing accuracy, giving a timing jitter lower than 5 ns FWHM.
The dimers emit photons with several wavelengths upon de-excitation, with the main emission lines at 157.63 nm[92], with $\simeq 80\%$ of the total intensity, followed by 157.52 nm with $\simeq 20\%$. The lines have a FWHM of 0.85 pm, leading to a longitudinal coherence length $L_{CL} = 1$ cm. The lasers have a flat top beam profile with a rectangular 9 mm $\times$ 4 mm beam shape. With a distance of $\simeq$ 1.4 m from laser to interferometer mirror, the transverse coherence amounts to 13 $\mu\mathrm{m} \times 29\ \mu\mathrm{m}$, large enough that all molecules see a coherent wave.
Due to the nature of the light pulse generation, namely the molecular F_2 transition, all three lasers emit at the same wavelength, unaffected by thermal drifts or differences in discharge parameters[92]. This makes them very suitable for creating standing light wave gratings, as matching the grating period of individual gratings is of vital importance to prevent phase averaging effects. The lasers were chosen to maximize photon energy and minimize the grating period while retaining the necessary pulse energy for efficient gratings.
The high photon energy of the laser pulses with 7.8 eV makes it possible to ionize a large variety of different molecules. Since ionization is one viable method of modulating the molecular beam, VUV standing waves can select sources of pointlike wavelets at G_1, and read out the final

intensity at G_3. The second advantage of the short wavelength comes from the correspondingly short grating period. Since the required time separation between grating pulses scales with d^2, a small wavelength has a strong effect on how compact the interferometer can be made to be. With $\lambda = 157$ nm and a period of $d = 78.8$ nm, the first-order Talbot time is only 15.57 ns/Da. This relaxes the velocity requirements for the molecular beam sources, as even fast beams only have a short travel distance between grating pulses.
Using F_2 excimer lasers, one needs to overcome several technical limitations. Molecular oxygen is strongly absorptive for photons of 157 nm wavelength[91], creating ozone. This absorption results in a penetration depth of less than 1 mm distance in air. To prevent this, all laser beam lines must be cleared of oxygen, either by flushing them with molecular nitrogen which is inert to the laser radiation, or evacuating them all. We have chosen the second method, as it gives the option of reliably attenuating the laser pulse energies by introducing a controlled flow of room air into the beamlines.
The limited coherence length L_{CL} imposes more significant limitations. The standing light wave visibility is reduced below 1/e at a 5 mm distance from the mirror surface. To perform meaningful experiments, a high standing-wave coherence is necessary, as the grating strength is limited. A more acceptable coherence > 0.6 is reached closer to the mirror surface at $<$3 mm. Guiding the molecular beam past the interferometer mirror at that distance increases the risk of particles contaminating the mirror. It also limits the available space to introduce optics for shifting the phase of grating G_3 [93]. This makes it impossible to scan the phase mechanically, which we circumvent by performing interference measurements in two modes. 2.11

3.3.2 CaF_2 Optics

There is only a small selection of viable materials for 157 nm optics. The choice for OTIMA was CaF_2 dielectric optics, for a reflectivity of 95%. Transmission optics such as focusing lenses and vacuum windows require high-quality substrates to maximize the transmission. Under optimal conditions, it reaches 95%. The quality of optics at this wavelength is poor compared to quartz optics and wavelengths above 200 nm. This leads to a loss in pulse energy from the laser output port to the interferometer mirror of $\simeq$33%, as alignment and focusing of the light gratings requires six optical components. Absorption of VUV photons leads to adsorption of hydrocarbons onto the substrates[94], creating a black coating over several months, a problem especially visible in high vacuum where self-cleaning is missing. Regular cleaning or replacement of the optics is needed. Exposing the optics to ozone or oxygen during laser operation was shown to be an effective method [95], as well as plasma cleaning [96].

3.3.3 Interferometer mirror

The interferometer mirror, a 4 by 7 cm rectangular CaF_2 mirror with a 5 by 3 cm clear aperture, is the heart piece of the interferometer. It is here that the light pulses of the lasers are turned into standing light waves to create the gratings that the molecules interact with on their journey through the experiment. The properties of the mirror have a tremendous influence on the quality of the gratings and thus on the quality of recorded interference fringes. The reflectivity must remain high to produce a clean standing light wave to act as a grating for the molecular

beam. In the case of OTIMA, the mirror reflectivity reaches 95% under optimal conditions. The second requirement is the surface roughness of the mirror. There are two different regimes to observe[79]. Firstly, the molecules are not stationary during the duration of a laser pulse. During this time, they will average over the static phase of the grating along their beam path. With velocities of ≃600 m/s, a molecule can travel ≃3 µm while interacting with the light grating. To prevent a loss of contrast, the mirror has to be smooth to < 10 nm over this distance. The second limitation is given by the fact that the molecules in the beam and during different

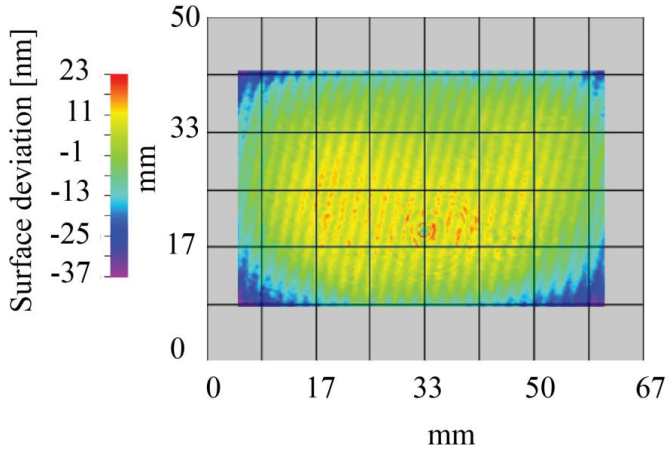

Figure 3.3: Measurement scan of the surface quality for one interferometer mirror used in the experiment. The 4 by 7 cm mirror shows deformities of the mirror surface below 8 nm. The visible fringes are an artifact of the imaging method used. Images provided by $LASEROPTIK\ GmbH,\ Garbsen, Germany$

cycles may interact with the light gratings at different points on the interferometer mirror due to the 9 mm extension of the light gratings along the flight path. This means that the mirror needs to be flat to below 10 nm not over 3 mum but 5 mm within a single grating and also over the entire mirror surface. The mirror in use in OTIMA, shown in figure 3.3, fulfills these strict requirements to allow for flexible alignment of the light gratings.

3.3.4 Alignment

The laser pulses are guided towards the interferometer mirror through evacuated beam lines to prevent loss of energy due to absorption by molecular oxygen. This makes it necessary to remotely controllable mirror mounts to ensure proper and stable alignment. Before entry into the main chamber, the beams enter the alignment stage. Here they are guided through a two-mirror system to adjust position and angle for optimal depletion and standing wave quality. During this stage, cylindrical lenses focus the beams to a point ≃5 cm behind the interferometer mirror in one axis, while leaving them spatially extended along the flight path of the molecules. The focused beam has a 300 µm by 9 mm beam profile and ensures a high intensity for interference experiments. The quality of the standing light wave alignment can be evaluated by observing the fluorescence on the window separating the high-pressure region of the optic

box from the ultra-high vacuum region of the main chamber. The individual fluorescence spots from the incoming and outgoing beam serve to more easily align the beam path into forming a standing light wave. Also, the temporal alignment needs to fulfill the resonance condition for interference. To observe and match the timings, a set of UV photodiodes monitor the laser beam lines. This enables us to match the pulse timing with the nanosecond precision that is required to prevent phase-averaging effects due to the transverse velocity.
Alignment of the three gratings for maximal spatial and temporal overlap requires optimization in several iterations to ensure the stability and quality for interference measurements.

3.4 Detection of molecules

In OTIMA we detect ions with mass sensitivity to match the mass of the signal with the correct grating pulse separation. To ionize the molecules that have passed all three interferometer pulses, we direct a fourth F_2 laser beam into the repeller region of a time-of-flight mass spectrometer. This $Coherent\ Existar\ 50X$ has a peak pulse energy of 2 mJ and a flat-top beam profile of 3 mm$\times$ 10 mm dimensions. The ions are detected in a Time of Flight Mass Spectrometer (ToF-MS, $Kaesdorf\ Munich$), which is operated in orthogonal mode. The ions travel through a Wiley McLarren[97] configuration with two acceleration stages coupled with a reflectron, giving a mass sensitivity of $\Delta m/m = 1/5000$. Mass calibration is achieved using reference molecules of known mass m_{C}, such as Buckminster fullerenes, to compare to the arrival time of the mass of the interfered particle m_{I}. From the time of flight, we then obtain

$$m_{\mathrm{I}} \;=\; m_{\mathrm{C}} \frac{T_{\mathrm{C}}^2}{T_{\mathrm{I}}^2}. \tag{3.2}$$

The ion signals are sent to the computer using an analog-to-digital converter. For each measurement, a tag allocates the signal to the reference S_{avg} or interference S_{int} mode. It is important to compare the counts of the two measurement modes in the experiment to achieve a reliable measure of interference contrast using 2.28. With multichannel plates (MCPs) as detectors, the signal is not a direct measure of the amount of simultaneous detection events.
To obtain a more accurate particle count, we treat the MCP response with an error estimation algorithm. Assuming a maximum of a single particle per experimental frame, the mass spectrum is compared against a threshold value. It is determined by taking the standard deviation of the spectrum baseline with no mass peaks. This is used to distinguish detection events, tagged with '1'. Signals that do not meet the required threshold are tagged with '0'. Comparing the number of detection events with the total number of frames, we can compute the likelihood of a '0' event, P_{zero}. As actual detection '1' events are rare, we can set $P_{\mathrm{zero}} = \exp(-\eta)$ according to Poisson statistics. From this, we can extract η, the average number of detected ions per measurement. This allows us to quantify the number of ions N in the measurement run equal to $-M \ln(P_{\mathrm{zero}})$, a now standardized measure of particle counts. We can then use the value N for error propagation to obtain the error bounds of the contrast measurements.

3.5 Timing control

Precise timing is of vital importance for interference experiments in the time domain, where nanosecond precision is required to ensure the interferometer remains stable. The timing pulses are given by three synced *Berkely Nucleonics* series 575 pulse generators with 50 ps timing jitter. The pulse generators control all relevant events in the experimental run, which can be seen in figure 3.4 There are two main issues to account for during our interference runs. The

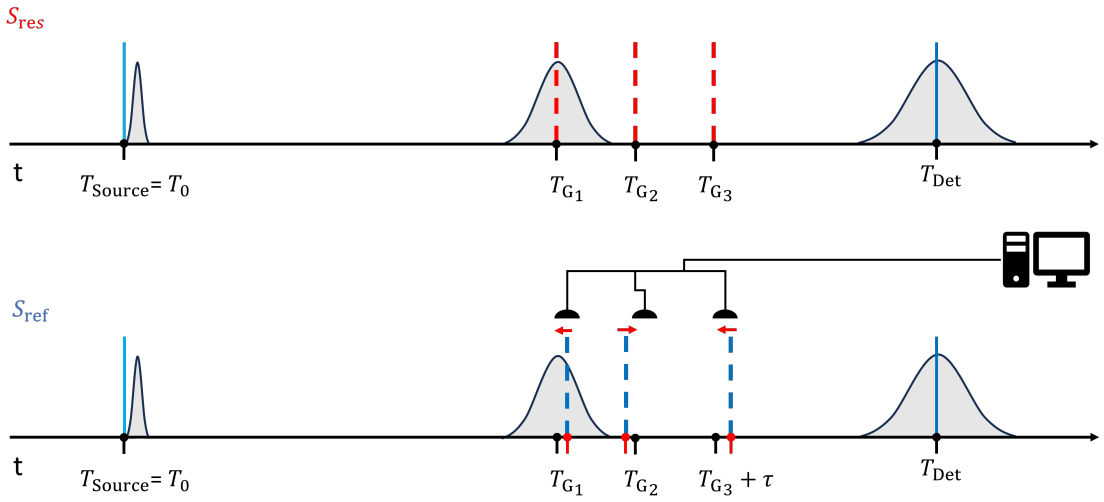

Figure 3.4: Timing scheme of the OTIMA experiment. The experiments run in two alternating timing configurations to measure S_{res} and S_{ref} simultaneously. The timing of the grating pulses T_{G_1}, T_{G_2} and T_{G_3} is recorded using fast response photodiodes, which feed the information into the control program[98] to adjust for timing shifts in the pulse timings. The arrival time distribution widens as the molecule cloud travels through the interferometer. To ensure a good overlap between each grating pulse, the final detection pulse is set to a smaller spatial extension, only detecting molecules that have interacted with all three gratings.

first is laser timing jitter, a random time uncertainty of the actual laser pulse timing around the intended pulse time. To prevent averaging over several phases due to the transverse velocity, the lasers must be stable with timing jitters below 5 ns FWHM. The pulse timing is also affected by long-term drifts of the F_2 excimer lasers. During operation, the changing temperatures in the system cause a drift in the pulse timing of the lasers. This gradual change may ultimately lead to a complete loss of the required resonance condition of the interferometer.
To compensate for this, we utilized a feedback loop consisting of a set of photodiodes with nanosecond response time that feed the laser timing information to the control program [98]. The pulse timing of the laser is automatically read out and adjusted by sending the new correct time to the pulse generators. This system is also able to observe the timing jitter and mark the measurement by assigning a jitter class, making it possible to select only the measurements with suitable timing quality for readout.

4 Matter wave interference of gramicidin

In this chapter, I will give an overview of the interference of gramicidin, a large natural antibiotic. Quantum interference was achieved for the first Talbot order T_T and at $T_T/2$. These results have been shown elsewhere [2], and serve as a good example of the experimental procedure for interference experiments and highlight the limits and potential for pulsed interference experiments with biomolecules in the future.

4.1 Gramicidin A1

Gramicidin A1, seen in figure 4.1, is a large polypeptide, which is excreted by *bacillus brevis* as protection against other bacteria. With a mass of 1882 Da and composed of 15 amino acids, it is already a very complex and fragile bio-molecule. The high abundance of tryptophan, the sole amino acid that can be single photon ionized with energies below 7.8 eV[99], makes it responsive to the grating and detection scheme of OTIMA. These factors made gramicidin an attractive choice for interference and made it a useful prototype for protein interference experiments.

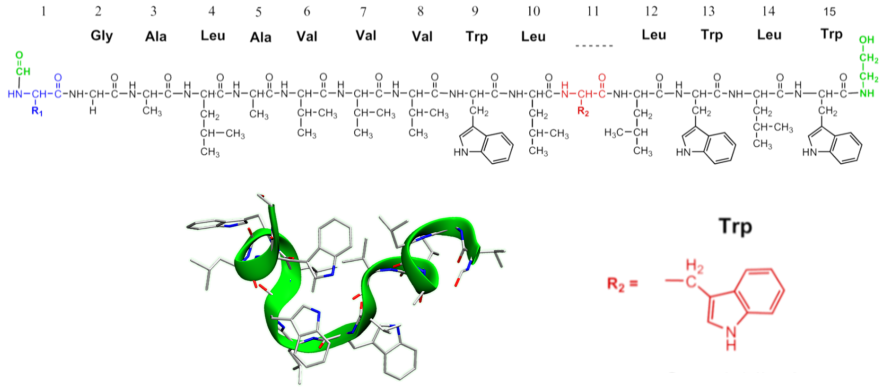

Figure 4.1: Image of the polypeptide antibiotic gramicidin. At the top, we see the chain of 15 amino acids making up the molecule. The high abundance of tryptophan (Trp, bottom right) makes gramicidin ionizable using single 157 nm photons and allows us to use it in the OTIMA setup. Bottom left: simulated image of the folding structure of gramicidin. We see that with 15 amino acids, a complex folding pattern occurs.

4.2 A source for fragile polypeptides

Complex biomolecules are very sensitive to changes in their environment. While thermal evaporation of dipeptides and functionalized tripeptides has been observed[100] even for vapor pressures useful for matter-wave interferometry, biomolecules of higher complexity are too fragile to be evaporated in an oven. However, fast and ultra-fast laser desorption followed by cooling in an adiabatic expansion gas, described in section 3.2.2, has allowed us to form neutral polypeptide beams of sufficient intensity and stability[101].

4.2.1 Short and ultrashort pulse desorption

Initial experiments based on ns-desorption showed the viability of the technique for creating beams of fragile polypeptides but also some limitations. During the pulse duration, the molecules in the illuminated area have ample opportunity to dissipate the energy into their environment. This reduces the quality of the molecular beam. The most relevant effect is the spallation of substrate clusters[82]. They do not contribute to the molecular beam, as they are too large to be carried along by the carrier gas, but they make up a significant fraction of the ablated material. To still obtain a good signal, the pulse energy must be increased, leading to faster sample depletion. The experiment has to be frequently interrupted to refresh the source by reapplying the sample. As this process changes the alignment, this method is unsuitable for interference measurements.
Ultrafast fs pulses improve the signal in two ways: The fraction of isolated molecules is increased, boosting the overall signal, and the low pulse energy of $\simeq 15\ \mu$J reduces ablation, which slows the rate of sample consumption. This leads to a more long-lived signal with fs desorption, as can be seen in figure 4.2, where the signal lifetime was tested in the case of fs and ns desorption. Not shown is the overall increase in absolute signal. With the improvement in signal lifetime and intensity brought on by fs desorption, it became possible to extend the interference measurements.

4.2.2 Beam velocity

In order to perform the interference measurements at different pulse separations T_T and $T_T/2$ the molecular beam velocity needed to be adjusted significantly to match the grating alignment of OTIMA. To change the velocity, we switched the carrier gas used for the supersonic expansion between argon for measurements at T_T, and helium for $T_T/2$. The mean velocity in these cases was $\simeq 550$ m/s for argon and $\simeq 1200$ m/s for helium. For helium, this corresponds to a velocity slip of 30%, while in the case of argon, the slip is negligible. Only minimal realignment was necessary to switch between the two measurement runs.

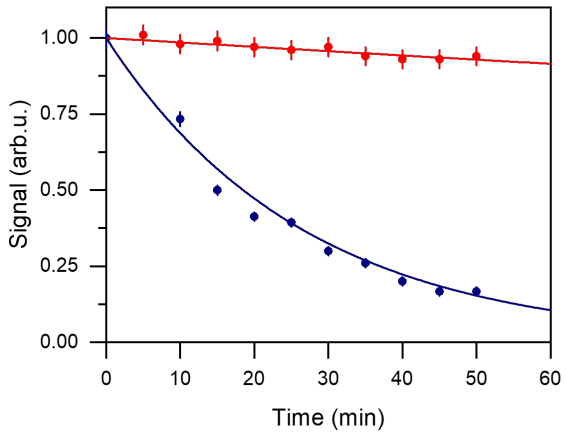

Figure 4.2: Signal decay rate for fs(red) and ns(blue) desorption. The signal decays rapidly in the fs case, due to the large required pulse energy and consequently high ablation rate. The signal half lifetime of the decay fit corresponds to $\simeq$ 27 minutes. With fs desorption, the signal lasts significantly longer, remaining above 90 % strength for 60 minutes, corresponding to the time of one interference measurement. The half-life time for this case is well beyond an hour with $\simeq$ 676 minutes, a 25-fold increase over ns desorption. A version of this figure is published in [101].

4.3 Interference measurements

4.3.1 Grating parameters

For interference with gramicidin, it was important to strike a balance between optimal fringe contrast and signal quality. We aimed for grating transmissions of 30%, corresponding to a $n_{\text{eff}} = 2.9$ accounting for the reflectivity $R = 0.94$ and the coherence $C = 0.7$ [79]. This served as a good compromise between the grating strength required to distinguish quantum interference from a classical shadow and retaining enough molecular beam intensity. With 30% transmission, the signal is strong enough to accumulate the statistics required for one measurement within 10 minutes. Scanning the interference resonance is then well within the time frame of a strong molecular beam source.

4.3.2 Verifying quantum fringes

To measure and verify the nature of the fringe oscillations, eleven separate measurements at different detunings τ were made to scan the resonance dip and extract the visibilities. Each measurement consisted of an interference measurement to obtain $S_{\text{int}} = S(\tau_{\text{int}})$ and a reference measurement $S_{\text{avg}} = S(\tau_{\text{avg}})$. For the measurement at the first Talbot time $T = T_T$, τ_{int} was varied from -100 ns to 100 ns in 20 ns steps. Measuring at the fractional Talbot order $T = T_T/2$, τ_{int} was scanned from -50 to +50 ns in 10 ns steps. For $T = T_T$ and $T = T_T/2$, the detuning of the reference measurements τ_{avg} was set to -200 ns and 100 ns, respectively. To extract the

fringe contrast from the measurements, we applied a sinusoidal fit with a Gaussian envelope.

$$S_{\mathrm{N}} = V_0 \times \exp\left[-\left(\frac{-\tau}{\sigma_{\mathrm{w}}\sqrt{2}}\right)\right] \times \cos\left(2\pi\frac{\tau}{\sigma_{\mathrm{p}} + \phi_{off}}\right) \tag{4.1}$$

The amplitude V_0 is a measure of the fringe contrast. The width of the resonance dip σ_{w} gives information about the molecular beam divergence α, and σ_{p} reveals the molecular tilt γ

$$\alpha = \arcsin\left(\frac{d}{2v\sigma_{\mathrm{w}}\sqrt{2\ln 10}}\right) \ , \ \gamma = \arcsin\left(\frac{d}{v\sigma_{\mathrm{p}}}\right) \tag{4.2}$$

The interference measurements, shown in figure 4.3, show a good match between the data points and quantum expectation for both first and fractional Talbot orders. The fit parameters from

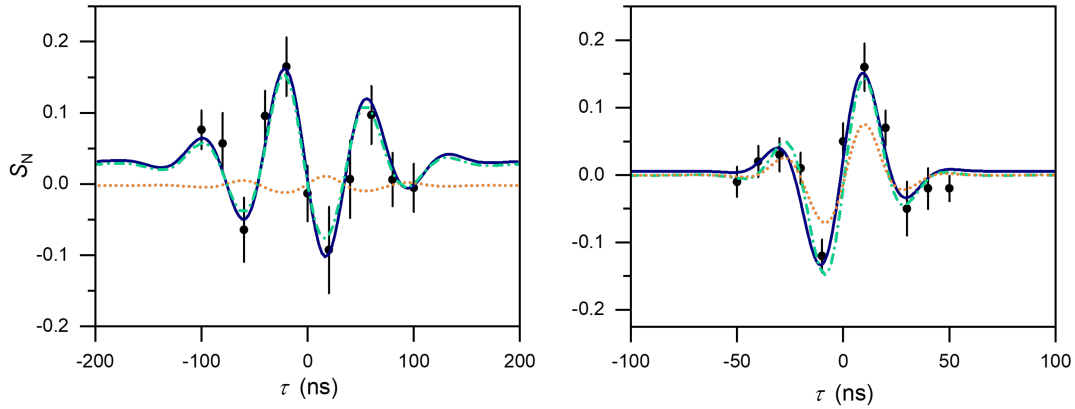

Figure 4.3: Interference dip measurements of gramicidin with 1-σ error bars, plotted together with a fit to the data using 4.1(solid line), as well as simulated fringes for quantum (dashed line) and classical (dotted line) cases. Left: Full order $\Delta T = T_T$ dip scan of the fringe oscillations. We can see a good match between the data and quantum prediction, while the classical prediction fails to reasonably explain the fringe modulations.
Right: Interference dip scan for gramicidin at $T = T_T/2$. The quantum prediction is the better fit for the data, however, the distinction is no longer as significant as for T_T. Note here that the change in fringe modulation is not due to the higher order fringe modulation but due to the changed beam velocity $550m/s \rightarrow 1200m/s$. A version of this figure was published in [2].

4.1 give a beam tilt angle $\gamma = 1.7$ mrad and divergence angle $\alpha = 0.4$ mrad, with visibilities of $V_0 = 0.16$ (T_T) and $0.18(T_T/2)$. While the measurements at $T = T_T$ the classical expectation completely fails to explain the data, for $T_T/2$ the difference is less pronounced. This is expected, as for smaller grating separations the matter waves have less time to evolve and do not reach full fringe contrast. This is in addition to the rise in classical visibility for smaller separations, causing the predictions to converge for small timings.

The simulations were performed using a value of $\beta = 0.6$, based on an average photoionization cross-section of $\langle\sigma_{\mathrm{PI}}\rangle = (4.65 \pm 0.21) \times 10^{-16}$ cm^2 and polarizability volume of $\langle\alpha\rangle = (157 \pm 1) \times 10^{-24}$m^3. To obtain the ionization cross-section, we attenuated the ionization laser energy by controlling the nitrogen gas flow of the laser beam line. The signal measurements were correlated with a simultaneous energy measurement using a $Thorlabs$ pyroelectric sensor and fitted to the equation for the final state population, assuming two populations N_0 and N_I 2.4.

$$N_I(\Phi) = N_0 \left[1 - \exp(-\sigma_{PI}\Phi\tau)\right]. \tag{4.3}$$

We obtain the dynamic polarizability volume from quantum chemical analysis [2], and obtain a value for the ensemble average of $\langle\alpha\rangle$ at 300 K. The precise knowledge of both $\langle\alpha\rangle$ and $\langle\sigma_{\mathrm{PI}}\rangle$

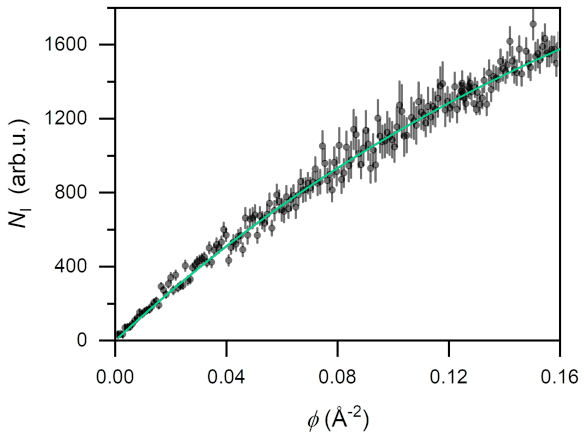

Figure 4.4: Measurement of the ionization cross-section of gramicidin at 157 nm. The scan was taken by controlling the nitrogen gas flow of the detection laser to attenuate the laser energy. Energy and signal measurements were performed simultaneously and fed directly into the control program M.O.P.S. The fit using ref 4.3 agreed very well with the data, suggesting a single photon process. The resulting value for the cross section was $\sigma_{PI} = (4.65 \pm 0.21) \times 10^{-16}$ cm^2. A version of this figure was published in [2].

allows us to distinguish quantum and classical case without prolonged measurement series, as the classical case would require a $\beta \simeq 100$ for the classical fringes to mimic the quantum expectation, which is orders of magnitude higher than for other organic molecules [79]. This method aided in overcoming the signal limitations. Even with the improvement obtained using fs desorption, the signal was not long-lived or strong enough to attempt grating power scans or time scans.

4.4 Beyond gramicidin

4.4.1 Source techniques

The interference experiments with gramicidin showed the possibility of such measurements for fragile and complex biomolecules. However, molecular beam techniques for neutral biomolecules still need to be explored to unlock the realm of proteins for interference experiments. Source stability and brightness will need to be improved significantly before interference experiments with heavier bio-molecules become viable.

4.4.2 The limits of OTIMA

Performing interference experiments with massive, complex molecules face a variety of technical challenges. One limitation is the small scale of the interferometer. With only $\simeq$2 cm distance between the gratings, the mass-velocity product is limited. While the short grating period still allowed for the interference of gramicidin in the first Talbot order, experiments with the protein insulin at $\simeq$5800 Da would not be possible with current source techniques, as the molecules would travel too fast. To reach higher masses, it is necessary to improve the molecular beam sources or to adapt the interferometer. Moreover, proteins are not susceptible to photoionization at 157 nm. While it is possible to ionize even large biomolecules if they are tryptophan-rich biomolecules[101], the natural abundance of tryptophan in proteins is very low. To unlock proteins for interferometry experiments, we must find new ways to prepare photo depletion beam splitters for proteins. All these factors call for a new generation of interferometers to improve upon the OTIMA design and overcome its limitations.

5 Tests for protein charge control

Biomolecules are a large class of materials with high internal complexity. Proteins especially are intriguing, as they are responsible for many biological processes, and they possess complex secondary, tertiary, and even quaternary structures.
The study of proteins is a large and active area of research[102]. In particular, their gas phase properties, decoupled from external influences, have attracted attention[103, 104, 105] to more clearly understand proteins and their behavior inside live organisms. Interference experiments with proteins offer an interesting avenue for probing their internal states. From Chapter 4, we have seen progress towards this goal, but also encountered the limitations of current interferometer and source techniques.

5.1 Photon induced charge change

The challenge of creating a stable source of gas-phase biomolecules is important for mass spectrometry[105], but it becomes even more challenging for neutral proteins, as required for interferometry experiments. Here, we explore photon-induced ionization and neutralization with photolabile tags to enable depletion grating mechanisms.

5.1.1 Direct photon absorption

Photoionization depends on several factors. First and most important, the photon must exceed the ionization threshold of the molecule to maximize ionization. The target can also be ionized if the combined photon energy of the absorbed photons within a small timeframe exceeds the ionization threshold. This multi-photon ionization[106, 70] makes some particles more accessible to ionization as photons of longer wavelengths are more easily produced, however, it may also lead to increased fragmentation of the molecule [73]. Another factor to consider is the absorption site and the size of the molecule[107]. If the free electron is not ejected at the surface of the molecule, electron recapture grows more likely for large systems. A final requirement for obtaining a high ion yield is a high absorption cross-section. It must be high enough that sufficient molecules in the neutral beam interact with the incoming photons to be ionized. Direct photon ionization with high UV/VUV light has been successful in the case of biomolecules up to 2000 Da. Proteins however, starting with the relatively small insulin, have proven to be unresponsive to this approach, with efforts towards post-ionization of a neutral beam showing no successes so far[108, 109]. This behavior is the subject of interest regarding the electron dynamics of complex protein systems [107].

5.1.2 Indirect photoionization with photolabile tags

An effort that combines two disciplines is indirect photon ionization using photoactive or photolabile tags to control and probe the behavior of proteins[110, 111, 45]. Such tags can be fluorescent to allow for super-resolution microscopy [112], or photo-activated medicines. In the gas phase, photo-tags are useful for obtaining mass-sensitive information about biomolecules[110]. Control of a molecule's charge state via the addition of a photo-receptive tag is an extension of these gas-phase approaches. The basic scheme for such a tag is shown in figure 5.1 The protein is outfitted with a tag, promoting absorption of a particular wavelength and ultimately leading to heterolytic cleavage of the tag from the protein. In this process, the two fragments carry different charges from the parent molecule, potentially leading to the ionization or neutralization of a fragment.
The tags shall include an absorption center, a charge center, and a tailored weak point.

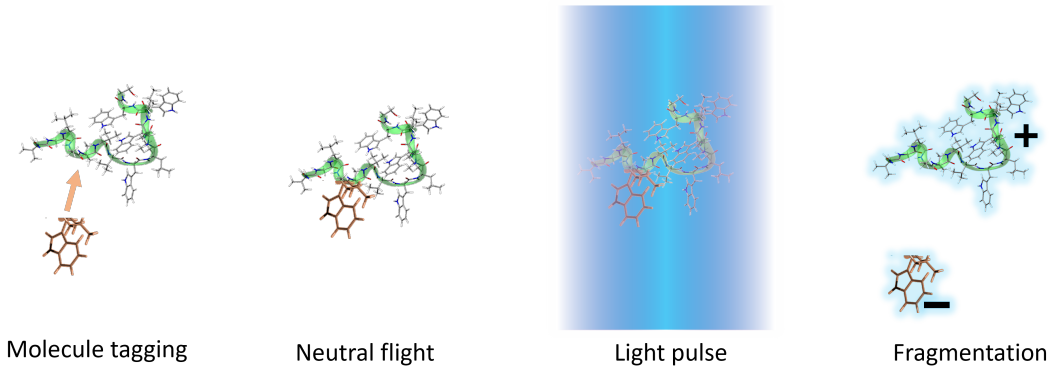

Figure 5.1: Photolabile tag scheme: The molecule is labeled with a photoactive tag. After evaporation, the molecule and tag stay connected until illuminated by a laser pulse of the target wavelength. The bond is cleaved and the tag separates from the molecule, changing the charge state of both in the process.

The absorption center possesses a high absorption cross-section and acts as the target receptor for the photons. The choice of absorption center governs at what wavelength light is absorbed most strongly, giving a choice in the wavelength used. Here it is relevant to find an optimum between absorption cross-section and photon energy, as the latter also influences the response of the tag.
The charge center is the heartpiece of the technique. It is tailored to shift the electron density distribution to create an uneven distribution in the particle charge. This then predisposes the tag to cleave from the protein with a change in charge state, imparting an opposing change in the protein charge state. The choice of charge center influences whether the protein charge state is pushed toward positive or negative change.
The weak point is the site that enables the photocleavage process. Positioned between the protein and the other components of the tag, the strength of the weak point will determine which photon energy is needed to cause the bond to break. As such, it also plays its part in determining the optimal wavelength for the photocleavable tag. A strong bond makes the entire

system more sturdy but requires a higher photon energy to separate. To obtain a photocleavable tag that creates the charge states required for neutralization and post ionization it is necessary to perform a variety of tests.

5.2 Matrix assisted laser desorption of charge controllable molecules

To test the photocleavable tags we must produce an intense beam of ions and neutrals. One method to produce intact protein ions in the gas phase is matrix-assisted laser desorption (MALDi). Here, analyte molecules are mixed into an acidic and UV-absorptive matrix. This mixture is then illuminated by a focused laser pulse to desorb the molecules and create a cloud of ions which can be detected in a mass spectrometer. This way it is possible to obtain even very large intact proteins in the gas phase.

Preparation of the sample

To prepare the sample, it is necessary to apply matrix and analyte onto the target surface using a suitable solvent, with subsequent treatment to remove the solvent and retain a thin film. The matrix is typically a molecule of low molecular weight, able to absorb strongly in the UV at around 350 nm. This makes them the primary target for the laser pulse, protecting the analyte from fragmentation during the desorption process. The acidic matrix molecules also act as proton sources for the ionization process in the expansion plume. Considering these factors, the choice and amount of matrix is of major importance to successfully create ions with MALDi[113]. For our purposes, we have found the optimal matrix to be α-Cyano-4-hydroxycinnamic acid (HCCA), which has strong absorption at 340 nm and does not significantly contaminate the low mass region of the recorded spectra. The solvent also influences the signal yield. The solubility of the matrix and analyte is vital for the mixing of the two components. The vapor pressure is important as it affects the state of the sample after the drying process, which in turn affects the analyte yield. Proper crystallization and thin, homogeneous films are important to achieve a high signal yield[113]. We use dimethyl sulfoxide as the solvent, as it efficiently dissolves our test molecules and has a low vapor pressure. We then prepare the sample using a vacuum drying method [114], which gives a homogeneous coating.

Laser desorption and ionization

During desorption, many processes affect the signal yield. The high intensity of the pulse gives rise to nonlinear processes in the matrix and analyte molecules [82]. This leads to their volatilization, as well as the formation of optical ions due to direct absorption and relaxation. Matrix fragments are another significant product of desorption and can facilitate the protonation of the gas phase analytes. Directly after desorption, the plume constituents are close together, interacting with each other and the light field. Here, secondary ionization processes take place, as the isolated neutrals in the beam can be protonated by free hydrogen ions that remain from the targeted matrix molecules. This process is especially important for large analytes such

as proteins, which are unlikely to ionize with direct photon absorption. The intensity of the desorption influences the signal yield and the constituents of the desorption plume[82, 85].

5.2.1 The experimental setup

In order to test the photo cleavage and ionization potential of several test particles we have built an experimental setup, seen in Figure 5.2 It encompasses particle creation using MALDi, optical access for spectroscopy tests and mass sensitive detection to distinguish between the intact and fragmented molecules in the molecular beam. These requirements are met by the setup, where

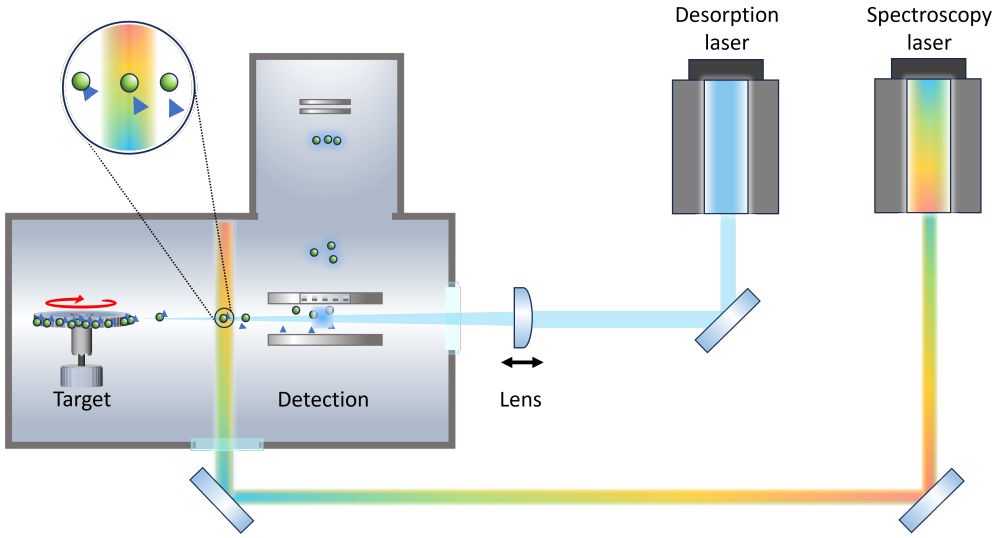

Figure 5.2: Setup for testing photolabile tags. Particles are desorbed from the target surface with a focused laser pulse. A needle electrode close to the target can be used to extract the ions from the beam. During travel, the molecules are exposed to a wavelength-tunable laser. After interacting with the laser, the molecules arrive in the repeller region of a ToF-MS, where the neutral molecules can be post-ionized using a VUV excimer laser. The ions are accelerated into the ToF and hit the MCP stack. The signal is sent to an oscilloscope for evaluation.

a vacuum chamber with optical access allows MALDi mass spectrometry combined with a laser providing ultraviolet to near-infrared light for spectroscopy.

The source

The MALDi source is composed of a target and desorption laser. The target is a motorized aluminum wheel that can rotated to present a fresh sample spot for desorption. This improves the signal lifetime of the experiment and makes it possible to perform spectroscopy experiments on the molecules for extended periods. There are two desorption lasers available to use depending on the needs of the experiment. A nitrogen-laser from *Laser Technik Berlin LTB*, which produces 337 nm light pulses with a flat-top beam profile of 3 mm by 7 mm and a peak pulse

energy of 80 µJ is used to obtain an ion signal for large mass molecules. A $Pharos$ fs-laser system from $Light\ Conversion$ can produce light at 1030/515/343 nm with peak pulse energies of 200, 100, and 70 uJ and a pulse duration of 290 fs. It makes it possible to record cleaner mass spectra for low-mass studies, where matrix fragments give a significant signal contribution. The laser beams are focused onto the wheel using a Plano-convex lens with f =20 cm focal length that is mounted on a translation stage to adjust the illuminated area. This is to ensure the optimal photon fluence for MALDi conditions[85]. Usual intensity values were chosen to be between 1000 and 7000 J/m^2. To enable tests with both the charged and neutral molecules desorbed from the wheel, a needle electrode placed close to the desorption site can be used to deflect the ions from the beam.

Spectroscopy

The spectroscopy laser, an $EXPLA\ NT200$ system, is guided into the experiment orthogonal to the molecular beam path at a distance of 3 cm after the wheel. The laser is tunable in wavelength from 225 to 2700 nm. To make the wavelength region of 240 to 700 nm accessible to the experiment, we use two different sets of mirrors, using $Laseroptic$ UV mirrors covering 240-400 nm, and $Thorlabs$ broadband mirrors for the visible regime. In the UV regime, 266 nm was of particular interest, as this wavelength is a good grating candidate. The low wavelength combined with the availability of good optics and lasers is a powerful combination when considering a future protein interferometer. To perform energy scans for the wavelength range 400-700 nm, the laser is guided through an angle adjustable Fresnel-rhomb for polarization control and a high-power polarizing beam splitter. With this setup, we can attenuate the laser from full energy down to a 1000 times decrease. To attenuate the wavelength region of 240 to 400 nm, we use an angle-dependent ND filter which can reduce the laser energy by a factor of 10000.
The OPO beam has a largely Gaussian shape with a spot diameter of 4 mm. To test for single or multi-photon response, we remember 2.7 and discuss how such processes behave. We start with a molecule, exposed to a laser pulse with intensity I_0 and photon energy $\hbar\omega$. Using 2.4 and2.6 as guides, we can construct fits to the data. For photodissociation, we need to account for two separate populations: the detected molecules N_0, and the molecules interacting with the light pulse $N_L \leq N_0$. The expected number of detected particles then follows

$$N(\Phi) \ = \ N_0[1 - N_L(1 - \exp(-\sigma\Phi\tau))]. \tag{5.1}$$

When we look at the fraction of detected molecules N_L/N_0 we can introduce the parameter $alpha = N_L/N_0$, quantifying the overlap between depleted molecules and detected molecules.

$$N(\Phi)/N_0 \ = \ 1 - \alpha + \alpha[1 - \exp(-\sigma_{(n)}\Phi^n\tau)] \tag{5.2}$$

Detection

To detect the molecules we use a ToF-MS from $Kaesdorf\ Munich$ which can detect positive ions with a mass resolution of $\Delta m/m \ = \ 1/500$. With this, we can distinguish the main protein signal from the cleaved tags. To address the neutral molecules in the beam, a $Coherent$

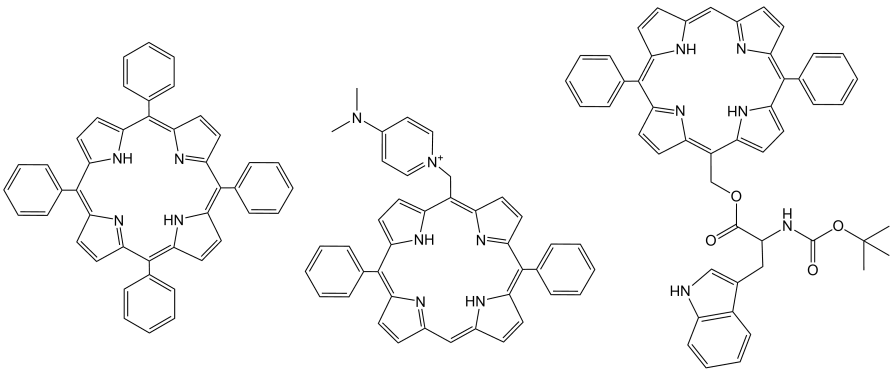

Figure 5.3: Chemical structure drawings of the three tested porphyrin derivatives. Left: Tetraphenylporphyrin(TPP) without any photolabile tags. Middle: Diphenylporphyrin(DPP) tagged with 4-Dimethylaminopyridine, with a charge center to facilitate heterolytic cleavage. Right: DPP tagged with tryptophan, for single photon cleavage of the bond

F_2 excimer laser is aligned to hit the molecules in the repeller region of the ToF-MS to photo ionize the neutral molecules desorbed in the MALDi process. To study the ions, we leave the needle electrode and the excimer laser deactivated, and activate both to study only the neutrals. To read out the Tof-MS signal, we use a $Waverunner$ Oscilloscope with 1 GaS/s, set to record an average of 256 experimental frames.

Timing

The experiment is timed with two pulse generators ($BerkelyNucleonics$ 475). To operate the experiment with (mode 'ON') and without photocleavage (mode 'OFF'), we use a TTL switch to channel the ToF signal from the two modes. This allows us to simultaneously record the spectra for molecules that interacted with the spectroscopy laser and a reference spectrum without the laser, reducing systematic errors due to signal fluctuation.

5.2.2 Test molecules

Porphyrins make interesting test candidates due to their high absorption cross-section around 410 nm. This may make them useful as the absorptive component for the photolabile tag. Here we have tested three varieties of porphyrin, shown in figure 5.3. The first is tetraphenylporphyrin (TPP, 614 Da), a chromophore with an absorption maximum expected at 420 nm. TPP is abundantly available, desorbs well, and can be photoionized with a single photon of 157 nm and 2 photons of 266 nm. This makes it a good overall candidate for testing and calibrating the setup. The next porphyrin derivative is diphenylporphyrin tagged with 4-Dimethylaminopyridine (DPP-DMAP, 597 Da), with an absorption maximum at 410 nm. This substance was tailored to cleave heterolytically after absorption of a photon. The final test particle, diphenylporphyrin tagged with tryptophan (DPP-TRP, 778 Da), is similarly tailored for photocleavage and change in charge state.

5.3 Results

5.3.1 Tetraphenylporphyrin

Due to the abundance and sturdiness of TPP, we were able to dry coat the target with the substrate, creating a thin film of TPP without matrix. We performed tests with ns and fs pulses to test optimal desorption conditions and particle velocities. From initial tests with fs-desorption, we obtained optimal signal intensity for photo-ionized neutrals with 4 µJ pulse energy and the lens positioned 17.86 cm from the target. A velocity scan with these settings returned a mean velocity of ≃500 m/s. Optimal parameters for ion generation were a pulse energy of 20 µJ with an 18.16 cm distance between the lens and target. Here, the velocities were much higher, giving a mean velocity of ≃1200 m/s. Sample mass spectra and velocity scans are shown in figure 5.4 Using the source parameters for neutral desorption, we performed energy scans at 420 nm to

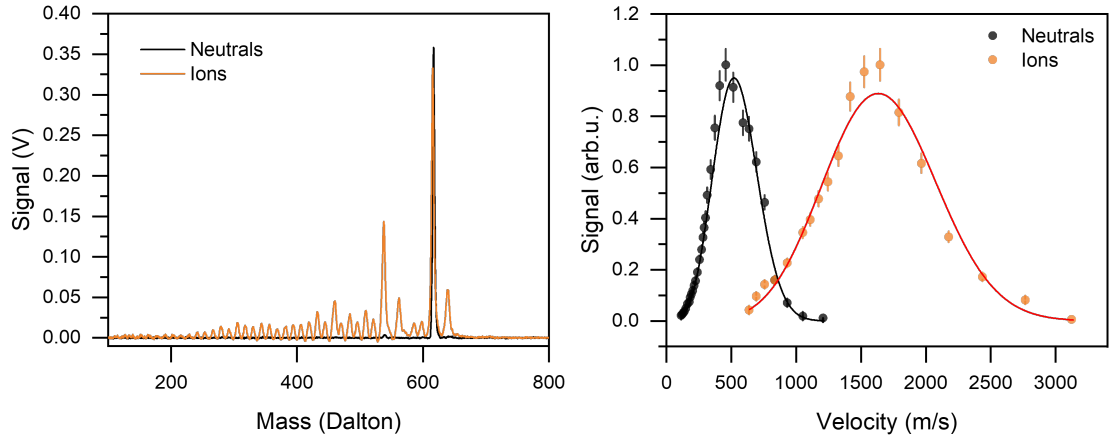

Figure 5.4: Left: Mass spectrum of neutral, post-ionized (black), and MALDi ion signal (orange). We see a stronger fragment background for MALDi ions due to the higher intensities at the desorption site. Right: Velocity of TPP, examining neutrals (black) and ions (orange). The ion velocities are significantly higher than observed for the neutral beam. A fit to the data (red lines) using 3.1 returns a stream velocity of around 300 m/s for the neutrals and 1200 m/s for the ions.

observe the signal dependence on the laser pulse energy. The data, shown in figure 5.5, shows full depletion of the main peak at higher pulse energies. Applying a fit to the data using 5.2, we obtain a single photon cross-section of $\sigma_{(1)} = (2.26 \pm 0.31) \times 10^{-16}$ cm^2. This value misses the expected absorption cross-section from solution studies ($\sigma_{sol} \simeq 4 \times 10^{-15}$ cm^2) by an order of magnitude. This may be due to the likelihood of fragmentation being low after photon absorption. While reduced compared to studies in solution, the high absorption cross-section may make TPP a valid candidate for the antenna role of a photolabile tag.

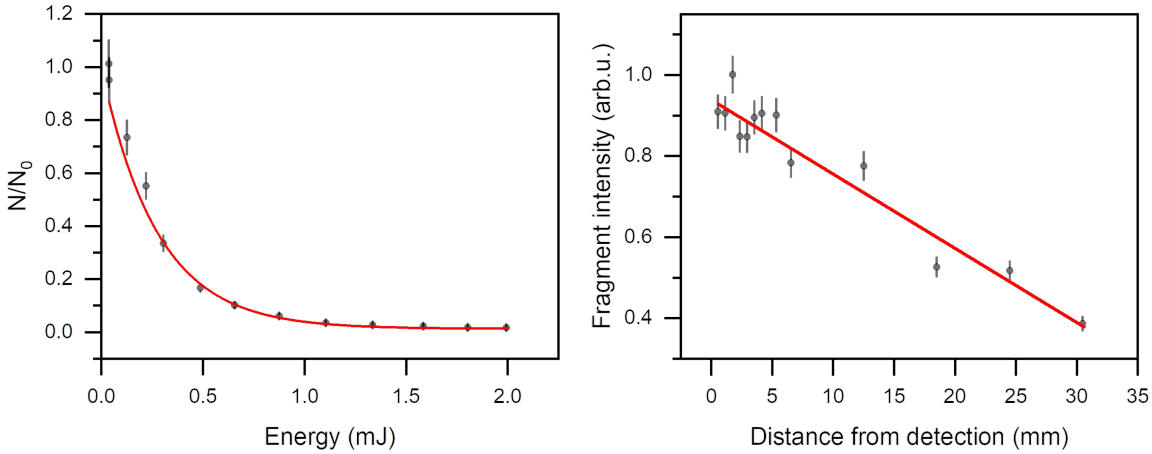

Figure 5.5: Left: Depletion measurements for TPP at 420 nm, with single photon depletion fit. The individual data points were taken with 128 averages for depletion measurement and simultaneous reference. The extracted cross-section are $\sigma_1 = 2.26 \times 10^{-16} cm^2$ for single photon depletion. Right: Relative fragment population for varying distances between detection and depletion laser. The red line is a guide for the eye. We see that with increasing distance, fewer fragments arrive inside the detection region. This suggests a significant momentum kick for the fragments. Data was acquired with 1000 averages per measurement.

Fragment trajectories

Looking at the difficulty of ionizing proteins, light grating based on photo fragmentation may be an interesting avenue to pursue. To verify the potential of fragmentation beam depletion, it was of interest to observe the fragment population with varying distances from the source. This can give information regarding the fragment trajectories after the event, which may be divergent enough to lead to total ejection from the molecular beam[75]. Should this be the case, it would present a viable grating mechanism in the future. To this end, measurements of the fragment populations of TPP were performed to obtain the exit angle from the detection region. The results are shown in figure 5.5 We see that the number of detected fragments decreases as the depletion laser is moved further away from detection. A linear fit to the data suggests a falloff to no fragment signal at a 52 mm distance from the detection region. As the detection area was a horizontal running wave with 4 mm width, as opposed to the molecular beam width of 1 mm, the exit angle then is on the order of $\simeq 2$ mrad. Given that the usual beam collimation requirements are stricter than this number[2], we can assume fragmentation will lead to beam depletion in usual interferometer experiments.

Ionization with 266 nm

In addition to depletion spectroscopy at 420 nm, we tested the photoionization yield at 266 nm, a candidate wavelength for the planned protein interferometer. As TPP does not display a

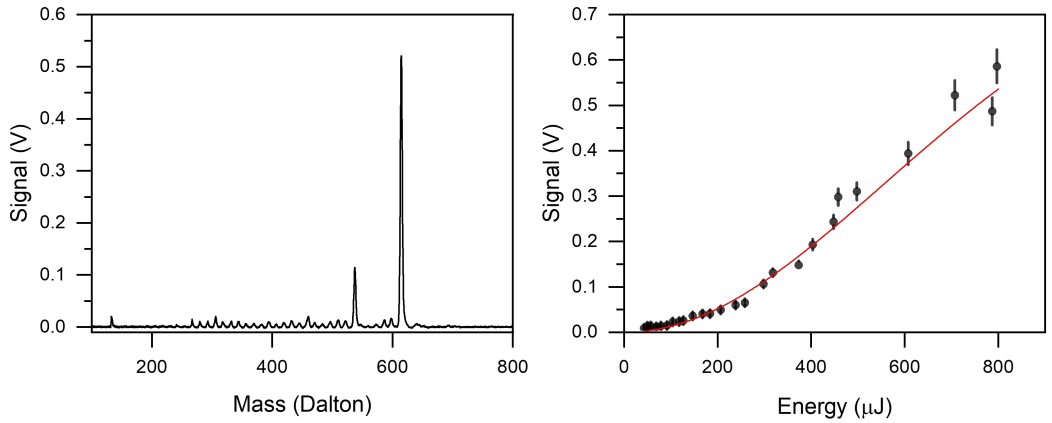

Figure 5.6: Left: Sample mass spectrum for TPP ionized with 266 nm. We see a visible fragment background, likely stemming from the source. Right: Energy scan of the TPP photo ion yield at 266 nm. The departure from linear behavior at low pulse energies suggests a two-photon process. The red line is a fit to the data assuming two-photon ionization.

resonance at 266 nm [115], we apply a non-resonant two-photon fit 2.7 to the data and obtain a cross-section of $(7.3 \pm 3.0) \times 10^{-41}$ cm^{4}s. While compared to a single photon process, two-photon processes are less favorable for depletion gratings, as the effective opening fraction of the grating is increased for a given pulse energy[74], it is still possible to observe interference fringes given suitably high pulse energies in the gratings. Lasers with pulse intensities of 10 mJ/cm^2 at 266 nm are commercially available and can be focused to reach higher intensities if necessary. Given this, TPP presents a potential candidate for interferometer alignment.

DPP-DMAP

For DPP-DMAP sample, we prepared a solution with 1:100 analyte-to-matrix ratio, applying 40 µL of the mixture onto the wheel and vacuum drying the sample. The neutral signal with fs desorption at 4 µJ pulse energy and 17.86 cm showed a complete lack of the intact mass peak at 597 Da. Using the OPO at 410 nm to ionize the particles was successful, as can be seen in figure 5.7 In the energy scan, we observe the ionization of both the parent mass and the fragment DPP+carbon. The process does not match a one- or two-photon absorption curve, but rather a three-photon process. This fits with the ionization threshold energy of porphyrins, which exceeds 6 eV [116, 117].

5.3.2 DPP-TRP

The DPP-TRP sample was prepared with similar initial conditions to DPP-DMAP, with a 1:100 analyte:matrix ratio by number and vacuum drying after application on the wheel. We observed a strong signal of the intact mass peak with VUV ionization, allowing us to perform tests of both photo depletion of the main peak and photoionization at 410 nm. Here we see clear

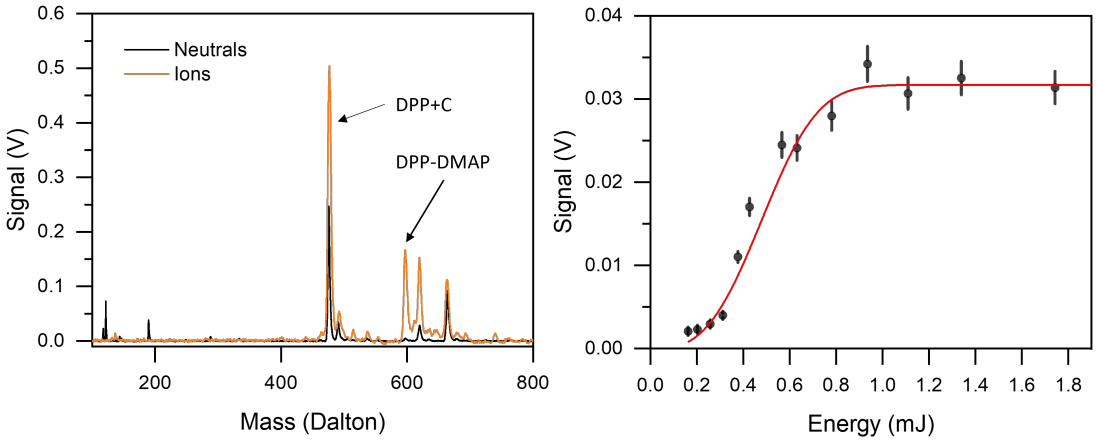

Figure 5.7: Left: Mass spectra for post-ionization (black) and MALDi ions (orange). The post-ionized spectrum has a strong mass peak for DPP+C but lacks the intact parent mass. In the MALDi configuration, we see the parent mass peak emerge. Right: DPP+C post-ionization signal for different pulse energies

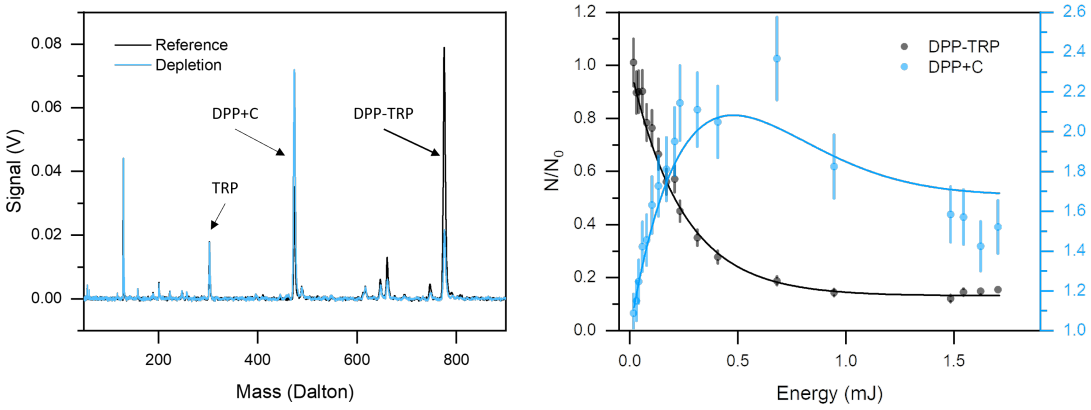

Figure 5.8: Left: Mass spectrum of DPP-TRP with (blue line) and without (black line) 410 nm light present. The three marked peaks from right to left correspond to the parent mass, DPP+C, and the TRP residue respectively. Right: Energy scan for the parent mass (black) and DPP+C (blue). The lines are fit using the assumed populations, with pure depletion for the parent peak. For DPP+C the contributions are an increase from the parent population and a reduction due to depletion of the initial fragment population.

evidence of a single photon process for the depletion of the main peak with a cross-section $\sigma_{PD} = (2.52 \pm 0.12) \times 10^{-16}$ cm^2. Observing the energy dependence of the main fragment

DPP+C we see more complex behavior. The signal first increases in strength and then weakens at higher pulse energies. The increase in signal corresponds to the fragmenting parent mass exactly, while the later drop in signal may be due to photo-depletion of the initial DPP+C population in the molecular beam. The TRP signal remained stable for the energy scan, showing no dependence on the rising laser fluence.

With the initial tests with photocleavable compounds, we can see a potential path towards new grating mechanisms for proteins. Photo-fragmentation gratings have already shown potential in previous experiments [75], but it remains to be seen if an efficient single-photon channel can be engineered to be used as PCT for proteins. Photo-activated charge control remains the key piece required for interference experiments with proteins, as such a mechanism in the form of a tag would ensure broad accessibility for neutral protein studies in the gas phase. Here, results have been promising, showing efficient single-photon cleavage for two compounds that may be used to facilitate heterolytic cleavage in the future. While this is ultimately the goal for proteins, photo-fragmentation is a sufficient grating mechanism for future interference experiments.

6 Controlled creation of nanoparticles

Optical trapping experiments are a powerful tool for probing quantum mechanical systems [118, 119]. Larger dielectric systems can be trapped using a tightly focused laser [120], where the incoming light polarizes the material and induces a gradient force to keep the particle contained. With precise control of the light field, this can also be used to cool the particles to the motional ground state[121, 122]. To perform such intricate experiments, the first step is the launch and individualization of size-selected nanoparticles that can be trapped. Finding new, improved sources is highly relevant, as they may unlock the limits that are placed on the experiments by the source quality. In this chapter, I will give a brief overview of the current state-of-the-art before presenting the work done on a particular method for particle preparation, namely particle creation with ultrashort weak laser pulses.

6.1 State of the art

The variety of loading mechanisms currently in use indicates the need for a reliable high vacuum trap loading mechanism. All of them have advantages and limitations that need to be accounted for when building an experiment.

Trap loading via nebulization

The first method to mention is based on droplet ejection with ultrasonic nebulization[46]. Here the nanoparticles of interest are put into a solution of high vapor pressure solvent which is sprayed into the trapping region. With this method, numerous nanoparticles are ejected into the air, where they may be picked up by the trapping apparatus. The abundance of particles is of great importance since the actual trapping area of typical optomechanical experiments is small, making trap loading with small numbers of randomly moving particles difficult. The method is also simple to implement. To be able to load the trap, one needs to have an entrance valve from which to inject the mixture into the system and wait for a nanoparticle to be captured. There are several drawbacks to this technique, however. The injection of liquid droplets into a vacuum system creates a significant gas load, preventing vacuum application. Furthermore, the undirected nature of the method, combined with the large number of nanoparticles transmitted, may lead to the coating of sensitive surfaces and make the actual experiment more challenging to perform. The likelihood of trapping liquid droplets without a nanoparticle inside is another drawback. Only after evacuation of the chamber can one be certain that the trapped particle is a nanoparticle and not a liquid droplet. Finally, this method requires the system to be at millibar pressures and to use the background gas as a slowing mechanism for the fast nanoparticles in the expansion plume. It requires extended pumping to reach the pressures necessary for further experiments.

Laser induced acoustic desorption

The second mechanism, laser-induced acoustic desorption[47], relies on the creation of a shockwave to launch particles from their parent substrate into the trap. The process can be imagined like this: nanoparticles are deposited on a flat, thin target surface. To launch the particles, the backside of the target is illuminated with a short pulse laser, leading to ablation and the creation of a pressure wave traveling through the substrate towards the nanoparticles. Once the wave reaches the other side, the particles are launched from the surface. The key advantage of LIAD is that it is vacuum-compatible. The mean particle velocities are on the order of 1-10 m/s. This is important for experiments with smaller trapping strengths, as the low velocities enable trapping at such conditions [123]. However, while LIAD may be considered a high vacuum-compatible source mechanism, the target substrate has to be replaced, making it necessary to open and reseal the vacuum chamber regularly. This reduces the reproducibility between targets, as even small differences may have large effects on the velocity and spread of the particle plume. The dynamics of shockwave propagation and particle launch depend strongly on the surface condition and density of the coating, and minor variations between targets may lead to a significant difference in the number of trapped particles per launch event.

Piezo-electric launcher

The piezo launching method[124] can be seen as an analog to the LIAD launch mechanism. Here, the laser-induced shockwave is replaced with a fast high-voltage signal on a piezoelectric crystal. This creates the accelerations needed to launch particles from a coated glass slide attached to the piezo into the vacuum. Just like LIAD, this system is vacuum-compatible and produces a large number of particles. Its main advantage over LIAD is its reliability, as the relatively simple process of launching the particles of the piezo is controllable to a good degree. While the particle size that can be launched is limited due to Van der Waals interactions, treatment of the glass surface makes it possible to reach nanoparticle sizes of <100 nm diameter[125]. The piezo launch method also requires the nanoparticles to be refreshed after use, leading to interruptions in the experiment.

Hollow-core fiber guided loading

The main characteristic of the previous launch mechanisms has been the number of particles ejected. The mode of operation was to launch an abundance of nanoparticles to improve the odds that one may be trapped by the experiment. This approach is sound in principle and has allowed numerous powerful experiments [121, 126, 127], but puts limits on the actual experiment. Hollow core fiber loading of the particle [128] goes to the other extreme. Here, a single particle is transferred from a high-pressure region into a high vacuum region. This transfer is made possible by pumping a hollow core fiber with light fields in both directions, which creates a standing light field inside the fiber. By tuning the pumping lasers, the particle can be transferred through the fiber while resting inside a standing wave minimum. The particle can then be moved into the trapping setup with velocities on the order. Using the hollow core fiber, it is possible to transfer particles from ≈ 10 mbar into ultra-high vacuum. A disadvantage

of this system is its complexity and fragility. To properly control the particle, one needs to know the size and optical properties, as this changes the light field intensities required to smoothly guide the particle. The technique requires optical access on both ends of the fiber, potentially taking space from the trapping experiment. Finally, the hollow core fiber is prone to damage in the form of clogging and breaking during operation.

6.2 Laser induced transfer

This method is a middle ground between the multi-particle launch systems and the single-particle control of the hollow core fiber. The core concept of the technique is the use of ultra-short laser pulses with energies of a few nJ to melt out pristine nanodroplets from a substrate of choice[49, 50]. This technique, known as laser-induced transfer has found strong interest in the field of micro- and nanomachining[129, 130, 131], allowing for precise placement of size-controlled nanostructures with flexibility in the choice of material. In laser-induced-$backward$-transfer (LIBT) the front target is illuminated, leading to the particle traveling back towards the lens. For laser-induced-$forward$-transfer (LIFT), the backside of the target is illuminated through the transparent supporting substrate and the particle travels away from the pulse.

6.2.1 The meltout process

Many studies, working with materials ranging from metals to semiconductors, have tested the mechanisms of laser meltout[129]. In simple terms, the process can be described as follows: controlled laser irradiation of a thin pure substrate causes the formation of a molten area, which after forming and detaching will take on a spherical shape due to surface tension. With precise control of laser pulse energy and focal spot size, the process can reliably create particles of the same diameter. A sketch of this process is shown in figure 6.1. For a more in-depth look we must distinguish the cases of metals versus semiconductors, as the relevant processes vary between the two types of material.

Metals (Gold)

In the case of metals, the illumination of the target has several possible outcomes, depending on whether the energy threshold is missed, met, or exceeded. The irradiated area begins to melt and deform due to a density differential. Examples for gold [132] show that the heating causes a bubble to form under the target area, with the center of the molten substrate expanding to a spire shape. With higher energy, a droplet starts to form on top of the spire. Reaching the threshold energy, this droplet can detach from its support and lift directly away from the surface. It is this main particle that has a controllable size. In addition to the primary particle formation, additional particles may form from the tension of the liquid spire. This secondary particle event may produce several particles of varying sizes[132].

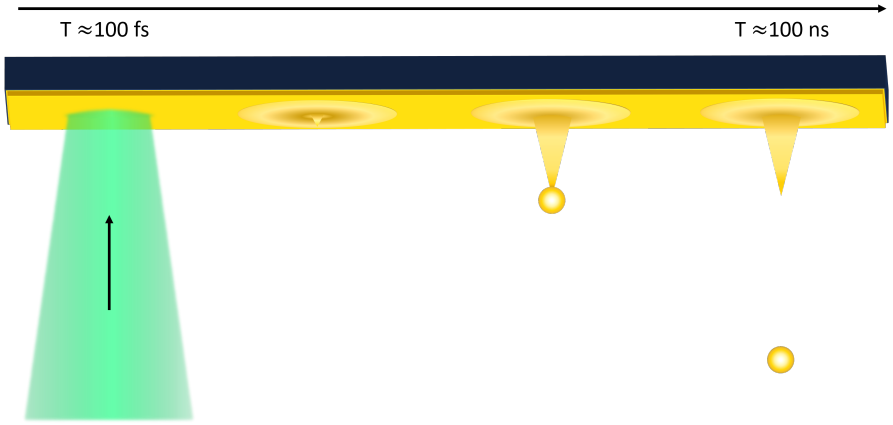

Figure 6.1: Sketch of the principle behind the single particle meltout process. A target surface is illuminated with a short-pulse laser. The absorbed light leads to localized melting of the surface, which deforms. Parts of the surface accumulate into a sphere due to surface tension. The sphere detaches from the rest of the substrate.

Semiconductors (Silicon)

The process in semiconductors is largely identical at first glance: with sufficient energy a single nanosphere is created and ejected from the target site. However, a closer study of the meltout process reveals important differences. Silicon has advantageous optical properties for optomechanical experiments because of its very low absorption and high polarizability at 1550 nm wavelength, the standard for such experiments. Silicon is an anomalous liquid with a liquid phase that is denser than its solid crystalline phase. The higher density prevents the formation of spires as launch sites for nanoparticles. For bulk silicon, the liquid will instead move towards the outer part of the melting site, following the temperature gradient. Droplets form at the edges of the irradiated area and with sufficient energy input detach as a set of undirected particles of varying sizes[133].
To promote single particle creation, it is advantageous to move to a silicon on insulator (SOI) substrate[50], where a layer of crystalline silicon around 50 nm thick is coated onto a high melting point substrate. This changes the melting dynamics dramatically. Instead of forming molten edges, the silicon accumulates into a hemisphere at the interface of the target and support substrate. With sufficient energy, this structure turns into a sphere due to surface tension and can lift off. This method creates a different melting pattern to metal nanoparticle meltout. For increasing energy, a lump forms, becoming more pronounced, and finally, if the energy threshold is met, an indentation where the proto-particle used to reside. Using a thin layer of silicon and properly adjusting the pulse energy and focus can thereby create size-controllable single particles in a fashion similar to metal particle creation.

6.3 Experimental setup

To test this method for nanoparticle creation and loading, we need to implement the technique, evaluate the vacuum compatibility, and finally test the kinetic parameters of the created particles. These necessary steps inform the design of the experimental setup, seen in figure 6.2. The

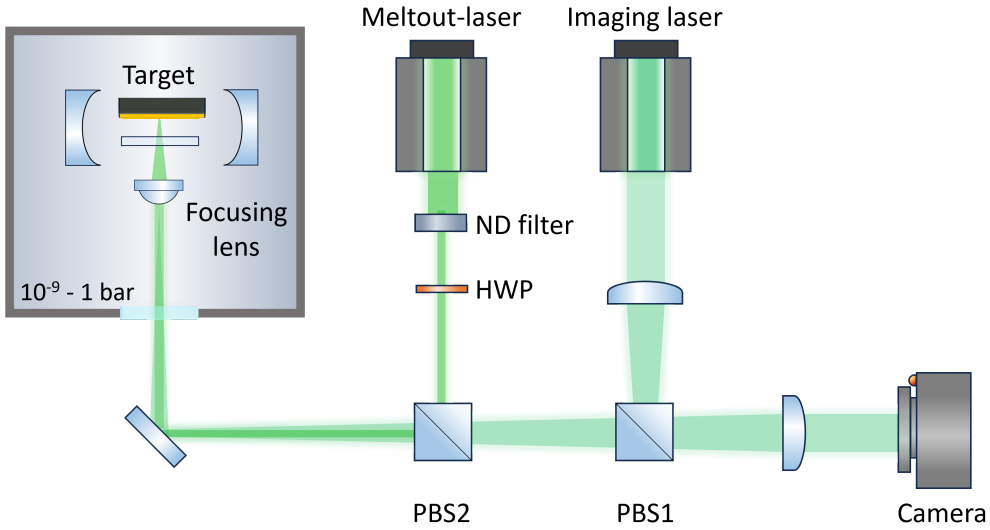

Figure 6.2: Simplified image of the experimental setup used for nanoparticle printing. The meltout laser is attenuated from its initial energy to the required energy range for meltout. Before entering the vacuum chamber, it is combined with the imaging laser via a Brewster window. A high NA aspheric lens focuses the beam onto the meltout target. To optimize focal distance and to move target sites, a motorized stage is employed. To ensure optimal positioning, the target site is viewed using a CCD camera.

experiment was set to allow operation both in LIBT and LIFT modes, allowing us to test various substrates as nanoparticle generation platforms. The setup may be divided into two segments: particle generation and particle detection.

6.3.1 Particle creation

The size-selective meltout process requires fine control of the laser energy and the spot size on the target substrate. To control the pulse energy the meltout laser, a pulsed *Light Conversion pharos* laser with 515 nm wavelength, 260 fs pulse duration, and 110 µJ peak pulse energy, the beam was guided through an attenuation stage to reduce the energy to the required range of 2-50 nJ. After the attenuation stage, the light pulse is guided into the experimental vacuum chamber through an AR-coated window. Here, it is focused to a sub-micron waist onto the target using an aspheric lens (NA = 0.55, EFL = 4.6 mm). The target may be moved using a *SmarAct* high precision 3d-translation stage.

To observe the target area and obtain feedback on the focal spot size, a second laser system is aligned to be co-linear with the meltout laser and acts as an imaging system. The continuous imaging laser (520 nm, <1 mW) is focused on the back focal plane of the aspheric lens, providing a collimated picture of the target area after exiting through the lens again and traveling through a lens towards a high-resolution camera ($Xereon$). We first align the imaging laser to good image quality, then align the meltout laser by observing the scattered light captured with the camera, using this to optimize position and angle. The distance of optimal focus is determined similarly. The target mount is machined to fit both the target sample and a capture slide, with a 15 µm distance between the target and capture. We observe particle sizes, positioning, and meltout behavior by viewing the samples under a $Zeiss\ Supra\ 55\ VP$ electron microscope. To ensure conductivity, the capture slide is coated with a gold film of about 10 nm thickness beforehand.
We used silicon-on-insulator (SoI) wavers, consisting of a 50-nanometer thick layer of polished crystalline silicon on a SiO_2 insulator substrate, supported by crystalline silicon with 300 µm thickness. We chose this type of substrate both for its availability and the ease of comparison between our and previous results. A comprehensive list of all target substrates used is given in table 6.1

Substrate	SOI	annealed silicon	gold
thickness, nm	50, 40, 25, 16	40, 20	150, 100

Table 6.1: Sample substrates used for tests of single particle creation with fs-laser pulses. The SOI samples were used for testing the method, its vacuum compatibility, and scattering detection measurements. Annealed silicon was used to test LIFT viability for non-crystalline silicon. The gold substrates were used to obtain velocity information for an alternate material type.

6.3.2 Cavity and scattering detection

To obtain in-flight information about the particles, we add a scattering detection setup to the experiment, using an infrared high-finesse ($F = 2 \times 10^4$) cavity and a scattering detection fiber(figure 6.3 The cavity is pumped by a fiber-coupled laser system ($Toptica\ CTL$, 1550 nm, $\Delta\nu = 10kHz$. The cavity-mirrors have a radius of curvature R = 10 cm and are spaced L_{cav} = 2.13 cm apart, giving a cavity waist of 120 µm, a free spectral range $\nu_{FSR} = 7.04$ Ghz and a line width $\Delta\nu_C = 352$ kHz. To stabilize the cavity we use side-of-fringe locking set to a detuning $\delta = \Delta\nu/2$

The cavity is moved independently of the target site with a 3D motorized $picomotors$ translation stage. The separate movement to the fixed meltout target point allows us to optimize the overlap between cavity mode and particle trajectory. The scattered light from the particle traversing the cavity is captured by a fiber which is placed on a third translation stage to allow alignment independent of both the cavity block and particle creation setup. As the particle travels through the cavity, it scatters light to the sides. To collect the light, we use a multimode

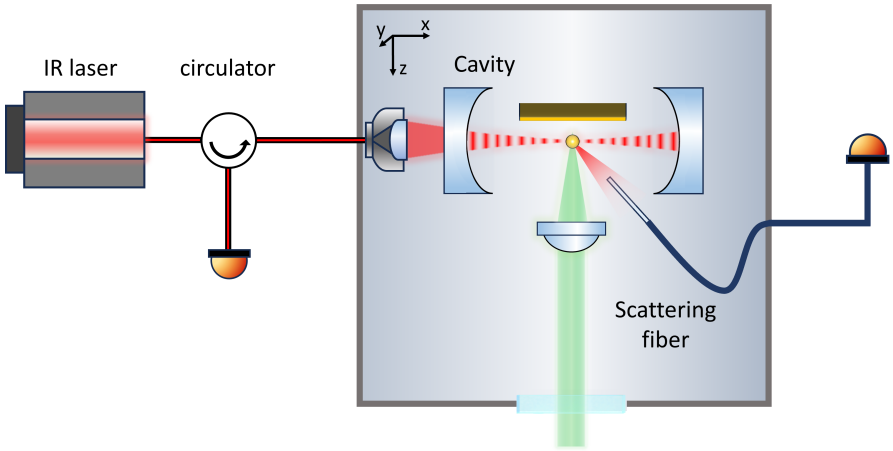

Figure 6.3: Cavity detection scheme of the meltout setup. The cavity is locked using side of fringe locking and aligned with the fs laser beam using a motorized stage. An additional optical fiber is aligned with the setup to pick up the scattered light of the particle as it passes through the light field. The scattering response can be observed using a biased photodiode detector. The time trace is recorded to obtain information about particle velocities and exit angles.

scattering fiber with a 600 µm mode diameter that is placed at 500 µm distance to the cavity waist. The relative scattering strength of a particle with radius r is

$$\eta_{rs} = \frac{P_s}{P_c} = \frac{\lambda}{3hc}\left(\frac{k^2\alpha}{\pi w_c \varepsilon_0}\right)^2. \tag{6.1}$$

Here, $\alpha = 4\pi\varepsilon_0 r^3 Re[(\varepsilon-1)(\varepsilon+2)]$ is the real part of the optical polarizability, ε_0 the electric permittivity of vacuum and ε the complex dielectric function of the material. The scattering signal is recorded using a $Waverunner$ oscilloscope with 5 GSa/s. The time a particle takes to travel through the cavity mode gives us information about their velocity, while the number of traversed antinodes relates tho the transverse velocity. We extract the velocity parameters with a fit incorporating the cavity waist w_V and wavelength λ_C

$$S(t) = A_0 \exp\left(-2\left[v_z\frac{t-t_0}{w_C}\right]^2\right) \times \left[1 + A_1\cos^2\left(\frac{\pi v_x}{\lambda_C}t + \phi_0\right)\right] \tag{6.2}$$

6.4 Results

6.4.1 Particle creation for vacuum application

Size controlled particle creation

The first tests of the experiment aimed to verify the controlled creation of single particles using SOI with 50 nm thickness. The meltout spots, shown in figure 6.4 show all the expected

characteristics for the different energy levels. Below the threshold energy E_P, the proto-particle remains attached to the surface as a hemisphere surrounded by an indentation. Reaching the threshold, the target site shows the exit mark left by the particle, a deeper indentation in the center of the structure, with a corresponding single particle on the surface. Finally, target sites illuminated with energy exceeding the range for single particle creation displayed visible molten edges, a of secondary particle creation. Single particles could be reliably created with energies

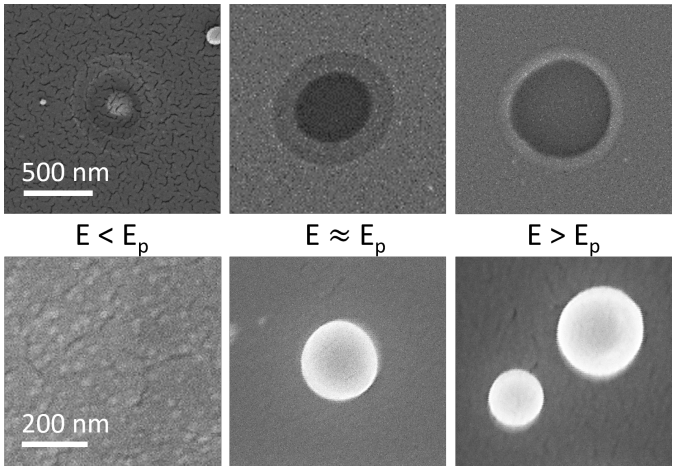

Figure 6.4: SEM images of silicon meltout at varied energies. Top: SOI substrate after illumination at several pulse energies. Bottom: capture slide images corresponding to the meltout events. The paired images show the molten spot of the target and the corresponding particle. Below threshold energy, the target forms an incomplete nanoparticle. For pulses within the energy range

ranging from 4.6 to 8.8 nJ. The single particle printing worked with a probability p>0.8, with good control of particle size characteristics.

Testing vacuum compatibility

Building on the successful single particle creation, we moved on to testing the vacuum compatibility of the method. Three different pressures were chosen to perform the tests. With atmospheric pressure as a reference, we performed the experiment at pressures of 10^{-2} mbar. To ensure ease of comparability, all samples were created with a single target and capture slide. This allowed direct verification of the process by comparing the melting patterns of the target plate and the arrangement of deposited nanoparticles on the capture slide. SEM images of all scenarios are collected together in FIGURE 6.5. We see that different pressures show no visible influence on the process in either reliability or size control. The radiative cooling rate

6.4.2 Cavity scattering detection

As the final step in the main line of silicon experiments, we measured the particle velocities and angular spread. Here, we observed a spread in the cavity fly through times and number of

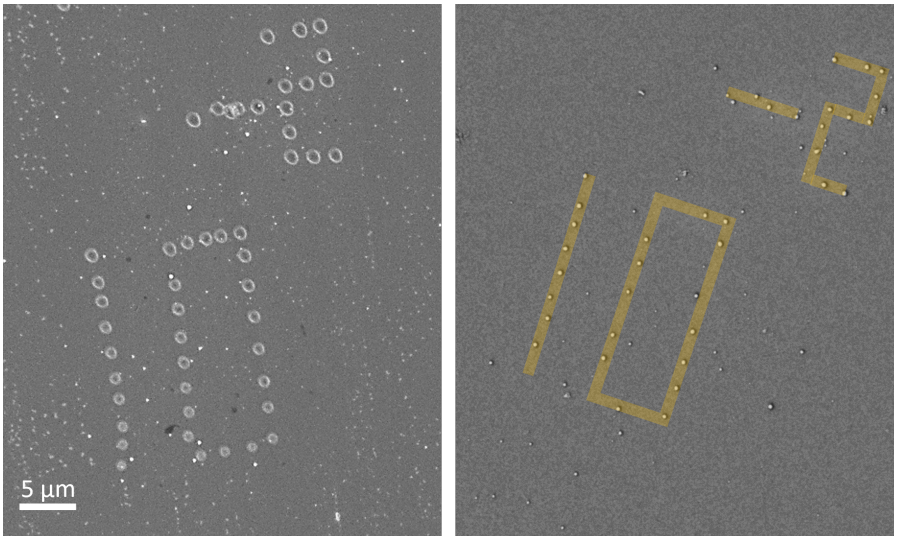

Figure 6.5: Left: SOI target site at 10^{-2} mbar pressure. The meltout spots are qualitatively the same as for atmospheric pressure. Right: capture slide image of the target site. We see a high ratio of single nanoparticles, deposited with good precision. The image was mirrored for ease of reading, with a highlight over the particles.

traversed antinodes. During several measurements, two distinct particle events were observable, indicating a possibly too high pulse energy. A time traces showing a particle transit event is shown in figure 6.6 From the extracted parameters we can see a mean velocity $\langle v_t \rangle$ =(32±

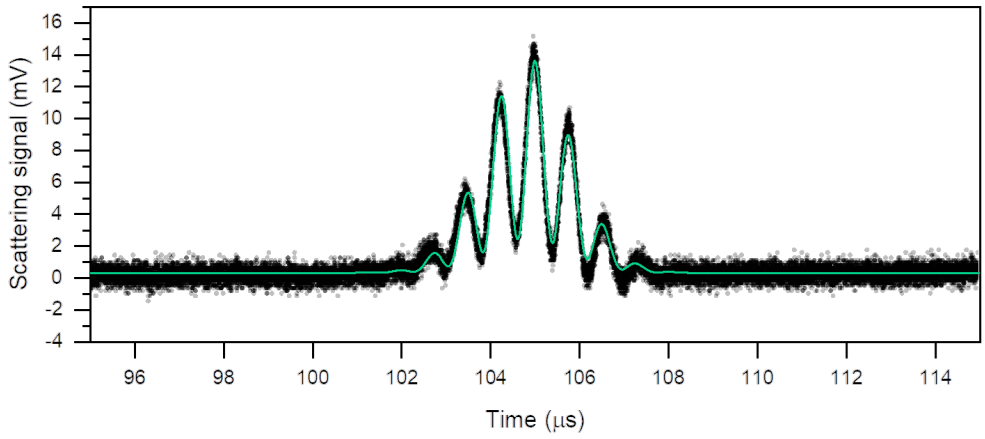

Figure 6.6: Sample traces of the scattering signal from created silicon nanoparticles. The scattering trace of the particle is fitted with a sinusoidal modulation describing the path through the grating antinodes, with a Gaussian envelope to characterize the travel through the cavity. The fit parameters from 6.2 give a measure of the particle velocity and the exit angle from the surface.

10)m/s, with a small angle spread of $\simeq$ 1 mrad. This agrees well with previous findings that studied the reliability of particle placement over distances between 10 and 80 microns[134].

6.4.3 Testing different targets

To extend the flexibility of the method, we performed tests on a variety of substrates using different focal distances.

Annealed silicon on glass

Laser-induced forward transfer has many advantages over backward transfer when one considers experimental space constraints. Motivated by this, we tested targets of annealed amorphous silicon with thicknesses of 40 and 20 nm, supported by a 170 μm thick glass substrate. The LIFT targets showed a similar response to the SOI wafers to laser illumination in the camera readout. However, studying the samples in electron microscopy revealed a strong qualitative difference between the samples, seen in figure 6.7. For LIFT, both 40 and 20 nm samples showed

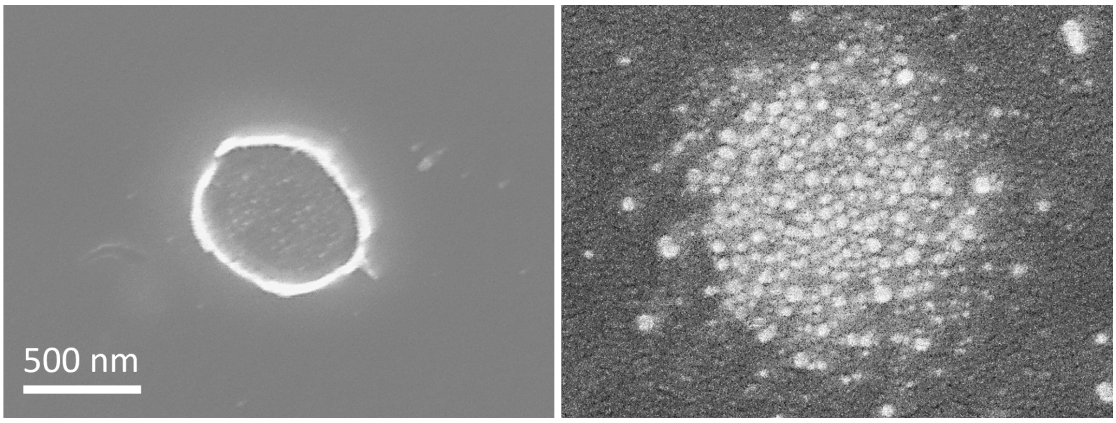

Figure 6.7: Left: SEM image of the annealed silicon targets after illumination. We see molten edges and droplet formation at the edges, with a jagged area in the center. Right: SEM image of the ejected particles on the capture slide. The pattern forms a disk of many small nanoparticles with different sizes

meltout behavior similar to bulk silicon[133]: a hole lined with molten droplets at the edge. Repeating the tests with LIBT yielded the same results. Amorphous silicon has an electron mobility of $\approx$0.1 V/cm^2 [135, 115], as opposed to crystalline silicons 1000 V/cm^2 [136], The heat conductivity is much lower as well[137]: 1.8 W/mK for amorphous silicon, compared to 100 W/mK. These differences may explain the change in behavior. Since the light is absorbed within a few hundred femtoseconds, the electron response contributes to a majority of the heating. Lower electron mobility means more localized heating, which compounds with the lower heat conductivity. Capture slide images of the meltout tests show deposited discs consisting of many particles with diameters <30 nm. The size of the disc is scalable with laser energy, up to the point where ablation becomes predominant.

Etched silicon

Achieving stable creation of particles with sizes smaller than 100 nm is an important milestone for loading small, ultra-high finesse cavities. To work towards such sizes, we performed a meltout experiment on SOI wavers etched to lower thickness. As the upper particle size is limited by the available volume of substrate material, a reduction in film thickness may serve to reduce both the required energy and overall particle size. To verify this we performed meltout

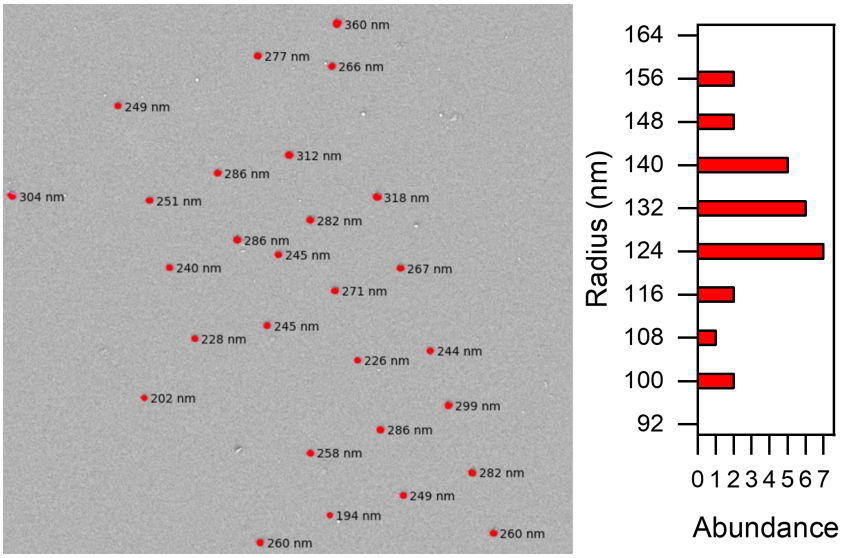

Figure 6.8: Left: Captured particles tagged by diameter using image processing software. The particles show a notable size spread due to the limited number of pixels per particle. Right: counted particles per size class. We see the majority of particles within the range of 230 to 280 nm diameter.

tests while varying the energy and focus on SOI samples that were etched down to thicknesses of 11,16,26 and 42 nm. For thinner substrates, the optimal energy region was shifted to lower energies, reflecting the reduced volume that needs to be heated. Within the correct energy range for single nanoparticle creation, the melting spots were qualitatively similar to the unetched silicon reference. The wavers showed a large amount of nanoparticles present around the target sites, while almost no particles could be observed on the capture slides.

Controlling focus and energy

Adjusting laser energy and focus allows varying the particle size range and makes the source mechanism flexible more than its counterparts. To test this dependence, we performed tests of various energies and focal distances, studying the effect of these two parameters with scattering electron microscopy. An increase in laser spot size leads to a higher energy requirement and larger particles. By varying spot size and energy, we were able to reliably create particles ranging from 160 to 350 nm in diameter. Figure 6.8 shows an image of a capture slide with particles created using $\simeq$10 nJ and a given size spread for this region

The particles have a most probable diameter of ≃260 nm, with a size spread of 13% FWHM. Different focal sizes show the same relative spread. This shows that increasing the particle size may be done with relative ease and is easily combined with methods to reduce particle size by controlling the substrate. With the two approaches usable in tandem, namely thin wavers with arbitrarily large meltout spots, a large size range may become accessible and controllable using a single in-situ source mechanism.

6.4.4 Gold

Gold is interesting because of its high polarizability and scattering cross-section, but also for matter-wave experiments as a material of high density that is susceptible to single photon ionization at deep UV wavelengths. To generate single gold nanoparticles, we used samples with a 100 nm thick gold layer, sputtered onto a smooth glass substrate. The meltout process was less controllable for single-particle creation, giving a significant fraction of multi-particle events. A set of typical meltout spots and particles are shown in figure 6.9. Here we observe

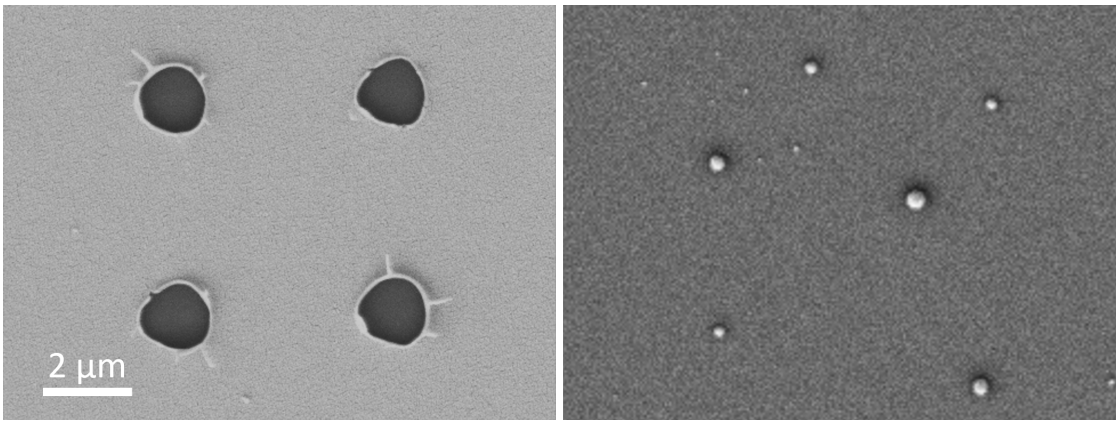

Figure 6.9: Left: Gold target surface after fs-laser illumination. The molten site exhibits signs of high energy, with no gold spire remaining in the center and visible molten edges. Right: Capture slide image of gold nanoparticle creation. The particles are placed randomly and show a significant size spread.

the targeted spots to be completely free of gold, with accumulations of gold on the edges. A corresponding image of the capture slide shows the created particles, with a noticeable size distribution centered around 400 nm diameter and imprecise placement. The multi-particle events proved useful for observing gold nanoparticles with scattering detection, with the larger particle size giving a more intense signal compared to silicon particles. The mean particle velocity for gold was around 50 m/s, however, enough particles with velocities below 1 m/s were produced to observe the trapping of gold nanoparticles. In addition to trapping times of up to 5 ms, cooling of the gold particles as they enter the cavity field could be observed. Figure 6.10 shows one example of this behavior. This cooling behavior was present both for tests at atmospheric pressure and at 10^{-2} mbar. As the size of the gold nanoparticles exceeded 400 nm in diameter, buffer gas cooling is a likely candidate.

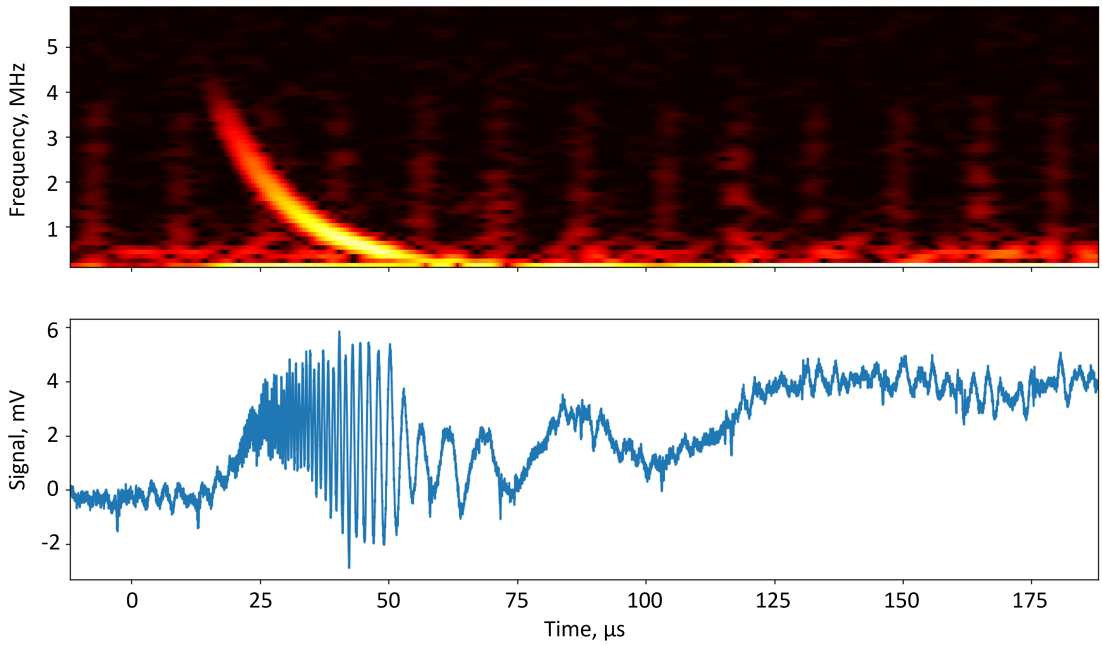

Figure 6.10: Top Fourier transform of the scattered light signal. We see evidence of slowing at the beginning, with the frequency dropping from 4 MHz down to below 1 MHz within 40 microseconds

6.5 Outlook

The results show that the laser-induced transfer method for creating size-selective particles for experiments shows great promise as a method for the creation of pure silicon nanoparticles. It can be used in high vacuum without reducing the vacuum quality and can be used semi-indefinitely due to the small amount of material used per creation. With custom-made targets with transparent supporting substrates [138], laser-induced forward transfer can become a viable method to directly inject particles into the trapping experiment from close distances. With the low energy required to operate in the single particle meltout regime, miniaturized lasers, and optics may be used to make a compact high vacuum particle source.
Metal particle generation is of particular interest for high-mass interference experiments. To control the size of particles created, one may adapt the substrate to different geometries, for example, pre-etching of the target to create islands of material, precisely controlling the volume available for particle formation[139]. Using such a method, it may become possible to limit the size of created nanoparticles to 10 nm or below, making the technique a powerful pulsed cluster source for high-mass experiments.

7 Pulsed interferometry past OTIMA

Interference experiments with high masses are an important goal in probing fundamental physics at the interface of quantum and classical mechanics. To this end, several approaches to high-mass interferometry are necessary. One approach is to work with single, massive nanoparticles that can be cooled and launched and perform repeated interference experiments. One possible avenue to reach these masses is the extension of the LUMI interferometer scheme[53], adjusting the grating period and remaining a continuous experiment. While LUMI has shown it can push towards high masses [1], the stability requirements for the future approach are the limits of experimental expertise. There is the cool Another avenue of progress is pulsed interferometry in the style of OTIMA, employing new techniques for light-matter interaction as a grating mechanism to overcome the limitations of OTIMA while retaining the advantages in this approach of interference experiment.

7.1 Limits of high mass interference experiments

To achieve interference experiments with high-mass systems, we have to overcome a variety of limitations. There is the matter of vibrational[81] motion of the interferometer, leading to fringe shifts during the measurement process. Other influences are thermal radiation giving which-path information[10], or collision events doing the same[80]. The sensitivity of an experiment to such events increases for high masses, as the expansion of the wavefront necessary for interference takes longer, and such events become more likely. The size of the interfered particle affects the performance of the depletion gratings. This is in addition to the initial challenge of preparing a stable source of particles for high-mass interference.

7.1.1 Vibrations

Noisy mechanical vibrations can modulate the interferometer fringes and reduce their contrast[42]. Vibrations with frequency ω add additional oscillation terms of the individual gratings $G^{(\mathrm{k})}, k = 1 - 3$ to the total grating shift 2.24

$$\Delta x_{vib}^{(\mathrm{k})} = \frac{2\pi}{d} A^{(k)} \sin\left((k-1)\omega T + \phi^{(\mathrm{k})}\right). \tag{7.1}$$

We implicitly average over these oscillations, reducing the observed contrast. We distinguish between the case of independent motion, and common-mode motion of the gratings [81, 42], as shown in figure 7.1. When undergoing independent motion, the gratings do not have a fixed phase relation to each other: they lack a common boundary like the single mirror of OTIMA.

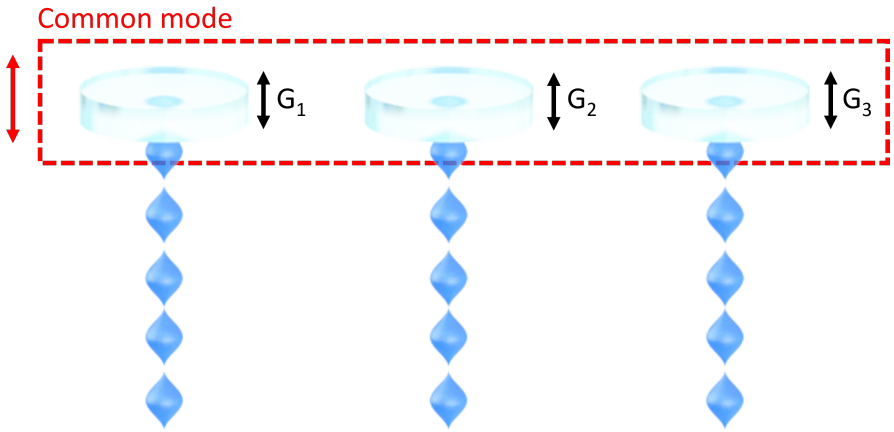

Figure 7.1: Translational vibration modes for a three rating interferometer. The common mode vibration (red) affects all gratings simultaneously, while the independent vibrations (black) have no common boundary.

Such vibrations lead to a visibility reduction of

$$\frac{V}{V_0} = \left| J_0\left(\frac{2\pi}{d}A\right)\right|^2 \left| J_0\left(\frac{4\pi}{d}A\right)\right|, \tag{7.2}$$

independent of the time separation ΔT between the gratings. Common-mode motion, where the entire system vibrates, affects the visibility differently, exhibiting a dependence on T

$$\frac{V}{V_0} = \left| J_0\left(\frac{8\pi A}{d}\sin\left(\omega\frac{T}{2}\right)\right)\right| \tag{7.3}$$

For independent vibrations of the gratings, the contrast is reduced to $\simeq 50\%$ for amplitudes $A^{(k)} = d/10$. For common-mode vibrations and a given grating pulse separation T, there exist favorable, resonant vibration frequencies and ones that lead to maximal dephasing of the recorded interference fringes[42]. In such a case, the contrast is reduced to $\simeq 50\%$ at $A = d/20$. For grating periods of around 100 nm, that gives us an upper bound for vibrations of $\simeq 5$nm. It is then always advantageous when considering vibrations to work with a common boundary, eliminating the problem of independent vibrations.

7.1.2 Collisional decoherence

A limiting factor in interference experiments is given by collisions with background gas. They provide which-path information and destroy the interference pattern.
The likelihood of these collisions grows with the evolution time and therefore with the mass of the system. This can be quantified by the visibility reduction factor $R_c = \exp(-2\Gamma_c T_T)$ [80] when considering a propagation time $2T_T$ through the interferometer. Here, Γ_c[80] is the

collision rate as the particle propagates through the interferometer

$$\Gamma_{\mathrm{c}} \simeq \frac{8p_{\mathrm{g}}}{k_B T_{\mathrm{g}}} \left(\frac{C_6^2 v_{\mathrm{g}}^3}{\hbar^2} \right)^{1/5}. \tag{7.4}$$

The parameters v_g, T_g, and p_g are the thermal velocity, temperature, and pressure of the background gas. From this, we can compute the background gas pressure where the contrast is reduced to $1/e$

$$p_c = \frac{k_B T_g}{16 T_T} \left(\frac{\hbar^2}{C_6^2 v_g^3} \right)^{1/5}, \tag{7.5}$$

The van der Waals coefficient C_6 depends on the static polarizability volume of both the background gas and the particle and therefore of the particle's mass, adding another scaling factor. It can be estimated using the Slater-Kirkwood formula [140]

$$C_6 \simeq \frac{3}{2} \frac{e\hbar}{\sqrt{4\pi\varepsilon_0 m_e}} \frac{\alpha_g \alpha}{\sqrt{\alpha_g/N_g + \sqrt{\alpha/N}}}, \tag{7.6}$$

where e and m_e are the charge and mass of the electron, with N_g and N the number of valence electrons for the background gas and particle respectively. Molecular nitrogen N_2, with static polarizability $\alpha_g = 1.74\text{Å}^3$, is the most abundant background gas up to 10^{-9} mbar, but for massive systems, we must push the pressure below that point. Here, it is more accurate to assume molecular hydrogen H_2 to give the main contribution for collision events. In this case, the required pressures are 20 percent smaller than for nitrogen, as the reduced polarizability of 0.8 Å^3 is compensated by the difference in mass.

7.1.3 Thermal radiation

Another limiting parameter that we must account for is thermal radiation. Complex particles emit black body photons, with wavelengths determined by the internal energy of the particle. This thermal radiation may lead to a localization of the particle, much like the case of particle-particle collisions. This is the case if the photon has a wavelength on the order of the grating period to provide which-path information of the particle, collapsing the spread-out wave function to a single point [10]. A longer evolution time ΔT allows for more emission events and gives a higher likelihood of decoherence. In figure 7.2 we can see the effect of thermal radiation and collisional events on the fringe visibility for various pressures and internal temperatures, assuming a grating of around 100 nm period We see that the temperature is a significant contributor to protein decoherence past 2 MDa at 500 K, leading to a total loss of contrast at $\simeq$4 MDa. To reach higher masses we must decrease the temperature. 100 K internal temperature prevents loss of contrast for experiments up to 100 MDa, the mass region of larger viroids [141]. For denser material and shorter grating wavelengths, the properties are relaxed, allowing interference without significant reduction in visibility for up to 10 MDa at 500 K. To reach beyond we require 200 K for experiment at 100 MDa and 100 K for 1 GDa. Observing the collision graphs, we see a noticeable reduction to below 50% in contrast after 1 MDa for 10^{-9}

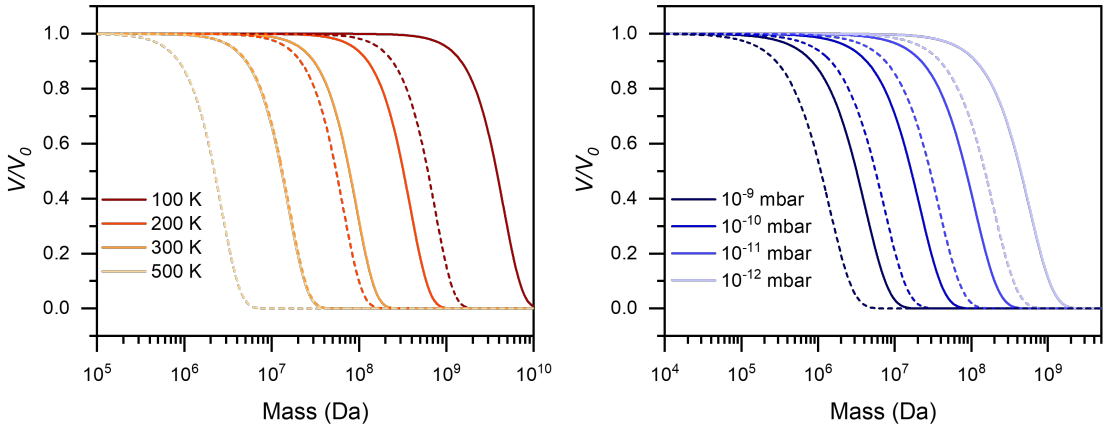

Figure 7.2: Left: Visibility reduction due to thermal decoherence as a function of mass, plotted for several particle internal temperatures. Right: Collisional decoherence rate as a function of particle velocity, chosen for background pressure levels of 10^{-9}, 10^{-10}, 10^{-11} and 10^{-12} mbar. The solid lines represent gold particles with a grating period of 106.5 nm. The dashed lines correspond to the average protein density and 133 nm grating period.

mbar pressure for proteins. Pushing the pressure down to 10^{-12} mbar eliminates collisional decoherence as a factor, even for viroids. The denser gold has relaxed conditions, dropping below 50% visibility past 3 MDa at a background pressure of 10^{-9} mbar.

7.1.4 Photon scattering in gratings

Particles can also Rayleigh scatter photons in the diffraction grating. Such a scattering event would lead to decoherence for the given particle, scattering occurs in a $\cos^2(\theta)$ pattern in a wide range of angles and with a photon momentum that suffices to scramble the pattern.
For small masses, the likelihood of such an event is minimal and does not lead to an observable change in fringe contrast. However, as the scattering cross-section grows more significant, these events start to visibly impact the observed visibility. The measure of note here is the relative strength of absorption σ_{abs} and σ_{sca}

$$\frac{\sigma_{\mathrm{abs}}}{\sigma_{\mathrm{sca}}} = \frac{4\pi^2 m|\varepsilon - 1|^2}{3\varrho\lambda^3 Im(\varepsilon)} \tag{7.7}$$

For identical strengths of scattering and absorption, the contrast is reduced to $\simeq 80\%$ of the maximum.

7.1.5 Particle size

The particle size determines the scattering rate for light and particles. Moreover, once it is a tenth of the grating period d, the point particle approximation fails[52, 142]. The main effect is

a reduction of the transmission through the interferometer. This effect becomes significant at different mass scales depending on the probed system. For dense metal clusters, such as gold clusters, with a density of 19.3 g/cm^3, only molecules beyond 10 MDa see a drop in transmission below 90 % of the point particle value. This reduces to 10 % relative transmission at 100 MDa. Combining this with the signal constraints for larger systems, this effect becomes a serious consideration for interferometry. In the case of proteins, with a mean density of 1.4 g/cm^3, this effect becomes apparent much sooner. Here we expect the size of the particles to reduce the final signal below 90% of the point particle expectation at 40 kDa, reducing to below 10% past 2 MDa. As most proteins inhabit the mass region spanning 6 kDa (for insulin) to 100 kDa (for ribonuclease[143]), the loss in transmission does not exceed 50%. A plot of this effect is shown

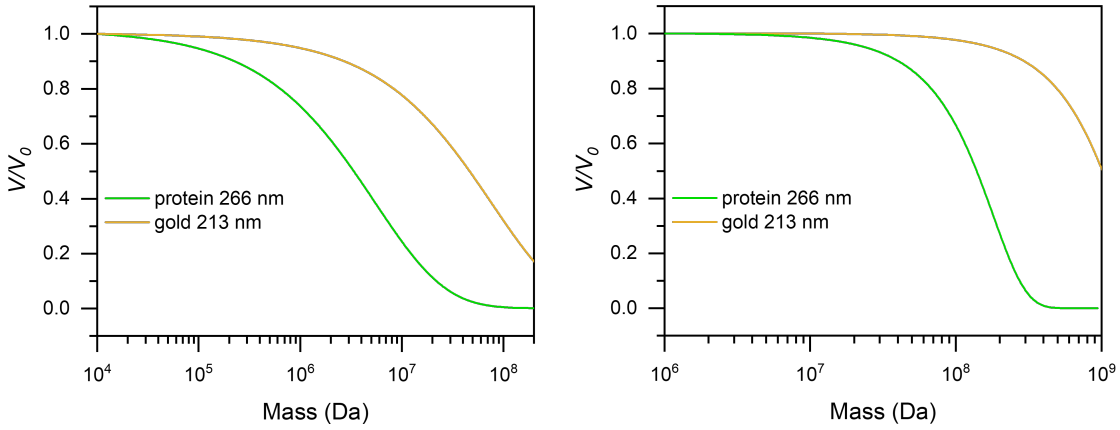

Figure 7.3: Left: Relative particle transmission as a function of particle mass. The yellow line shows the effect for gold with a density of 19.3 g/mm^3, while average protein densities of 1.4 g/mm^3 are described with the green line. We see a divergence from the point-particle expectation starting at 1 MDa for gold, and 10 kDa for biological matter and reducing to $\simeq$10% for $10^8(3\times10^6)$ Da. Right: Visibility reduction due to Rayleigh scattering of light in the gratings. For the simulation of gold, the grating period was taken to be $d = 106.5$ nm, assuming a 106.5 nm grating period. For proteins, a grating period of 133 nm was assumed.

in figure 7.3, where we see the reduction in transmission for particles like metal clusters in the case of gold, or usual protein densities. This shows that we already must expect a relevant reduction in transmission due to the particle size in the case of usual protein masses of $\simeq 50$ kDa. Similarly, in the case of heavy metal clusters, we must assume a loss in overall signal starting at 1 MDa and becoming significant past 10 MDa.

7.1.6 Gravity

Gravity is one of the strictest limits for high mass interference on Earth. Most obvious is the fall distance of the molecules, which is proportional to T^2. For masses larger than 10^6Da, this may quickly grow to be a significant distance, up to over 100 meters for 10^8 Da. Another limitation

is the fall $velocity$. Should the gratings be aligned parallel to gravity, the growing velocity component may cause the particles to traverse several grating nodes during the light pulse. Averaging over the grating nodes then causes a loss of fringe visibility. To compensate for the influence of gravity, we may introduce an upward component to the velocity of particles[53]. The optimum case for compensation for an experiment lasting $2T$ is an initial vertical velocity of gT. This reduces the interferometer height by a factor of four and the maximal transverse velocity by a factor of two. Full or partial compensation of gravity in this way may allow experiments with particles up to 10 MDa mass within a 1 m vertical region, and thus remain viable for tabletop experiments. As the timescale of the experiment plays a crucial role in these limits, it is of great interest to find ways to minimize the required evolution time through the interferometer.

7.1.7 Coriolis effect

Another matter to consider for interferometry experiments with long interrogation times is the effect of the Coriolis acceleration. It causes a shift in the interferometer fringes 2.24 dependent on the orientation of the experiment's alignment to the rotation of Earth $\vec{a}_C = -2\vec{\Omega} \times \vec{v}$. It affects the particles in the vertical direction, as well as in the horizontal plane:

$$\begin{pmatrix} a_{ver} \\ a_{lat} \\ a_{lon} \end{pmatrix} = 2\Omega_E \begin{pmatrix} v_{lon}\cos(\phi_{lat}) \\ v_{lon}\sin(\phi_{lat}) \\ v_{lat}\sin(\phi_{lat}) - v_{ver}\cos(\phi_{lat}) \end{pmatrix}. \tag{7.8}$$

Here Ω_E is the angular velocity of Earth, ϕ_{lat} is the latitude of the experiment, and v_{ver}, v_{lon} and v_{lat} are the vertical, longitudinal and latitudinal velocity of the particle respectively. The Coriolis acceleration is small compared to gravity, even for particles with a velocity of 1000 m/s only accounting for one percent of gravity. However, the velocity dependence of $\vec{a}_C$ makes it sensitive to the velocity spread of the molecular beam, even in a pulsed experiment. Taking the case of vertical gratings with a fixed distance L, we can expect a visibility reduction due to the velocity spread of

$$\frac{V}{V_0} \simeq \exp\left[-8\left(\frac{\pi\Omega_E \Delta v \cos\phi_{lat}\delta T L}{v dv}\right)^2\right]. \tag{7.9}$$

The relative velocity spread $\Delta v/v$ becomes more important for higher masses, due to the increased interrogation time. Figure 7.4 shows the relative contrast for 0.5 %, 1%, 5% and 10% velocity spread. We see a reduction in contrast by 50 % starting at 500 kDa for a 10% velocity spread, with 0.5% able to go up to a mass of 9 MDa Dalton before the same reduction. Partially compensating for Coriolis in the horizontal plane is possible by adjusting the grating angle versus gravity[42], while the vertical effect can be suppressed by choosing the experimental alignment to be perpendicular to the longitudinal direction, i.e., north facing.

Qualities of a pulsed experiment

While the collimation requirements in the case of a perfect parabola are prohibitive [53] with 10 μm, given a finite spread in velocity. A pulsed experiment does not incur these limitations

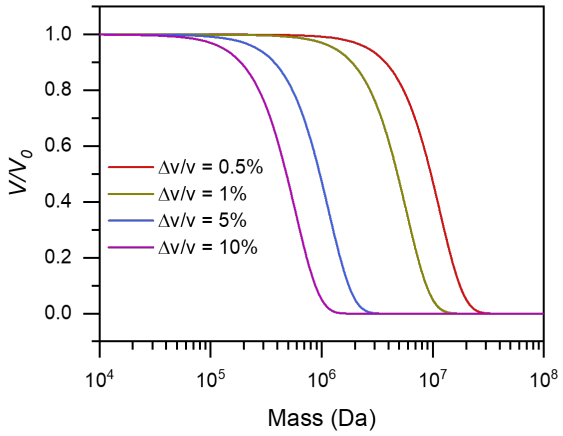

Figure 7.4: Visibility reduction due to uncompensated Coriolis dephasing, assuming a velocity spread of 0.5%(dark green) to 10% (bright green). For this graph, a grating wavelength of 266 nm and a distance L of 0.12 m between gratings was assumed

because of the simultaneous illumination of all particles for sufficiently extended light gratings. Another advantage to note is technical. Acquiring powerful lasers of short wavelengths is easier for pulsed experiments, as the concentration of the light in a short pulse allows for more efficient conversion mechanisms.

These advantages come with the difficulty of acquiring a strong signal. Since it is vital to ensure all detected particles have interacted with the full interferometer sequence, only a small fraction of the velocity distribution in the beam is sampled. This strict velocity selection, on the order of 0.5 % in OTIMA, makes acquiring sufficient counts more challenging than a continuous interferometer scheme like LUMI, where more than 10 % of the velocity distribution can be sampled. This can be compensated for by more extended grating pulses and a larger detection area, which increases the effect of the Coriolis dephasing.

7.2 A pulsed interferometer for proteins

The successful interference of gramicidin showed the potential for accessing large neutral biomolecules for interference measurements. Past gramicidin lies the mass and complexity range of proteins, with insulin the smallest possible protein with 51 amino acid residues. Proteins are intriguing targets for interference experiments because of their complexity. Unlocking this category of molecules for interference is a challenging task, however. Proteins are difficult to transfer into the gas phase without damaging their structure. It has proven even more difficult to post-ionize neutral gas phase proteins. These roadblocks need to be cleared to unlock interference experiments with this class of molecules.

7.2.1 A stable beam source for proteins

The biggest challenge in performing interference experiments with proteins lies in the creation and detection of a neutral beam of molecules. To realize such a beam, several things need to be considered.

Creating the beam

First to consider is the creation of the beam: under what circumstances can the proteins be transferred cleanly into the gas phase? What is the charge state of the molecules after evaporation? Are there secondary processes such as cluster formation or thermal degradation? The goal of a 'clean' protein is soft evaporation without damaging the proteins and minimizing beam contaminants such as chunks droplets or clusters. Evaporation without damage may be done using several methods, the top contenders of which are electron spray ionization (ESI) and matrix-assisted laser desorption (MALDi). Both may be used to create a beam of neutral or charged proteins that have successfully survived the transition into the gas phase. ESI has the advantage of extreme sample efficiency, transferring nearly the entire sample into a molecular beam. The initial charge of the beam can be controlled with additional tools [144] to produce a majority of proteins in the intended charge. However, the technique still has limitations. The first is the nature of beam creation. To produce the beam, a spray of the solution is aerosolized using an electron spray that leads to a Coulomb explosion of the droplets. This gives the charge distribution, which can be quite significant. With average charge states as high as +30, for hemoglobin, it is challenging to tune these beams to produce the neutral or singly charged molecules necessary. Further, the continuous nature of ESI may make it less suitable for interference experiments with pulsed gratings.
Adaptations of the laser methods used in OTIMA may be more attractive to the creation of molecules with a single charge. Change to a MALDi process by adding a matrix capable of protonating the proteins, and it is possible to obtain a beam of ions from a point-like pulsed source. While the ratio of ions to neutrals is only 10^{-3} to 10^{-4} [82, 145], the potential of guiding and slowing the charged proteins makes it possible to retain a majority of the ions in the beam for interference experiments. MALDi method also has the advantage of being compatible with a supersonic expansion nozzle to cool the molecules internally and direct them toward the experiment within a small velocity spread.

Beam control

For some mass regimes, it may become necessary to slow the molecules down to fit with the geometry of the interferometer. With the potential of charge control using photolabile tags, it is possible to start with a beam of ions guided and slowed with electric fields, which can then be neutralized for interference experiments. In the case of electric slowing several things are to consider. Firstly, the particles must be guided towards the experiment properly by the use of guiding fields, which may impact the quality of electric slowing. Secondly, it is difficult to truly 'cool down' particle motion by merely applying electric fields. Usually, a reduction in forward velocity does not slow them laterally, leading to a larger beam divergence.

However, using a combination of time-dependent fields and taking advantage of the potential for instantaneous neutralization, headway can be made. One potential configuration is a slowing geometry reminiscent of a time-of-flight mass spectrometer, shown in 7.5. Particles are first

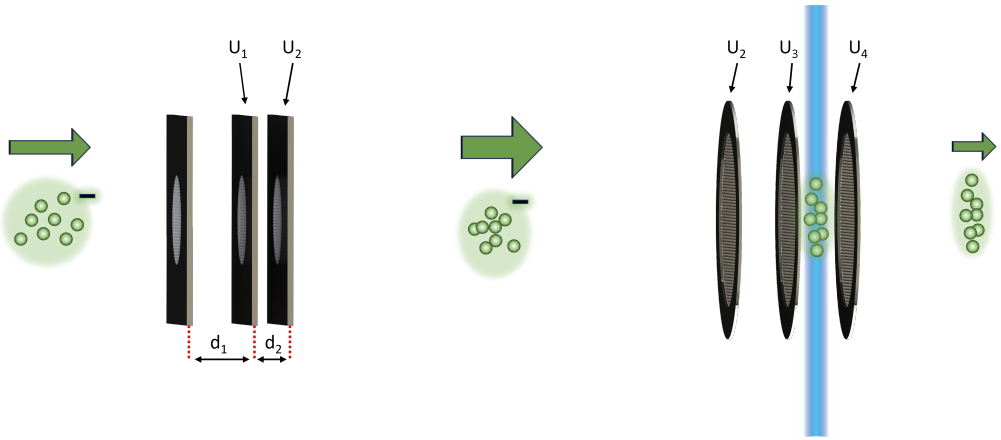

Figure 7.5: Slowing scheme for ions inspired by a ToF-MS approach. The particles are sped up and separated by their mass. The voltage of the electrodes is chosen to focus the particles in the turning point of the electrostatic mirror. A light pulse neutralizes the slowed molecules, which exit the slowing setup into the experiment proper.

accelerated and are spatially focused onto a point l_F.

$$l_F = 2d_1 k^{\frac{3}{2}} \left(1 - \frac{d_2}{(k + k^{\frac{1}{2}})d_1}\right). \tag{7.10}$$

This distance is governed by the ratio of acceleration voltages $k = U_2/U_1$ and the distance d_1 between electrode one and ground, and electrode one to electrode two d_2. After acceleration, the molecules enter a slowing stage in the form of a two-stage electrostatic mirror. Before the particles reach the peak of their travel in the slowing zone, they can be neutralized with a pulsed laser. By tuning the delay of the laser pulse, particles can be neutralized at the optimal time to produce a package of particles of the desired velocity.
Additionally, with the acceleration stage, it is possible to separate the clusters in the beam by their mass. This change in arrival time at the apex can then be used to post-select the mass region of interest from the molecular beam, effectively selecting only the molecules of interest from the source.
The disadvantage of this technique is the lack of control for cooling the transverse directions. As a result, the beam divergence increases with more powerful slowing, leading to a heavier loss in signal intensity over the same distance. This limits this technique to transversally cold sources of proteins, which can accommodate the increased divergence. Using laser desorption in combination with supersonic expansion 3.2.2 can provide the beam parameters needed. The sharp velocity distribution and powerful cooling of this source make it a good companion to the slowing method. To obtain beams with larger molecules, it is possible to use a heavier

carrier gas, giving both a lower beam velocity and better energy transfer for the impacts. Using Krypton for example, we obtain a velocity of ≃390 m/s at room temperature, or ≃240 m/s when cooling the valve to the boiling point of Krypton at 120 K, which can be done using a nitrogen cryostat [146]. A heavier carrier gas has the additional advantage of improving the cooling of the vibration and rotation degrees of freedom[89], reducing the thermal decoherence rate of the molecules.

7.2.2 Interferometer designs

To perform interference experiments and proteins, an interferometer suitable to the task is needed. Here we must observe the limitations given by the nature of protein beams and adapt the interferometer to match. Building on the framework of OTIMA, the interferometer shall be based on a single boundary, providing vibrational stability and ease of alignment. This can be implemented by using a single interferometer mirror, which ensures perfect flatness between mirrors but is limited by the substrate stability and available size. Alternatively, a Zerodur substrate with high rigidity and low thermal expansion may be machined to the required flatness and complemented with three individual mirrors. This gives the interferometer more overall stability but introduces strict alignment requirements in-between the three mirrors, as angle differences of as small as 10^{-7} rad can cause significant dephasing in the fringe contrast.

The choice of grating

For a purely optical interferometer, the choice of wavelength is important. In OTIMA, the laser wavelength of 157 nm was chosen to have the highest chance of single photon ionization as a universal grating mechanism. For a protein interferometer, this wavelength does not produce the needed single photon response necessary for efficient gratings. It is then necessary to look for new options. With the possibility of using photocleavable tags as a means for controlling the charge state of a molecule, the laser wavelengths for an interferometer are more flexible. The scaling of the Talbot time 2.9, proportional to d^2, is an important factor to consider. Large grating periods then translate to long evolution times and make the requirements on the molecular beam more strict. To keep T_T as small as possible it is preferable to work in the UV regime.
As 266 nm light has shown success as a cleavable tag, it is an enticing candidate for use as a grating. This wavelength has several advantages. Light gratings formed by this wavelength have a period of 133 nm, giving a mass scaling of 44.3 ns/Da. Compared to OTIMA, we would require a ≃3 times larger interferometer to target the same mass. With the availability of high-quality optics for 266 nm on fused silica substrates, it is possible to exceed this number. Such substrates are easier to machine and prepare and the size of the interferometer mirror could be extended from 5 to up to 25 cm. The potentially increased interferometer length leads to an overall improvement in the mass scaling, which is lost when considering larger wavelengths such as 355 or 532 nm, which give a mass scaling of 78.96 ns/Da and 177.32 ns/Da respectively. Lasers for 266 nm light have an additional advantage in their coherence length L_C. Using a seed laser, it is possible to obtain a coherence length of ≃25 cm, as opposed to 1 cm, which improves the available space between the molecular beam and interferometer drastically. This will both improve the standing wave quality and make it possible to implement new methods

for scanning the phase of the matter wave fringes.

Scanning the interferometer phase

When using a single mirror for all gratings, scanning the phase by shifting G_3 becomes challenging. In the prior OTIMA experiment, quantum interference was probed by performing interference measurements, as well as reference measurements outside the resonance condition. A comparison of the signal revealed the the quantum fluctuation of the signal. This indirect method was chosen to overcome the short coherence length of the F_2 laser beams forming the interferometer gratings. With the potentially longer coherence lengths of 266 nm lasers, new options become available. One such method may be the geometrical shifting of the standing

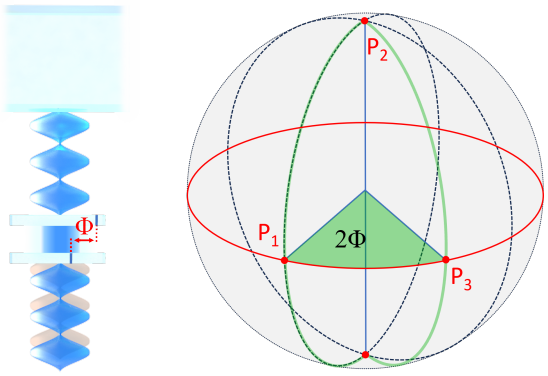

Figure 7.6: Left: image of the phase scanning scheme. The light passes through two quarter wave retarders with a relative angle ϕ and reflects from the mirror. This introduces a geometric phase, that can be shifted by varying the angle. Right: Polarization vector path of the light passing through the phase retardation setup. Starting from the point P_0 on the sphere with linear polarization, the light passes through QWP1. With the fast axis aligned at 45° to the incident polarization, it is changed to right-circular polarization P_1 and returns to linear polarization after QWP2 (P_2). After reflecting off the mirror, the light is transformed by QWP2 to left-circular polarization (P_3). Finally, by passing through QWP1, the journey ends at P_0. The angle difference θ between the fast axes of QWP1 and QWP2 then leads to a 2θ phase shift of the light, the Pancharatnam phase

light phase using two quarter-wave plates with a relative angle difference ϕ[147]. This has proven viable for atom interferometry and can allow G_3 to scan over the interference fringes. With this, we would not require a reference measurement to quantify the fringe contrast. The phase shifting mechanism is an application of geometric phase [148], and can be visualized on the Bloch sphere (see figure 7.6). Starting with incoming linearly polarized light, the first quarter wave plate turns the polarization circular. Combined with the mirror, the second quarter wave plate effectively can be treated as a half-wave plate that rotates the circular polarization on the sphere. Completing the circuit by passing through the first quarter wave plate again recovers

the linear polarization, however the relative angle between the wave plates ϕ is imprinted as a 2ϕ phase shift onto the standing wave. As this method shifts the phase by changing the relative angle of the two-phase plates over 2π it is sturdy towards vibrations. The angle ϕ can be controlled with high precision using motorized mounts, which can be accurate down to $\mu\mathrm{rad}$. The method may depart from the sinusoidal case due to several factors [93], and it is necessary to modify the Pancharatnam phase to account for the quality of the quarter-wave plate and imperfect alignment. To take advantage of a high standing wave fidelity, it is necessary to make the rotation system very compact

Combining the single mirror setup with non-mechanical phase scanning mechanisms may provide great improvements to the experimental procedure of OTIMA while maintaining the sturdiness against vibrations inherent to a single mirror system.

Particle mass and detection

To perform interference experiments within the mass range for proteins of 10 to 100 kDa, we require detection methods suitable to this range to accumulate the necessary counts for interference measurements. Using a ToF-MS with MCP stacks for this purpose is possible, however with reduced efficiency for higher masses. Using the ToF-MS of the OTIMA setup 3.2.1 with a 16 kV acceleration voltage, the detection efficiency would drop to 25% at 100 kDa[149, 150]. The particle detection is then no significant limit to the viability of a protein interference experiment.

7.2.3 Interferometry with insulin

Observing the limits for interference experiments seen in 7.1, and the potential for photoactive tagging at 266 nm [45], we can imagine insulin to be the next milestone for biomolecule interference. With a mass of $\simeq$ 6000 Da, we would be operating below the mass regime where reductions in contrast and compromises about signal quality become relevant. Given the evolution time of 2.66 ms in between grating pulses to reach the first Talbot order, and assuming a mirror with 25 cm extension along the beam path, we would require a particle velocity of $\simeq$450 m/s, already achievable with an Even Lavie valve using Argon at 200 K. This would allow us to perform experiments using source techniques already proven to be viable for biomolecular beam creation[101, 2]. With an initial velocity suitable for the likely interferometer geometry, there would be no need to prepare the insulin as a beam of ions initially. This would also allow us to skip the neutralization stage of the slowing process, simplifying the chemical synthesis required for experiments. To observe interference, we would require the grating photons to either fragment or ionize the system. Photo fragmentation is a simpler choice, as photo labile tagging with homolytic cleavage is already possible[151]. Observing the photo-fragmentation cross-sections observed in Chapter 5, we would require pulse intensities on the order of 3 mJ/cm^2 to obtain an average grating strength of $n_0 \geq$4. Photolabile tagging with $heterolytic$ cleavage is likely to yield lower cross-sections but allow us to obtain a grating and detection mechanism at the same time, simplifying the interferometer design. With an assumed cross-section of $\simeq 10^{-17}$ cm^2, we would require 60 mJ/cm^2 pulse intensities, achievable by focusing the grating laser pulses using cylindrical lenses. To reach insulin interference, it is necessary to build and

test the new interferometer based on 266 nm light gratings, as well as refine the photo-cleavage process. We may then combine the two necessary ingredients for interference experiments: the molecular beam and interferometer techniques.

8 Beyond interference

With a new generation of interferometers approaching that can perform experiments with complex, massive systems that have been inaccessible to date, it is useful to look toward the potential uses such interferometers may have.

8.1 Measuring molecular properties of proteins

The nanoscale sensitivity inherent to experiments probing for matter-wave interference makes them an attractive tool for probing small forces[152] and probe fundamental physical questions [153, 154]. However, this sensitivity may also be used in reverse: probing the properties of the interfering particle[54]. As the systems that become accessible to interference experiments become ever larger and more complex, the own internal structure and properties become interesting as a field of study. To this end, it is possible to adapt an interference experiment to probe these internal properties on a scale that is inaccessible to classical beam experiments. With the possibility of protein interference with the new pulsed interferometer under construction in the Arndt group, knowing the ways to use the sensitivity of such experiments is of great interest.

8.1.1 Deflectometry

The conceptually most simple way to probe molecular properties is by performing deflectometry experiments. Such experiments aim to introduce a beam shift by targeting the internal properties of the particles. This is done by applying controlled electric or magnetic fields. As such, deflectometry experiments aim for knowledge about the electric and magnetic properties of particles: dipole moments and polarizabilities, magnetic moments, and susceptibilities. The molecular beam initially travels through the field-free experiment until it reaches the deflection region of length L_1. Here the particle is subjected to force F_x along a direction that imparts a beam shift Δx_F

$$\Delta x_F = \int_0^{L_1} \mathrm{d}z \int_0^z \mathrm{z}' \frac{F_x(z')}{mv^2}, \tag{8.1}$$

and a velocity kick

$$\Delta v_F = \int_0^{L_1} \mathrm{d}z \frac{F_x(z)}{mv}. \tag{8.2}$$

After exiting the deflection region, the new particle trajectory leads to a shift of the molecular beam. The displacement can be measured using position-sensitive detection schemes[155], for example by using a movable collimation slit to filter the detected signal. To probe the electric

properties of a molecule, we can apply an electric field in the form of $(\vec{E}\nabla)E_x = const.$ This gives us access to both the permanent and induced dipole moments with the acting force

$$F_x = (\vec{d}\nabla)E_x \tag{8.3}$$

Here, the dipole may be permanent, leading to a broadening of the beam, or induced by the electric field acting on the susceptibility $\chi_E = \alpha_0 + \langle d^2 \rangle_T / 3k_B T$. It is composed of the static polarizability α_0, and the so-called Van Vleck term, a thermal average of the squared molecular dipole moment. The static polarizability gives a shift in the beam as the molecules align with the field, while permanent moments lead to a broadening of the beam. The case of magnetic deflection is similar, with a field of $(\vec{B}\nabla)B_x$ giving us access to the magnetic susceptibility χ_M and permanent moment $\vec{\mu}_M$.

$$F_x = (\vec{\mu}\nabla)B_x \tag{8.4}$$

Such experiments are a much-used tool for probing the characteristics of molecules[156, 157, 158, 159, 160], as with sufficient field strength the beam deflection is visible for classically achievable spatial resolution. Introducing an interferometer sequence to such experiments can make them sensitive to beam deflection on the nanometer scale. The sensitivity to small phase shifts makes it possible to probe the properties of systems that are more difficult to probe classically[57, 57]. In an interferometer, the total shift takes the form

$$\Delta x = \pm \left(\Delta x_F + v_F \frac{L - L_2}{v} \right), \tag{8.5}$$

depending on if deflection occurs before (+) or after (-) G_2 in the interferometer sequence. For finite velocity spreads, one must average over the different times spent inside the field, giving a reduction in contrast. Here, a pulsed experiment can benefit from the usually small detected velocity spread.[2].

8.1.2 Collision studies

Measuring the collision cross-section of gas phase samples is of particular interest for determining their structure. As such, it has seen the most use in the field of structural biology, where information regarding protein structure and the possibility of characterizing different types and conformations is much sought after. The main technique for measuring the collision cross-section is ion mobility spectroscopy. It is based on guiding the particles of interest through a drift tube filled with a well-characterized gas mixture by applying an electric field. The drift velocity may then be related to the collision cross-section of ion and gas. While a well-developed and powerful tool to obtain structural information, this method is limited to ions only, which may lead to different conformations than the 'native' state. A reliable method for determining the cross-section of neutral systems is not easily found, and it is here that interference experiments may shine. Due to the sensitivity of the interference measurements to collision events, they are uniquely suited to determining collision cross-sections. Any single collision event during a particle's journey through the interferometer will lead to localization and thus loss of interference. With equation 7.4, we have a measure of the likely number of collision events for

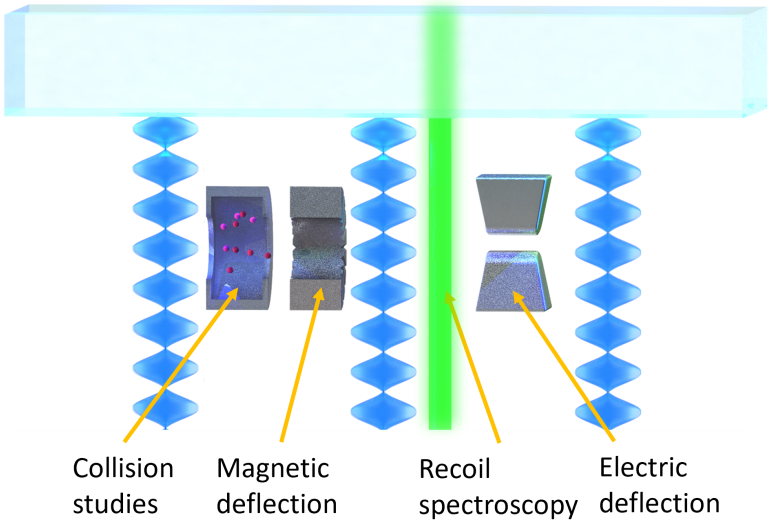

Figure 8.1: Image of the different potential tools for molecular measurements in a matter wave interferometer. From left to right the options are buffer gas cells to study collision properties of molecules. Magnetic and electric deflection experiments probe the susceptibilities and permanent dipole moments. Spectroscopy experiments probe the optical properties of molecules, such as absorption cross-section and polarizability

a given particle and pressure. By introducing a collision gas cell with controllable pressure, we may use this sensitivity to measure the loss of fringe contrast as a function of gas pressure. This could enable studies of the collision interactions of large neutral systems to obtain structural information.

8.1.3 Recoil spectroscopy

Talbot Lau interferometers may also make it possible to probe the optical properties of proteins. Especially interesting here is the potential for recoil spectroscopy. Gas phase spectroscopy conventionally comes in two main forms[161, 162]. The first is a close analog to liquid or solid sample studies, where a cloud of molecules is created to attenuate the spectroscopy laser[163]. This method relies on the ability to create dense vapors of the molecule in question and is thus poorly suited to larger more fragile systems. The second, action spectroscopy, relies on visible reactions to photon absorption such as dissociation [164], ionization [165], or fluorescence [166], all of which become less likely for biomolecules as they grow in size and have more internal degrees of freedom to disperse the photon energy. In an interferometer, it is possible to detect the momentum kick imparted by the photon and use this minuscule effect to quantify the absorption event[167].
Recoil spectroscopy has already been successfully used to probe the optical properties of systems sturdy towards conventional action spectroscopy[58] The scheme for recoil spectroscopy, shown in figure 8.2 is as follows: In addition to a normal interference measurement to determine S_N,

we add a second measurement cycle. In this cycle, a recoil laser with energy E_R, set to the same time as G_2, is activated. Particles passing through the running wave light may absorb photons.

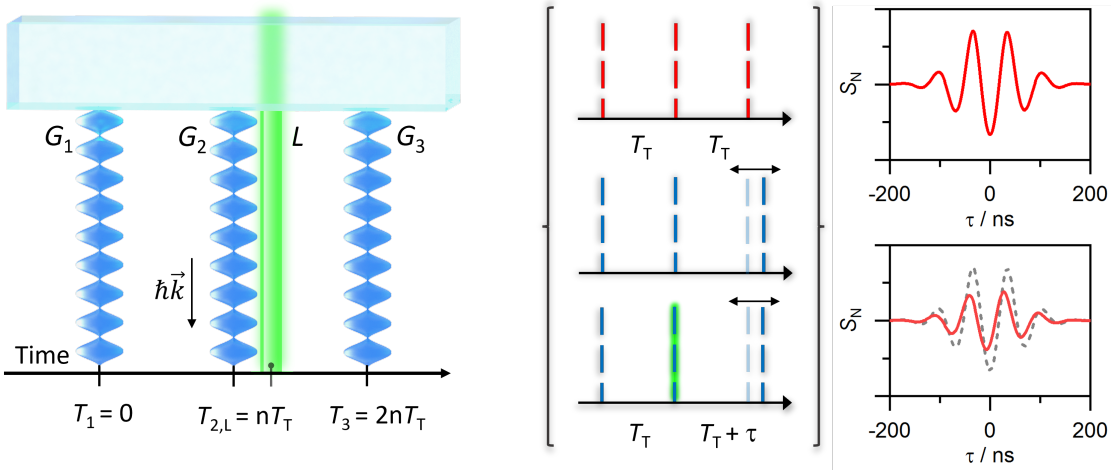

Figure 8.2: Te measurement scheme for photon recoil measurements. The Initial interference scan is complemented by a measurement with an active recoil laser. The running wave imparts a momentum kick on the proteins absorbing a photon, resulting in a shift in the pattern. The observed fringes are then averaged over the different momentum kicks imparted on the molecules in the beam. The resulting loss in contrast can be related to the absorption cross-section

Should a particle absorb a photon in this way, it will receive a momentum kick $\hbar k_R$ that will lead to a shift in the final fringe pattern

$$\Delta x_R = \frac{Td^2}{T_T \lambda_R}. \tag{8.6}$$

Since the absorption events are random, the presence of the recoil laser leads to a distribution of discrete momentum kicks and shifts, reducing the observed fringe contrast. To quantify the effect of the recoil laser we then look at this reduction in contrast. Looking once again at 2.25, we obtain a reduction

$$\tilde{S}_\ell \;=\; S_\ell \exp\left(n_R\left[1-\exp\left(\frac{2\pi i \ell T d}{T_T \lambda_R}\right)\right]\right) = R_\ell S_\ell. \tag{8.7}$$

It depends directly on n_R, the mean number of absorbed recoil photons

$$n_0 \;=\; \frac{\sigma_{abs} E_R \lambda_R}{hcA_R}. \tag{8.8}$$

This gives us direct access to the absolute absorption cross-section of the particle by performing the recoil measurement. The sensitivity of the recoil measurement depends on the strength of the momentum kick and as such the wavelength used. Assuming a grating period of 133 nm,

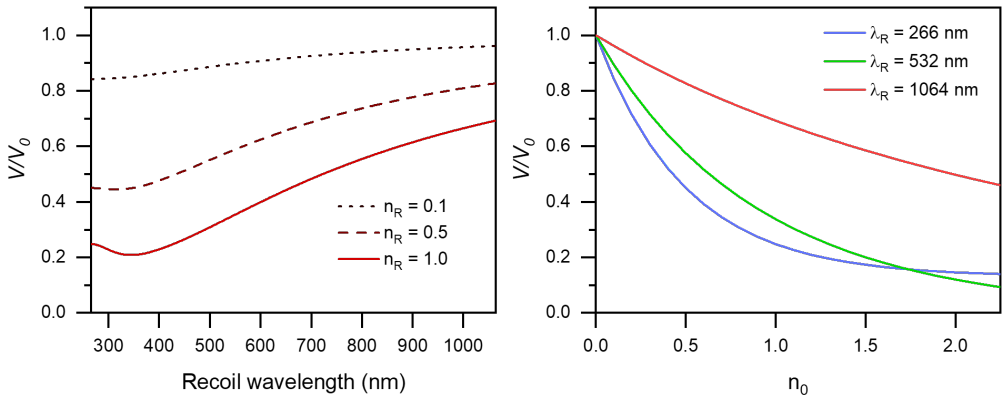

Figure 8.3: Left: Simulation of an interference scan for different mean photon recoils. The peaks lose in strength and the relative reduction can be extracted by measurements. For small photon numbers and high recoil wavelengths, this requires high initial contrast to see.
Right: Scan of the contrast reduction for varying n_R, displaying both S_N and V_{sin}. We see that the

which is a strong candidate for protein interferometry, we can observe the reduction strength for different wavelengths. Figure 8.3 shows plots of the contrast reduction for various wavelengths, for a variety of n_R. For increasing wavelengths λ_R, the contrast reduction decreases to below 10% at 560 nm, for 0.1 photon absorbed on average, which is within the usual uncertainty range for an initial visibility of 40%. For stronger absorption, we can expect to see reductions of $\geq$ 20% over the range of 266 to 1064 nm. We then need both strong initial contrast and high recoil-laser energy to ensure recoil events lead to visible reduction. Another method is to extend the time after the momentum kick. Increasing the pulse separation times of the interferometer to higher Talbot orders $T = nT_{\text{T}}, n > 1$ gives a boost in sensitivity due to the larger shift. This can be seen as effectively reducing the wavelength of the spectroscopy laser and can make recoil spectroscopy potentially viable for spectroscopy in the infrared as well. The challenge in this approach lies in the required evolution time of the probed molecules. Large systems are more difficult to interfere in higher Talbot orders, as the velocity requirement becomes more strict.

For recoil spectroscopy tests it is important to account for photo relaxation effects like fragmentation and fluorescence. Fluorescence of the molecule after absorption leads to an additional reduction in contrast due to the isotropic emission of the photon. This additional reduction in contrast is in addition to the recoil of the absorption event and needs to be accounted for to correctly quantify the absorption cross section[59]. This makes it difficult to still obtain a quantitative measure of the absorption cross-section, making it necessary to rule out fluorescence as a factor for precise measurements.

8.2 A pulsed interferometer with gold clusters

Interference experiments with high macroscopic systems are an important tool for probing fundamental physics. The approaches for realizing such experiments are manifold[41, 168] and will enable us to probe quantum mechanics on a powerful scale. Considering the technological challenges involved in such ventures, it is useful to observe and revisit different concepts. Molecular beam experiments have shown a large degree of macroscopicity, that can further be improved in the future [1, 53]. For a truly high mass interference experiment using molecular beams, metallic clusters are a strong candidate, and are currently being explored with 266 nm light in LUMI. As pulsed interferometry experiments are an important analogue to continuous experiments I want to motivate the potential of a pulsed interferometer for metal clusters.
Due to the high density compared to other systems, metal clusters adhere to the point particle approximation until very high masses, reducing the negative impact on the grating transmission caused by finite particle size. The threshold energy for photoionization can be exceeded using tabletop lasers, making it possible to have single photon depletion gratings and charge state control. Finally, standard sources of metal clusters perform with high efficiency and create intense beams[169], both attractive qualities in a molecular beam source. Creating stable beams of high-mass clusters is then a much more achievable task for preparing interference experiments compared to other particle candidates.

8.2.1 Grating wavelength

The first question is once again the choice of wavelength for the interferometer. Here it is advantageous to go to the lowest wavelength possible without sacrificing standing wave quality. This improves both the interferometer mass scaling, as well as unlock metals with higher work function for interference experiments[170]. A strong candidate here is 213 nm light, which is commercially available for pulsed lasers. The 5.82 eV photon energy at this wavelength is sufficient to ionize many different metals [171] with a single photon. This ensures an efficient grating mechanism for depleting the molecular beam and observing quantum fringes. For gratings of 106.5 nm period, the Talbot length is $T_T = 28.4$ ns/Da, compared to 44.6 ns/Da for 133 nm gratings. While pulse energy is limited compared to 266 nm, for more massive clusters the absorption cross-section is large enough to allow ionization with even weak light pulses. For 213 nm light, lasers with coherence lengths of up to 20 cm are available, enabling a standing wave fidelity of over 70 $\%$ for distances up to 5 cm away from the mirror. This is sufficient room to include phase scanning mechanisms in the beam line of G_3. Optics for 213 nm are of similar quality to 266 nm optics, enabling efficient guiding and shaping of the light grating.

8.2.2 Choice of metal cluster

For this work, I will place the focus on gold. With a work function of 5.3 eV, gold may be ionized using 213 nm photons, allowing for efficient grating mechanisms and charge control for beam preparation and detection. The high density of gold gives it a favorable mass-to-size scaling compared to other metals, minimizing the effects of finite particle size until 10 MDa. Finally, its positive polarizability [172] can push the resonance condition for optimal contrast to noticeably

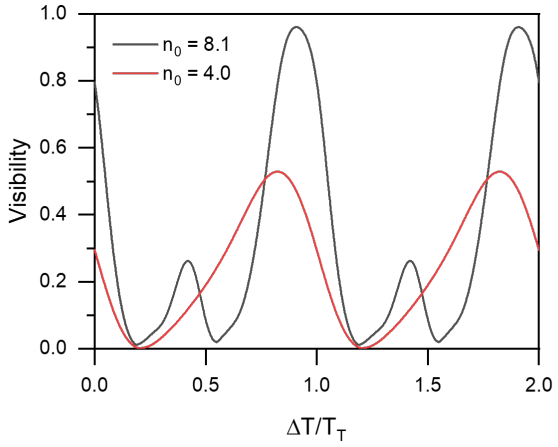

Figure 8.4: Time scan of the interference contrast for high (yellow) and low (purple) grating power of G_2, corresponding to 16% and 25% transmission, respectively. The outer gratings are set to a static 25% transmission. We see that for the optical properties of gold, we can expect the maximum contrast well before T_T. For 20% transmission, we obtain very strong contrast at $0.9T_T$, as well as a clear fractional Talbot order at $0.42T_T$. Lower grating powers give a broader resonance with maximum contrast at $0.8T_T$, remaining above 30% down to $0.6T_T$

smaller timings.
Assuming a dielectric response from the clusters [173, 159], the factor β remains takes the form

$$\beta = \frac{3Im(\varepsilon)}{|\varepsilon|^2 + Re(\varepsilon) - 2}, \tag{8.9}$$

which for gold has a value of $\beta = 0.8$ at 213 nm. Observing the resonance behavior, we see the contrast to be maximal at $T = 0.8T_T$, reducing the required interferometer length for interference. Another important factor supporting the choice of gold: it is readily available in the form of size selected nanoparticles. Commercially available gold nanoparticles span the size range of 1.8 to 1500 nm diameter, which encompasses the mass region 10^5 to 10^{10} Dalton with a size spread of below 30%. Such particles could be transferred into the gas phase using LIAD, creating a plume of particles with velocities ranging from 1 to 40 m/s [47, 123]. An alternative method comes with laser-induced transfer methods[174], where pre-etched gold targets could be illuminated to create a directed pulse of particles with size spread below 10% and forward velocities of around 20 m/s.

8.2.3 Mapping the parameter space

Knowing the target material for cluster creation is an important first step in experimental modeling, as it gives many relevant pieces of information to determine experimental bounds. For these experimental bounds, the fact that different masses lead to different beam parameters is the most important thing to keep in mind. Experimental approaches that work for one mass

range may be impossible to realize in another. To that end, it is important to map the parameter space of the optimal interference conditions to obtain a measure of which method for realizing an interferometry experiment works.
For this, we can use the relevant parameters from 7.1 to obtain an experimental framework for cluster experiments. The interferometer setup must attenuate vibrations to <5 nm amplitude to ensure the experiment does not suffer excessively from dephasing vibrations. As the mass increases, the required pressure, temperature, and interferometer height increase. The strictest limit for a tabletop experiment is gravity. Considering the Talbot time for the grating period, we expect a fall distance of around 1.6 meters for 10 MDa over a time $2T_T$. This can be reduced to around 40 cm vertical distance by compensating for gravity, which is more manageable for an experiment. Experiments with 100 MDa however, with a fall distance of 160 meters, are not feasible in a normal molecular beam experiment.
Taking 10 MDa as the limit, a background pressure of 10^{-10} mbar is necessary to prevent collision events from significantly affecting the fringe contrast. For this mass, an internal temperature of 200 K is necessary to prevent decoherence via thermal radiation. The particle size, a diameter of 10 nm at 10 MDa, does not significantly lower the grating transmission, or reduce fringe visibility due to Rayleigh scattering. Finally, with increasing mass and interrogation time, the particle must be slowed to a velocity matching the interferometer geometry. For molecules heavier than 10 MDa, we require velocities below 1 m/s. To achieve this, a way of controlling the particle velocity is needed.

Buffer gas slowing

While particle slowing with electric fields is possible, the difficulty grows with a higher mass-to-charge ratio. Likewise, the problem of cooling transverse velocities in combination with the propagation direction becomes more relevant as the particles become heavier and require better collimation. Instead of slowing with electric fields, buffer gas slowing can be a powerful tool for reducing the kinetic energy of a molecular beam [175]. By collisions with the background gas, the clusters quickly bleed off energy and are reduced to the temperature of the gas, and a corresponding velocity $v_{th} = \sqrt{2k_BT/m}$. As this method reduces the thermal velocity, we can slow both forward and transverse velocities. For an incident cluster beam traversing the buffer gas, the final velocity is determined by the number of collisions. With the initial temperature T_i and the final temperature T_f, we may use the following relation to estimate the required number of collisions

$$n_{col} = \frac{(m_b + m)^2}{2m_b m} \ln\left(\frac{T_f - T_b}{T_i - T_b}\right). \tag{8.10}$$

We see that both the relative mass of the buffer gas and its temperature are of great importance to minimize the required number of collisions. To obtain a measure of the overall slowing time required we must combine n_{col} with the collisional mean free time

$$\tau_{col} = \frac{\sqrt{m_b k_B T_b}}{4\pi p}\left(\frac{3\varrho}{4\pi m}\right)^{\frac{2}{3}}. \tag{8.11}$$

We see that for a given buffer gas and cluster, the mean free time scales linearly with pressure. To estimate the slowing rate let us assume a buffer gas of neon at 10 K, and an initial particle

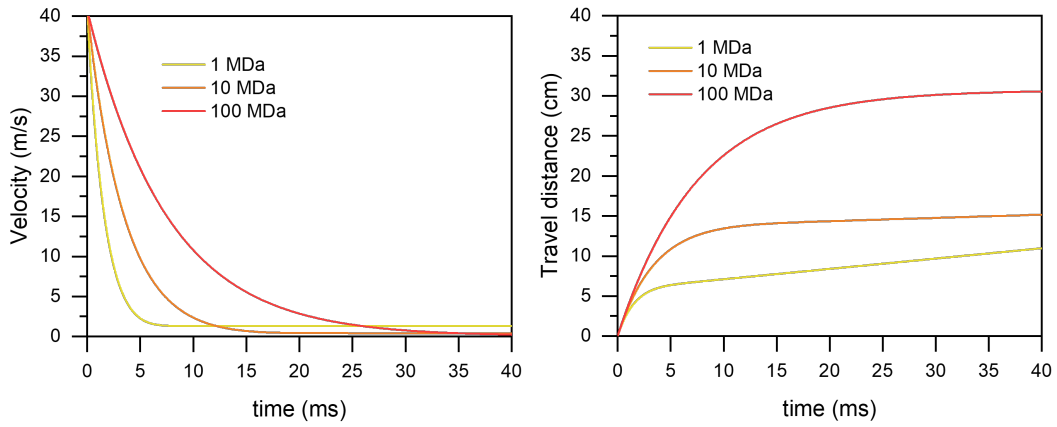

Figure 8.5: Left: Particle velocity as a function of cooling time. The collisions with the cold background gas cause the particle to lose kinetic energy until it reaches thermal equilibrium with the background gas temperature T_b. Right: Distance traveled through the buffer gas zone. The particle travels quickly initially, but the loss in velocity leads to an overall small distance traveled.

velocity of 40 m/s. With a background pressure of 10^{-3} mbar, clusters with 1 MDa can be cooled to ambient temperature in $\simeq$ 6 ms. During this process, they get slowed to $\langle v \rangle = \simeq$0.4 m/s and travel a distance of 5 cm. For higher masses, the required number of collisions increases linearly, increasing by a hundredfold for 100 MDa. However, the collision mean-free-time $decreases$ with higher mass, giving a combined mass scaling $\propto m^{1/3}$. Due to this, the distance and time necessary for cooling the particles does not scale beyond 40 ms and 30 cm. A potential candidate for the buffer gas is neon. It can be cooled down to just above 10 K and has a much more favorable mass for collision slowing than helium. With 10 K and below easily in reach using currently available cryostats, it can be used to cool at high pressures, and then be 'extracted' from the chamber with lowered temperature. The high-pressure requirement is the main drawback of the method. To quickly cool and slow the cluster beam, the buffer gas collisions must be rapid. However, to prevent collisional decoherence, the pressure during the interference measurement needs to be below 10^{-01} mbar for 10 MDa gold particles. Additionally, the buffer gas must be cooled to properly slow down the traversing clusters, requiring a cryostat and thermal insulation. The low temperatures may be exploited however to freeze out the buffer gas, letting it adsorb to the chamber walls. Staying with the example of Neon, the gas pressure drops rapidly with temperature, sinking from 2×10^{-4} mbar at 10 K to 10^{-15} mbar at 5 K. Such temperatures are viable in commercial cryostats with a cooling power of 1 W at 4 Kelvin. To ensure the particles do not leave the molecular beam during the slowing process, they can be guided through the buffer gas zone using a quadrupole ion trap[175, 176]. We can axially extract the molecules with a forward velocity of 10 times the thermal velocity to prepare a molecular beam of sufficient brightness for the experiment.

This way, the cluster beam system may be split into two parts: low vacuum ion slowing and UHV neutral interference. A possible scheme of the cooling is shown in figure 8.6.

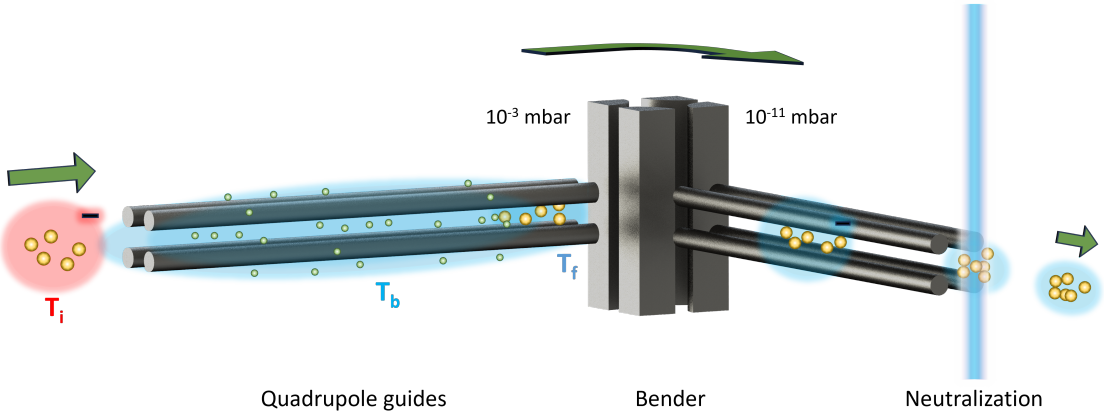

Figure 8.6: Buffer gas cooling scheme for gold clusters. The particles, with an initial temperature T_i, enter the buffer gas cloud. While collisional cooling takes place, the particles are guided using a quadrupole ion trap arrangement. From there, the ions are extracted from the high-pressure region and guided to the interferometer

Assuming a working configuration for slowing, we can guide the clusters into the interferometer itself and neutralize them for interference experiments.

8.2.4 Interferometer configurations

Once the particles are slowed to a suitable extent, they are ready for transfer into the actual experiment. Here we need to consider the interferometer configuration to best make use of the incoming particles. Having already decided on the grating laser wavelength of 213 nm, as well as the target particle, gold, we now observe the consider the mirror alignment. Will the gratings be aligned vertically along gravity or placed horizontally along the fall trajectory of the cluster beam? As the optimal configuration depends on the initial beam parameters and necessary evolution time, it is best to treat each option to highlight its advantages and disadvantages.

Vertical grating alignment, single mirror

This interferometer alignment has much in common with the previously described OTIMA setup. With a single mirror, the experiment becomes very sturdy towards vibrations, and the strict alignment criteria for individual mirrors can be removed from the considerations.
With a vertical beam alignment the particles will not fall out of the grating beams, allowing for much easier and sturdier alignment without needing to adjust the grating placement to account for gravity. However, there are limitations inherent to this configuration. With increasing particle mass, the evolution time between gratings needed to develop interference fringes scales accordingly. As the mirror needs to encompass the distance traveled during the pulse sequence its length must scale up to match. This becomes challenging for an interferometer size exceeding

20 cm but can be made possible by attaching individual mirrors to a stable support rail. This incurs additional requirements, as the mirror alignment must be accurate within 10 $\mu\mathrm{rad}$, but keeps the stability towards the vibration of a single mirror setup. Given the velocity spread of the particles, a longer interferometer sequence increases the spatial spread. This leads to a reduction in detected signal but can be compensated by illuminating a larger area with the light pulses. Increasing the size of the beam profile has disadvantages, however. The gratings become weaker as the area grows, negatively affecting the maximally reachable fringe contrast. When expanding the beams one must also consider the mirror quality, where the flatness requirement of $\lambda/10$ must hold over the entire illuminated area. Finally, a larger beam area will prevent us from using some methods for scanning the phase of G_3 due to the size constraints for some optical elements. A return to the OTIMA method of interference fringe measurement is possible but increases the necessary counts by a factor of two.
For particles beyond 1 MDa the limitations described in 7.1 become significant. The first limit to observe is once again gravity. To observe interference fringes we require good standing wave fidelity. For 213 nm light, this limits the maximal distance from the mirror surface to 5 cm, where we still expect over 70$\%$ fidelity. With a vertical grating alignment, we expect a fall distance of 1.56 cm without compensation at 1 MDa. While this is within the limit, at 10 MDa we expect a fall distance of around 40 cm even when starting with a compensating vertical velocity component gT. This puts a sharp mass limit on this interferometer configuration.

Vertical grating alignment, multiple mirrors

Three mirrors allow for flexibility in configuration that cannot be reproduced with a single mirror setup. With proper placement it is possible to tailor to different fall distances or forward velocities, allowing the interferometer to be scaled up to a much larger scale than a single mirror experiment. Additionally, the three separate mirrors allow for individual phase scanning using mechanical options like motorized stages. This method of phase scanning is already well-tested and widely applied for interference experiments. Using single mirrors, it is also much easier to obtain optics of the required surface quality if they are relatively small individually, potentially removing a major roadblock from the realization of such an experiment. However, the new limitations that come with individual mirrors are not trivial to circumvent. Proper alignment of the mirror surfaces is necessary so as not to create a mismatch in the grating period of the individual gratings. The precision required for this is very high, running on the order of 10^{-7} rad. The experimental stability towards vibrations is compromised as well when switching to individual mirrors, as there is now no common boundary to cancel individual vibration modes both transverse and torsional[42].

Vertical mirror horizontal gratings

By positioning the mirror vertically with horizontal gratings, the issue of gravity changes. Now the limitation is no longer imposed by the limited grating coherence length but by the grating alignment. This is easier to overcome by arranging the experiment beneficially[53]. A possible method here is a fountain configuration for the particle beam. Here the molecules can be guided to launch upwards at small velocities and, with vertically spaced gratings can be illuminated at

the right time for observing quantum fringes. This configuration shows the greatest advantage of a pulsed experiment, as the collimation requirement for the molecular beam is much reduced compared to a continuous experiment. Switching to a purely vertical velocity and horizontal gratings, the Coriolis effect changes slightly, but the dephasing can be prevented by aligning the gratings orthogonal to the latitudinal direction. This introduces a small mean beam shift of the molecular beam with regards to the gratings, on the order of 0.1 mm. This method shows the greatest promise for interference experiments past 1 MDa but will require more in-depth study, as it is a departure from the known methods of the Arndt group.

8.3 Concluding remarks

Interference experiments with systems of great complexity and mass are under development that can probe both fundamental physics on a previously unobtainable scale, as well as probe systems of great complexity in their fundamental, environment-free states. To reach these systems we will require the refinement of existing methods as well as the introduction of new concepts to overcome the challenges inherent to experiments with systems of great fragility, complexity, and sensitivity. In this work I have given a small sample of the path walked and yet to be walked in the direction of pulsed interferometry experiments with proteins, and possibly massive metal clusters. Future work will see a realization of some concepts described here, while others will return to the fog of unready ideas, to be picked up later and refined.

Bibliography

[1] Yaakov Y. Fein, Philipp Geyer, Patrick Zwick, Filip Kialka, Sebastian Pedalino, Marcel Mayor, Stefan Gerlich, and Markus Arndt. Quantum superposition of molecules beyond 25 kDa. *Nat. Phys.*, 15(12):1242–1245, 2019-12.

[2] A. Shayeghi, P. Rieser, G. Richter, U. Sezer, J. H. Rodewald, P. Geyer, T. J. Martinez, and M. Arndt. Matter-wave interference of a native polypeptide. *Nat Commun*, 11(1):1447, 2020-03-19.

[3] M. Planck. On an improvement of wien's equation for the spectrum. In *The Old Quantum Theory*, pages 79–81. Elsevier, 1967.

[4] A. Einstein. Über einen die erzeugung und verwandlung des lichtes betreffenden heuristischen gesichtspunkt. *Annalen der Physik*, 322(6):132–148, 1905.

[5] E. Schrödinger. Quantisierung als eigenwertproblem. *Annalen der Physik*, 384(4):361–376, 1926.

[6] Frank Wilczek. Quantum field theory. *Rev. Mod. Phys.*, 71(2):S85–S95, 1999-03-01.

[7] Jason M. Hogan, David M S Johnson, Susannah Dickerson, Tim Kovachy, Alex Sugarbaker, Sheng wey Chiow, Peter W. Graham, Mark A. Kasevich, Babak Saif, Surjeet Rajendran, Philippe Bouyer, Bernard D. Seery, Lee Feinberg, and Ritva Keski-Kuha. An atomic gravitational wave interferometric sensor in low earth orbit (AGIS-LEO). *Gen. Relativ. Gravit.*, 43(7):1953–2009, 2011.

[8] Rainer Kaltenbaek, Markus Arndt, Markus Aspelmeyer, Peter F. Barker, Angelo Bassi, James Bateman, Alessio Belenchia, Joel Bergé, Sougato Bose, Claus Braxmaier, Bruno Christophe, Garrett D. Cole, Catalina Curceanu, Animesh Datta, Maxime Debiossac, Uroš Delić, Lajos Diósi, Andrew A. Geraci, Stefan Gerlich, Christine Guerlin, Gerald Hechenblaikner, Antoine Heidmann, Sven Herrmann, Klaus Hornberger, Ulrich Johann, Nikolai Kiesel, Thomas W. LeBrun, Gerard J. Milburn, James Millen, Makan Mohageg, David C. Moore, Gavin W. Morley, Stefan Nimmrichter, Lukas Novotny, Daniel K. L. Oi, Mauro Paternostro, C. Jess Riedel, Manuel Rodrigues, Loïc Rondin, Albert Roura, Wolfgang P. Schleich, Thilo Schuldt, Benjamin A. Stickler, Hendrik Ulbricht, Christian Vogt, and Lisa Wörner. Research campaign: Macroscopic quantum resonators (MAQRO). *Quantum Sci. Technol.*, 8(1):014006, 2023-01.

[9] E. Joos and H. D. Zeh. The emergence of classical properties through interaction with the environment. *Zeitschrift für Physik B Condensed Matter*, 59(2):223–243, 1985-06. Publisher: Springer Nature.

[10] Lucia Hackermüller, Klaus Hornberger, Björn Brezger, Anton Zeilinger, and Markus Arndt. Decoherence of matter waves by thermal emission of radiation. *Nature*, 427(6976):711–4, 2004.

[11] Erich Joos. Elements of environmental decoherence. In Philippe Blanchard, Erich Joos, Domenico Giulini, Clau Kiefer, and Ion-Olimpiu Stamatescu, editors, *Decoherence: Theoretical, Experimental, and Conceptual Problems*, Lecture Notes in Physics, pages 1–17. Springer, 2000.

[12] G. C. Ghirardi, A. Rimini, and T. Weber. Unified dynamics for microscopic and macroscopic systems. *Phys. rev. D*, 34(2):470–491, 1986-07.

[13] G C Ghirardi, Philip Pearle, and Alberto Rimini. Markov processes in hilbert space and continuous spontaneous localization of systems of identical particles. *Phys. rev. A*, 42(1):78–89, 1990.

[14] Roger Penrose. On gravity's role in quantum state reduction. *Gen. Relativ. Gravit.*, 28(5):581–600, 1996.

[15] Igor Pikovski, Magdalena Zych, Fabio Costa, and Caslav Brukner. Universal decoherence due to gravitational time dilation. *Nat. Phys.*, 11(8):668–672, 2015.

[16] M. Bahrami, S. Donadi, L. Ferialdi, A. Bassi, C. Curceanu, A. Di Domenico, and B. C. Hiesmayr. Are collapse models testable with quantum oscillating systems? the case of neutrinos, kaons, chiral molecules. *Sci. Rep.*, 3:1–7, 2013.

[17] A. Vinante, M. Carlesso, A. Bassi, A. Chiasera, S. Varas, P. Falferi, B. Margesin, R. Mezzena, and H. Ulbricht. Narrowing the parameter space of collapse models with ultracold layered force sensors. *Phys. Rev. Lett.*, 125(10):100404, 2020-09-03.

[18] Louis De Broglie. *Recherches sur la théorie des quanta.* Thesis, Migration-université en cours d'affectation, 1924.

[19] G. P. Thomson and A. Reid. Diffraction of cathode rays by a thin film. *Nature*, 119(3007):890–890, 1927-06.

[20] C. Davisson and L. H. Germer. Davisson germer. *Phys. Rev.*, 30(6):705–740, 1927. ISBN: 0027-8424.

[21] I. Estermann and O. Stern. Beugung von molekularstrahlen. *Zeitschrift für Phys.*, 61(1):95–125, 1930.

[22] Dana P. Mitchell and Philip N. Powers. Bragg reflection of slow neutrons. *Phys. Rev.*, 50(5):486–487, 1936-09.

[23] A Zeilinger, C Shull, J Arthur, and M Horne. Bragg-case neutron interferometry. *Phys. rev. A*, 28(1):487–489, 1983.

[24] P E Moskowitz, P L Gould, S R Atlas, and D E Pritchard. Diffraction of an atomic beam by standing-wave radiation. *Phys. rev. Lett.*, 51(5), 1983.

[25] Pascal Szriftgiser, David Guéry-Odelin, Markus Arndt, and Jean Dalibard. Atomic wave diffraction and interference using temporal slits. *Phys. Rev. Lett.*, 77(1):4–7, 1996.

[26] J B Fixler, G T Foster, J M McGuirk, and M. A. Kasevich. Atom interferometer measurement of the newtonian constant of gravity. *Science (80-.).*, 315(5808):74–77, 2007.

[27] L Zhou, Z Y Xiong, W Yang, B Tang, W C Peng, K Hao, R B Li, M Liu, J Wang, and M S Zhan. Development of an atom gravimeter and status of the 10-meter atom interferometer for precision gravity measurement. *General Relativity and Gravitation*, 43(7):1931–1942, 2011.

[28] Hans Joachim Eichler and Jürgen Eichler. *Laser: Bauformen, Strahlführung, Anwendungen*. Springer, 2015.

[29] Mark Kasevich and Steven Chu. Atomic interferometry using stimulated raman transitions. *Phys. rev. Lett.*, 67(2):181–184, 1991.

[30] J.F. Clauser. De broglie-wave interference of small rocks and live viruses. In R. S. Cohen, M. Horne, and J. Stachel, editors, *Experimental Metaphysics*, pages 1–11. Kluwer Academic, 1997. Type: Book Section.

[31] Steven Chu. The manipulation of neutral particles. *Reviews of Modern Physics*, 70(3):685–706, 1998.

[32] B Dubetsky and P Berman. Matter-wave interference using two-level atoms and resonant optical fields. *Phys. rev. A*, 59(3):2269–2278, 1999.

[33] Ronald J. Adler, Holger Mueller, and Martin L. Perl. A terrestrial search for dark contents of the vacuum, such as dark energy, using atom interferometry. *Int. J. Mod. Phys. A*, 26(29):4959–4979, 2011-11-20.

[34] P. Hamilton, M. Jaffe, P. Haslinger, Q. Simmons, H. Müller, and J. Khoury. Atom-interferometry constraints on dark energy. *Science*, 349(6250):849–851, 2015-08-21.

[35] Stephen J Friedman, Hong Gao, and Herman Batelaan *. Resonant atomic diffraction: real versus imaginary potentials. *Journal of Modern Optics*, 52(17):2475–2500, 2005-11.

[36] Sandra Eibenberger, Stefan Gerlich, Markus Arndt, Marcel Mayor, and Jens Tüxen. Matter-wave interference of particles selected from a molecular library with masses exceeding 10,000 amu. *Physical chemistry chemical physics : PCCP*, 15(35):14696–700, 2013-09.

[37] C Riedel. Direct detection of classically undetectable dark matter through quantum decoherence. *Phys. rev. D*, 88(11):116005, 2013.

[38] John F. Clauser and Shifang Li. Talbot-vonLau atom interferometry with cold slow potassium. *Phys. Rev. A*, 49(4):R2213, 1994. ISBN: 1050-2947.

[39] William B Case, Mathias Tomandl, Sarayut Deachapunya, and Markus Arndt. Realization of optical carpets in the talbot and talbot-lau configurations. *Optics express*, 17(23):20966–20974, 2009-11.

[40] H F Talbot. LXXVI. facts relating to optical science. no. IV. *Philosophical Magazine Series 3*, 9(56):401–407, 1836.

[41] James Bateman, Stefan Nimmrichter, Klaus Hornberger, and Hendrik Ulbricht. Near-field interferometry of a free-falling nanoparticle from a point-like source. *Nat. Commun.*, 5:1–16, 2014.

[42] Yaakov Y Fein. *Long-baseline universal matter-wave interferometry*. PhD thesis, University of Vienna, 2020.

[43] Philipp Haslinger, Nadine Dörre, Philipp Geyer, Jonas Rodewald, Stefan Nimmrichter, and Markus Arndt. A universal matter-wave interferometer with optical ionization gratings in the time domain. *Nat. Phys. 9, 144 148, 2013*, 2014-02-06.

[44] E. Wigner. On the quantum correction for thermodynamic equilibrium. *Phys. rev.*, 40(5):749–759, 1932-06.

[45] Jonas Schätti, Moritz Kriegleder, Maxime Debiossac, Michael Kerschbaum, Philipp Geyer, Marcel Mayor, Markus Arndt, and Valentin Köhler. Neutralization of insulin by photocleavage under high vacuum. *Chem. Commun.*, 55(83):12507–12510, 2019.

[46] S. Anand, J. Nylk, S. L. Neale, C. Dodds, S. Grant, M. H. Ismail, J. Reboud, J. M. Cooper, and D. McGloin. Aerosol droplet optical trap loading using surface acoustic wave nebulization. *Optic Express*, 21(25):30148–30155, 2013-12-16.

[47] Uğur Sezer, Lisa Wörner, Johannes Horak, Lukas Felix, Jens Tüxen, Christoph Götz, Alipasha Vaziri, Marcel Mayor, and Markus Arndt. Laser-induced acoustic desorption of natural and functionalized biochromophores. *Anal. Chem.*, 87(11):5614–5619, 2015-06-02.

[48] Evan Weisman, Chethn Krishna Galla, Cris Montoya, Eduardo Alejandro, Jason Lim, Melanie Beck, George P. Winstone, Alexey Grinin, William Eom, and Andrew A. Geraci. An apparatus for in-vacuum loading of nanoparticles into an optical trap. *Review of Scientific Instruments*, 93(11):115115, 2022-11-29.

[49] A.I. Kuznetsov, J. Koch, and B.N. Chichkov. Laser-induced backward transfer of gold nanodroplets. *Opt. Express*, 17(21):18820, 2009-10-12.

[50] Urs Zywietz, Andrey B Evlyukhin, Carsten Reinhardt, and Boris N Chichkov. Laser printing of silicon nanoparticles with resonant optical electric and magnetic responses. *Nat. Commun.*, 5:3402, 2014.

[51] Klaus Hornberger, John Sipe, and Markus Arndt. Theory of decoherence in a matter wave talbot-lau interferometer. *Phys. rev. A*, 70(5):53608, 2004-11.

[52] Stefan Nimmrichter. *Macroscopic Matter Wave Interferometry*. Springer Theses. Springer International Publishing, 2014.

[53] Filip Kialka, Yaakov Y. Fein, Sebastian Pedalino, Stefan Gerlich, and Markus Arndt. A roadmap for universal high-mass matter-wave interferometry. *AVS Quantum Sci.*, 4(2):020502, 2022-06.

[54] Markus Arndt. De broglie's meter stick:. *Phys. Today*, 67:33–36, 2014.

[55] Sandra Eibenberger, Stefan Gerlich, Markus Arndt, Jens Tüxen, and Marcel Mayor. Electric moments in molecule interferometry. *New J Phys.*, 13(4):43033, 2011-04.

[56] Lukas Mairhofer. *Deflectometry in a Kapitza-Dirac-Talbot-Lau interferometer for matter waves*. Master thesis, University of Vienna, 2013.

[57] Yaakov Y. Fein, Armin Shayeghi, Lukas Mairhofer, Filip Kialka, Philipp Rieser, Philipp Geyer, Stefan Gerlich, and Markus Arndt. Quantum-assisted measurement of atomic diamagnetism. *Phys. Rev. X*, 10(1):011014, 2020-01-22.

[58] Sandra Eibenberger, Xiaxi Cheng, J. {\textbackslash}hspace0 167emP Cotter, and Markus Arndt. Absolute absorption cross sections from photon recoil in a matter-wave interferometer. *Phys. rev. Lett.*, 112(25), 2014-06. Publisher: American Physical Society (APS).

[59] Jonas Rodewald, Philipp Haslinger, Nadine Dörre, Benjamin A. Stickler, Armin Shayeghi, Klaus Hornberger, and Markus Arndt. New avenues for matter-wave-enhanced spectroscopy. *Applied Physics B*, 123(1), 2016-12.

[60] Christiaan Huygens. *Treatise on Light*. Macmillan And Company., Limited, 1912.

[61] Thomas Young. *A course of lectures on natural philosophy and the mechanical arts, Volume 1*. Johnson, 1807.

[62] Yoshio Torii, Yoichi Suzuki, Mikio Kozuma, Toshiaki Sugiura, Takahiro Kuga, Lu Deng, and E W Hagley. Mach-zehnder bragg interferometer for a bose-einstein condensate. *Phys. rev. A*, 61(4):41602–41604, 2000.

[63] C J Bordé, C Salomon, and S Avrillier. Optical ramsey fringes with traveling waves. *Phys. rev. A*, 30(4):1836–1848, 1984.

[64] E Lau. Beugungserscheinungen an doppelrastern. *Annalen der Physik*, 437(7):417–423, 1948.

[65] E W Hagley, L Deng, and M Kozuma. A well-collimated quasi-continuous atom laser. *Science*, 283(5408):1706–1709, 1999.

[66] Christian Knobloch, Benjamin A. Stickler, Christian Brand, Michele Sclafani, Yigal Lilach, Thomas Juffmann, Ori Cheshnovsky, Klaus Hornberger, and Markus Arndt. On the role of the electric dipole moment in the diffraction of biomolecules at nanomechanical gratings. *Fortschritte der Phys.*, pages 1–8, 2016.

[67] Ch J. Bordeé. Atomic interferometry with internal state labelling. *Phys. Lett. A*, 140(1):10–12, 1989. ISBN: 0375-9601.

[68] W A Saunders, P Fayet, and L Wöste. Photodestruction of positively and negatively charged aluminum-cluster ions. *Phys. rev. A*, 39(9):4400–4405, 1989.

[69] Stefan Nimmrichter, Philipp Haslinger, Klaus Hornberger, and Markus Arndt. Concept of an ionizing time-domain matter-wave interferometer. *New J. Phys. 13 (2011) 075002*, 2011-02-17.

[70] B. Witzel, C. J. G. J. Uiterwaal, H. Schröder, D. Charalambidis, and K.-L. Kompa. Analysis of multiphoton ionization of metal atoms in the saturation regime using subpicosecond KrF laser pulses. *Phys. Rev. A*, 58(5):3836–3848, 1998-11-01.

[71] P. Lambropoulos and X. Tang. Multiple excitation and ionization of atoms by strong lasers. *J. Opt. Soc. Am. B*, 4(5):821, 1987-05-01.

[72] David S. Zakheim and Philip M. Johnson. Rate equation modelling of molecular multiphoton ionization dynamics. *Chemical Physics*, 46(3):263–272, 1980-03-01.

[73] S. R. Coon, W. F. Calaway, M. J. Pellin, J. W. Burnett, and J. M. White. Molecular photofragmentation during non-resonant multiphoton ionization of sputtered species. *Surface and Interface Analysis*, 20(12):1007–1010, 1993.

[74] Kai Walter, Stefan Nimmrichter, and Klaus Hornberger. Multiphoton absorption in optical gratings for matter waves. *Phys. Rev. A*, 94(4):1–12, 2016.

[75] Nadine Dörre, Jonas Rodewald, Philipp Geyer, Bernd von Issendorff, Philipp Haslinger, and Markus Arndt. Photofragmentation beam splitters for matter-wave interferometry. *Phys. rev. Lett.*, 113(23):233001, 2014-12.

[76] Karl V Wood and James W.Taylor. A photoionization mass spectrometric study of autoionization in ethylene and trans-2-butene. *Int. J. Mass Spectrom. and Ion Physics*, 30(3):307–318, 1979.

[77] H. Batelaan. The kapitza-dirac effect. *Contemporary Physics*, 41(6):369–381, 2000-11.

[78] Stefan Gerlich, Lucia Hackermüller, Klaus Hornberger, Alexander Stibor, Hendrik Ulbricht, Michael Gring, Fabienne Goldfarb, Tim Savas, Marcel Müri, Marcel Mayor, and Markus Arndt. A kapitza–dirac–talbot–lau interferometer for highly polarizable molecules. *Nat. Phys.*, 3(10):711–715, 2007-08. Publisher: Springer Nature.

[79] Nadine Dörre, Philipp Haslinger, Jonas Rodewald, Philipp Geyer, and Markus Arndt. Refined model for talbot–lau matter-wave optics with pulsed photodepletion gratings. *J. Opt. Soc. Am. B*, 32(1):114, 2014. ISBN: 0740-3224 1520-8540.

[80] Klaus Hornberger, Stefan Uttenthaler, Björn Brezger, Lucia Hackermüller, Markus Arndt, and Anton Zeilinger. Collisional decoherence observed in matter wave interferometry. *Phys. Rev. Lett.*, 90(16):160401, 2003-04-22.

[81] Alexander Stibor, Klaus Hornberger, Lucia Hackermüller, Anton Zeilinger, and Markus Arndt. Talbot-lau interferometry with fullerenes: Sensitivity to inertial forces and vibrational dephasing. *Laser Phys.*, 15(1):10–17, 2005.

[82] Richard Knochenmuss. Ion formation mechanisms in UV-MALDI. *The Analyst*, 131(9):966, 2006.

[83] John J. Brady, Elizabeth J. Judge, and Robert J. Levis. Nonresonant femtosecond laser vaporization of aqueous protein preserves folded structure. *Proceedings of the National Academy of Sciences of the United States of America*, 108(30):12217–12222, 2011.

[84] Vitaliy Chagovets, Vladimir Frankevich, and Renato Zenobi. Initial velocity distribution of MALDI/LDI ions measured by internal MALDI source fourier-transform ion cyclotron resonance mass spectrometry. *J. Am. Soc. Mass Spectrom.*, 25(11):1991–1994, 2014-11-01.

[85] Marcel Niehaus and Jens Soltwisch. New insights into mechanisms of material ejection in MALDI mass spectrometry for a wide range of spot sizes. *Sci Rep*, 8(1):7755, 2018-05-17.

[86] Yong Jin Bae and Myung Soo Kim. A thermal mechanism of ion formation in MALDI. *Annual Rev. Anal. Chem.*, 8(1):41–60, 2015-07-22.

[87] K Luria, W Christen, and U Even. Generation and propagation of intense supersonic beams. *The journal of physical chemistry. A*, 115(25):7362–7367, 2011.

[88] Uzi Even. The even-lavie valve as a source for high intensity supersonic beam. *EPJ Tech. Instrum.*, 2(1):17, 2015. ISBN: 2195-7045.

[89] E. Kolodney and A. Amirav. Aerodynamical acceleration and rotational-vibrational temperatures in seeded supersonic molecular beams. *Chemical Physics*, 82(3):269–283, 1983-12-15.

[90] A. Amirav, U. Even, and J. Jortner. Cooling of large and heavy molecules in seeded supersonic beams. *Chemical Physics*, 51(1):31–42, 1980-09-15.

[91] H. Pummer, K. Hohla, M. Diegelmann, and J. P. Reilly. Discharge pumped f2 laser at 1580 Å. *Optics Communications*, 28(1):104–106, 1979-01-01.

[92] C. J. Sansonetti, J. Reader, and K. Vogler. Precision measurement of wavelengths emitted by a molecular fluorine laser at 157 nm. *Appl Opt*, 40(12):1974–1978, 2001-04-20.

[93] B. Décamps, A. Gauguet, J. Vigué, and M. Büchner. Pancharatnam phase: A tool for atom optics. *Phys. Rev. A*, 96(1):013624, 2017-07-24.

[94] K. Boller, R.-P. Haelbich, H. Hogrefe, W. Jark, and C. Kunz. Investigation of carbon contamination of mirror surfaces exposed to synchrotron radiation. *Nuclear Instruments and Methods in Physics Research*, 208(1):273–279, 1983-04.

[95] Roger W. C. Hansen, Mark Bissen, Dan Wallace, Jeff Wolske, and Tom Miller. Ultraviolet/ozone cleaning of carbon-contaminated optics. *Appl. Opt., AO*, 32(22):4114–4116, 1993-08-01.

[96] Jonas Rodewald. *Experiments with a pulsed Talbot Lau matter-wave interferometer*. phdthesis, University of Vienna, 2017.

[97] W. C. Wiley and I. H. McLaren. Time-of-flight mass spectrometer with improved resolution. *Review of Scientific Instruments*, 26(12):1150–1157, 1955-12.

[98] Philipp Geyer. *Matter-wave interferometry with complex nanoparticles*. phdthesis, University of Vienna, 2015.

[99] David M. Close. Calculated vertical ionization energies of the common alpha-amino acids in the gas phase and in solution. *J. Phys. Chem. A*, 115(13):2900–2912, 2011-04-07.

[100] J. Schätti, U. Sezer, S. Pedalino, J. P. Cotter, M. Arndt, M. Mayor, and V. Köhler. Tailoring the volatility and stability of oligopeptides. *Journal of Mass Spectrometry*, 52(8):550–556, 2017.

[101] Jonas Schätti, Philipp Rieser, Ugur Sezer, Georg Richter, Philipp Geyer, Gustavo G. Rondina, Daniel Häussinger, Marcel Mayor, Armin Shayeghi, Valentin Köhler, and Markus Arndt. Pushing the mass limit for intact launch and photoionization of large neutral biopolymers. *Commun Chem*, 1(1):93, 2018-12-10.

[102] M. Zouhair Atassi, editor. *Protein Reviews: Volume 23*, volume 1414 of *Advances in Experimental Medicine and Biology*. Springer International Publishing, 2023.

[103] Martin F. Jarrold. Peptides and proteins in the vapor phase. *Ann. Rev. Phys. Chem.*, 51(1):179–207, 2000.

[104] Rodolphe Antoine and Philippe Dugourd. Visible and ultraviolet spectroscopy of gas phase protein ions. *Phys. Chem. Chem. Phys.*, 13(37):16494–509, 2011.

[105] Judith Webster and David Oxley. Protein identification by MALDI-TOF mass spectrometry. *Methods Mol Biol*, 800:227–240, 2012.

[106] Guang S. He. Multiphoton absorption (MPA) theories. In Guang S. He, editor, *Laser Stimulated Scattering and Multiphoton Excitation*, page 0. Oxford University Press, 2022-02-25.

[107] E. W. Schlag and R. D. Levine. Ionization, charge separation, charge recombination, and electron transfer in large systems. *J. Phys. Chem.*, 96(26):10608–10616, 1992.

[108] E. W. Schlag, J. Grotemeyer, and R. D. Levine. Do large molecules ionize? *Chem. Phys. Lett.*, 190(6):521–527, 1992.

[109] C. H. Beckercor and K. J. Wufn. On the photoionization of large molecules. *J. Am. Soc. Mass Spectrom.*, 6(10):883–888, 1995-10-01.

[110] S. Sauer, H. Lehrach, and R. Reinhardt. Maldi mass spectrometry analysis of single nucleotide polymorphisms by photocleavage and charge-tagging. *Nucleic Acids Research*, 31(11):10, 2003.

[111] M. Debiossac, J. Schätti, M. Kriegleder, P. Geyer, A. Shayeghi, M. Mayor, M. Arndt, and V. Köhler. Tailored photocleavable peptides: fragmentation and neutralization pathways in high vacuum. *Phys Chem Chem Phys*, 20(16):11412–11417, 2018-04-28.

[112] Harekrushna Sahoo. Fluorescent labeling techniques in biomolecules: a flashback. *RSC Adv.*, 2(18):7017–7029, 2012-07-30.

[113] Kanjana Wiangnon and Rainer Cramer. Sample preparation: A crucial factor for the analytical performance of rationally designed MALDI matrices. *Anal. Chem.*, 87(3):1485–1488, 2015-02-03.

[114] Thorsten W. Jaskolla, Michael Karas, Udo Roth, Kerstin Steinert, Christoph Menzel, and Karsten Reihs. Comparison between vacuum sublimed matrices and conventional dried droplet preparation in MALDI-TOF mass spectrometry. *Journal of the American Society for Mass Spectrometry*, 20(6):1104–1114, 2009-06-01.

[115] M. M. El-Nahass, H. M. Zeyada, M. S. Aziz, and M. M. Makhlouf. Current transport mechanisms and photovoltaic properties of tetraphenylporphyrin/n-type silicon heterojunction solar cell. *Thin Solid Films*, 492(1):290–297, 2005-12-01.

[116] Abhik Ghosh and Torgil Vangberg. Valence ionization potentials and cation radicals of prototype porphyrins. the remarkable performance of nonlocal density functional theory. *Theor Chem Acta*, 97(1):143–149, 1997-10-01.

[117] Dennis P. Piet, David Danovich, Han Zuilhof, and Ernst J. R. Sudhölter. Ionization potentials of porphyrins and phthalocyanines. a comparative benchmark study of fast improvements of koopman's theorem. *J. Chem. Soc., Perkin Trans. 2*, 8:1653–1662, 1999.

[118] M R Andrews, C G Townsend, H J. Miesner, and W Ketterle. Observation of interference between two bose condensates. *Science*, 275(5300):637–641, 1997.

[119] I D Setija, H G C Werij, O J Luiten, M W Reynolds, T W Hijmans, and J T M Walraven. Optical cooling of atomic-hydrogen in a magnetic trap. *Phys. rev. Lett.*, 70(15):2257, 1993.

[120] A Ashkin and J M Dziedzic. Optical levitation of liquid drops by radiation pressure. *Source Sci. New Ser.*, 187(21):1073–1075, 1975.

[121] Uroš Delić, Manuel Reisenbauer, Kahan Dare, David Grass, Vladan Vuletić, Nikolai Kiesel, and Markus Aspelmeyer. Cooling of a levitated nanoparticle to the motional quantum ground state. *Science*, 367(6480):892–895, 2020-02-21.

[122] Lorenzo Magrini, Philipp Rosenzweig, Constanze Bach, Andreas Deutschmann-Olek, Sebastian G. Hofer, Sungkun Hong, Nikolai Kiesel, Andreas Kugi, and Markus Aspelmeyer. Real-time optimal quantum control of mechanical motion at room temperature. *Nature*, 595(7867):373–377, 2021-07.

[123] Maryam Nikkhou, Yanhui Hu, James A. Sabin, and James Millen. Direct and clean loading of nanoparticles into optical traps at millibar pressures. *Photonics*, 8(11):458, 2021-11.

[124] Evan Weisman, Chethn Krishna Galla, Cris Montoya, Eduardo Alejandro, Jason Lim, Melanie Beck, George P. Winstone, Alexey Grinin, William Eom, and Andrew A. Geraci. An apparatus for in-vacuum loading of nanoparticles into an optical trap. *Review of Scientific Instruments*, 93(11):115115, 2022-11-29.

[125] Ayub Khodaee, Kahan Dare, Aisling Johnson, Uroš Delić, and Markus Aspelmeyer. Dry launching of silica nanoparticles in vacuum. *AIP Advances*, 12(12):125023, 2022-12-22.

[126] Jakob Rieser, Mario A. Ciampini, Henning Rudolph, Nikolai Kiesel, Klaus Hornberger, Benjamin A. Stickler, Markus Aspelmeyer, and Uroš Delić. Tunable light-induced dipole-dipole interaction between optically levitated nanoparticles. *Science*, 377(6609):987–990, 2022-08-26.

[127] Johannes Piotrowski, Dominik Windey, Jayadev Vijayan, Carlos Gonzalez-Ballestero, Andrés de los Ríos Sommer, Nadine Meyer, Romain Quidant, Oriol Romero-Isart, René Reimann, and Lukas Novotny. Simultaneous ground-state cooling of two mechanical modes of a levitated nanoparticle. *Nat. Phys.*, 19(7):1009–1013, 2023-07.

[128] Stefan Lindner, Paul Juschitz, Jakob Rieser, Yaakov Y. Fein, Mario Ciampini, Markus Aspelmeyer, and Nikolai Kiesel. Hollow-core fiber loading of nanoparticles into ultra-high vacuum, 2023-11-23.

[129] Qingfeng Li, David Grojo, Anne-Patricia Alloncle, Boris Chichkov, and Philippe Delaporte. Digital laser micro- and nanoprinting. *Nanophotonics*, 8(1):27–44, 2019-01-01.

[130] Boris Chichkov. Laser printing: trends and perspectives. *Appl. Phys. A*, 128(11):1015, 2022-10-31.

[131] Connie Kong Wai Lee, Yexin Pan, Rongliang Yang, Minseong Kim, and Mitch Guijun Li. Laser-induced transfer of functional materials. *Top Curr Chem (Z)*, 381(4):18, 2023-05-22.

[132] Claudia Unger, Jrgen Koch, Ludger Overmeyer, and Boris N. Chichkov. Time-resolved studies of femtosecond-laser induced melt dynamics. *Opt. Express*, 20(22):24864, 2012-10-22.

[133] Urs Zywietz, Carsten Reinhardt, Andrey B. Evlyukhin, Tobias Birr, and Boris N. Chichkov. Generation and patterning of si nanoparticles by femtosecond laser pulses. *Appl. Phys. A*, 114(1):45–50, 2014-01.

[134] Denis M. Zhigunov, Andrey B. Evlyukhin, Alexander S. Shalin, Urs Zywietz, and Boris N. Chichkov. Femtosecond laser printing of single ge and SiGe nanoparticles with electric and magnetic optical resonances. *ACS Photonics*, 5(3):977–983, 2018-03-21.

[135] A. R. Moore. Electron and hole drift mobility in amorphous silicon. *Applied Physics Letters*, 31(11):762–764, 1977-12-01.

[136] Jun Ma and Sanjiv Sinha. Thermoelectric properties of highly doped n-type polysilicon inverse opals. *Journal of Applied Physics*, 112(7):073719, 2012-10-11.

[137] Seungjae Moon, Mutsuko Hatano, Minghong Lee, and Costas P. Grigoropoulos. Thermal conductivity of amorphous silicon thin films. *International Journal of Heat and Mass Transfer*, 45(12):2439–2447, 2002-06-01.

[138] Sergey Makarov, Lada Kolotova, Sergey Starikov, Urs Zywietz, and Boris Chichkov. Resonant silicon nanoparticles with controllable crystalline states and nonlinear optical responses. *Nanoscale*, 10(24):11403–11409, 2018.

[139] Alberto Piqué and Pere Serra. *Laser Printing of Functional Materials: 3D Microfabrication, Electronics and Biomedicine*. Wiley, 1 edition, 2018-02-05.

[140] Anthony Stone. *The Theory of Intermolecular Forces*, volume 2nd ed. OUP Oxford, 2013.

[141] Sergio Dominguez-Medina, Shawn Fostner, Martial Defoort, Marc Sansa, Ann-Kathrin Stark, Mohammad Abdul Halim, Emeline Vernhes, Marc Gely, Guillaume Jourdan, Thomas Alava, Pascale Boulanger, Christophe Masselon, and Sébastien Hentz. Neutral mass spectrometry of virus capsids above 100 megadaltons with nanomechanical resonators. *Science*, 362(6417):918–922, 2018-11-23.

[142] Alessio Belenchia, Giulio Gasbarri, Rainer Kaltenbaek, Hendrik Ulbricht, and Mauro Paternostro. Talbot-lau effect beyond the point-particle approximation. *Phys. Rev. A*, 100(3):033813, 2019-09-11.

[143] Steven Zimmerly, Denis Drainas, Lee A. Sylvers, and Dieter Söll. Identification of a 100-kDa protein associated with nuclear ribonuclease p activity in schizosaccharomyces pombe. *European Journal of Biochemistry*, 217(2):501–507, 1993.

[144] M. Scalf, M. S. Westphall, and L. M. Smith. Charge reduction electrospray mass spectrometry. *Anal Chem*, 72(1):52–60, 2000-01-01.

[145] Yin-Hung Lai and Yi-Sheng Wang. Matrix-assisted laser desorption/ionization mass spectrometry: Mechanistic studies and methods for improving the structural identification of carbohydrates. *Mass Spectrom (Tokyo)*, 6:S0072, 2017.

[146] K. P. Meletov. A nitrogen cryostat with adjustable temperature and cold loading of samples for the measurement of optical spectra. *Instrum Exp Tech*, 63(2):291–293, 2020-04.

[147] T. H. Chyba, R. Simon, L. J. Wang, and L. Mandel. Measurement of the pancharatnam phase for a light beam. *Opt. Lett.*, 13(7):562, 1988-07-01.

[148] S. Pancharatnam. Generalized theory of interference, and its applications. *Proc. Indian Acad. Sci.*, 44(5):247–262, 1956-11-01.

[149] G.W. Fraser. The ion detection efficiency of microchannel plates (MCPs). *Int. J. Mass Spectrom.*, 215(1):13–30, 2002-04.

[150] Ranran Liu, Qiyao Li, and Lloyd M. Smith. Detection of large ions in time-of-flight mass spectrometry: effects of ion mass and acceleration voltage on microchannel plate detector response. *J Am Soc Mass Spectrom*, 25(8):1374–1383, 2014-08.

[151] W. Ryan Parker and Jennifer S. Brodbelt. Characterization of the cysteine content in proteins utilizing cysteine selenylation with 266 nm ultraviolet photodissociation (UVPD). *J. Am. Soc. Mass Spectrom.*, 27(8):1344–1350, 2016-08-01.

[152] Andrea Vinante, Chris Timberlake, Dmitry Budker, Derek F. Jackson Kimball, Alexander O. Sushkov, and Hendrik Ulbricht. Surpassing the energy resolution limit with ferromagnetic torque sensors. *Phys. Rev. Lett.*, 127(7):070801, 2021-08-10.

[153] Jonas Rodewald, Nadine Dörre, Andrea Grimaldi, Philipp Geyer, Lukas Felix, Marcel Mayor, Armin Shayeghi, and Markus Arndt. Isotope-selective high-order interferometry with large organic molecules in free fall. *New J Phys.*, 20(3):033016, 2018. Publisher: IOP Publishing.

[154] Savas Dimopoulos, Peter W Graham, Jason M Hogan, Mark a. Kasevich, and Surjeet Rajendran. Gravitational wave detection with atom interferometry. *Physics Letters B*, 678(1):37–40, 2009.

[155] M. Abd El Rahim, R. Antoine, L. Arnaud, M. Barbaire, M. Broyer, Ch Clavier, I. Compagnon, Ph Dugourd, J. Maurelli, and D. Rayane. Position sensitive detection coupled to high-resolution time-of-flight mass spectrometry: Imaging for molecular beam deflection experiments. *Rev. Sci. Instrum.*, 75(12):5221–5227, 2004. ISBN: 00346748 (ISSN).

[156] David A. Crosby and Jens C. Zorn. Dipole polarizability of 2s13 and 2s01 metastable helium measured by the electric deflection time-of-flight method. *Phys. Rev. A*, 16(2):488–491, 1977.

[157] Ramiro Moro, Roman Rabinovitch, Chunlei Xia, and Vitaly V. Kresin. Electric dipole moments of water clusters from a beam deflection measurement. *Phys. Rev. Lett.*, 97(12), 2006.

[158] Rodolphe Antoine, Isabelle Compagnon, Driss Rayane, Michel Broyer, Philippe Dugourd, Nicolas Sommerer, Michel Rossignol, David Pippen, Frederick C. Hagemeister, and Martin F. Jarrold. Application of molecular beam deflection time-of-flight mass spectrometry to peptide analysis. *Anal. Chem.*, 75(20):5512–5516, 2003.

[159] Sven Heiles and Rolf Schäfer. *Dielectric Properties of Isolated Clusters: Beam Deflection Studies*. SpringerBriefs in Molecular Science. Springer Netherlands, 2014.

[160] Daniel J. Merthe and Vitaly V. Kresin. Electrostatic deflection of a molecular beam of massive neutral particles: Fully field-oriented polar molecules within superfluid nanodroplets. *J. Phys. Chem. Lett.*, 7(23):4879–4883, 2016.

[161] Wolfgang Demtröder. *Laser Spectroscopy 2: Experimental Techniques*. Springer Berlin Heidelberg, 2015.

[162] Aleksandr Pereverzev and Jana Roithová. Experimental techniques and terminology in gas-phase ion spectroscopy. *Journal of Mass Spectrometry*, 57(5):e4826, 2022.

[163] Hiromichi Kataura, Norikazu Irie, Nobuo Kobayashi, Yohji Achiba, Kouichi Kikuchi, Takaaki Hanyu Takaaki Hanyu, and Shigeo Yamaguchi Shigeo Yamaguchi. Optical absorption of gas phase c60 and c70. *Jpn. J. Appl. Phys.*, 32(11):L1667, 1993-11-01.

[164] Reinhard Schinke. *Photodissociation Dynamics: Spectroscopy and Fragmentation of Small Polyatomic Molecules*. Cambridge University Press, 2008.

[165] K LaiHing, P Y Cheng, and M A Duncan. Laser photoionization and spectroscopy of gas phase silver clusters. *Zeitschrift für Physik D: Atoms, Molecules and Clusters*, 13(2):161–169, 1989.

[166] Eric Rohlfing and James J Valentini. Laser-excited fluorescence spectroscopy of the jet-cooled copper trimer. *Chemical Physics Letters*, 126(2):113–118, 1986.

[167] Stefan Nimmrichter, Klaus Hornberger, Hendrik Ulbricht, and Markus Arndt. Absolute absorption spectroscopy based on molecule interferometry. *Phys. rev. A*, 78(6):63607, 2008.

[168] Lukas Neumeier, Mario A. Ciampini, Oriol Romero-Isart, Markus Aspelmeyer, and Nikolai Kiesel. Fast quantum interference of a nanoparticle via optical potential control, 2022-07-25.

[169] a Wucher and M Wahl. The formation of clusters during ion induced sputtering of metals. *Nuclear Instruments and Methods in Physics Research Section B: Beam Interactions with Materials and Atoms*, 115(1):581–589, 1996.

[170] Elisabeth Reiger, Lucia Hackermüller, Martin Berninger, and Markus Arndt. Exploration of gold nanoparticle beams for matter wave interferometry. *Opt. Commun.*, 264(2):326–332, 2006. ISBN: 0030-4018.

[171] Benedict Ofuonye, Jaseun Lee, Minjun Yan, Changwoo Sun, Jian-Min Zuo, and Ilesanmi Adesida. Electrical and microstructural properties of thermally annealed ni/au and ni/pt/au schottky contacts on AlGaN/GaN heterostructures. *Semicond. Sci. Technol.*, 29(9):095005, 2014-07.

[172] Wolfgang S. M. Werner, Kathrin Glantschnig, and Claudia Ambrosch-Draxl. Optical constants and inelastic electron-scattering data for 17 elemental metals. *J. Phys. Chem. Ref. Data*, 38(4):1013–1092, 2009-12-10.

[173] F. A. Ivanyuk. Dielectric function of metal clusters: Finite-size effects and the macroscopic limit. *Phys. Rev. B*, 77(15):155425, 2008-04-17.

[174] Filimon Zacharatos, Martin Duderstadt, Evangelos Almpanis, Lampros Patsiouras, Kestutis Kurselis, Dimitris Tsoukalas, Carsten Reinhardt, Nikolaos Papanikolaou, Boris N.

Chichkov, and Ioanna Zergioti. Laser printing of au nanoparticles with sub-micron resolution for the fabrication of monochromatic reflectors on stretchable substrates. *Optics & Laser Technology*, 135:106660, 2021-03-01.

[175] Taeman Kim. *Buffer gas cooling of ions in a radio frequency quadrupole ion guide: a study of the cooling process and cooled beam properties.* phdthesis, McGill University, 1997.

[176] Elisabeth Reiger, Lucia Hackermüller, Martin Berninger, and Markus Arndt. Exploration of gold nanoparticle beams for matter wave interferometry. *Optics Communications*, 264(2):326–332, 2006-08.

9 Acknowledgements

First, I would like to express my thanks to my supervisor, Markus Arndt. His dedication to science and to being a teacher are an inspiration, as is the boundless energy which he invests into it. With his continuous support and readiness for discussions, guidance and assistance, he was an invaluable mentor to me.

I would also like to thank Armin Shayeghi, who intensely worked with me on the OTIMA experiment, and the projects beyond, and was happy to share his ideas and insights with me. More thanks are in order to Philipp Geyer, who made sure that the experiment survived our efforts to bring the interference experiments to fruition.

I would like to thank my fellow PhD students for the stimulating discussions, work related or otherwise, that helped me stay productive and focused during my time with them. I would particularly like to thank Stefan Troyer, who was an invaluable companion in our shared project of nanoparticle meltout.

My thanks go out to our compatriots in Basel, Jonas Schätti, Hua Yong, Amal Sanal Kumar and Valentin Köhler, who performed chemical synthesis to enable the push for protein interference.

Last but not least, I would like to thank my Family. My parents, who have given me unwavering support and invaluable advice, which steered and me supported me when I needed it. My brothers, who I could share thoughts and stories with.
Thank you all sincerely.

Curriculum Vitae

Philipp Rieser

University of Vienna

philipp.rieser@univie.ac.at

Education

University of Vienna *Vienna*

PhD Phyics *04.2019 - present*

- Supervisor: Univ. Prof. Dr. Markus Arndt
- Topic: *Towards time domain interferometry with complex systems*

University of Vienna *Vienna*

MSc Phyiscs *10.2016 - 04.2019*

- Supervisor: Univ. Prof. Dr. Markus Arndt

University of Vienna *Vienna*

BSc Physics *10.2013 - 10.2016*

Publications

Published

J. Schätti, **P. Rieser**, U. Sezer, G. Richter, P. Geyer, G. G. Rondina, D. Häussinger, M. Mayor, A. Shayeghi, V. Köhler, M. Arndt, Pushing the mass limit for intact launch and photoionization of large neutral biopolymers, Communications Chemistry 1, 93 (2018)

A. Shayeghi, **P, Rieser**, G. Richter, U. Sezer, J. H. Rodewald, P. Geyer, T. J. Martinez & M. Arndt. 2017. Matter-wave interference of a native polypeptide. Nature Communications, 11, Article number: 1447 (2020)

Y.Y. Fein, A. Shayeghi, L. Mairhofer, F. Kialka, **P. Rieser**, P. Geyer, S. Gerlich, M. Arndt Quantum-Assisted Measurement of Atomic Diamagnetism, Physical Review X 10, 011014 (2020)

In Prep

A heralded source of size-controlled silicon and gold nanoparticles for optomechanics

Scholarships

2019 - present **Doctoral fellow**, Vienna center for Quantum Sciene and Technology, Austrian Science Fund (FWF)

2019 - present **Mobility fellow**, Vienna doctoral School for Physics